Title
Modeling Pacific Atoll Island Shorelines' Response to Climate Change

Author
Shope, James Brandon

Publication Date
2016

UNIVERSITTY OF CALIFORNIA
SANTA CRUZ

MODELING PACIFIC ATOLL ISLAND SHORELINES' RESPONSE TO CLIMATE CHANGE

A dissertation submitted in partial satisfaction
of the requirements for the degree of

DOCTOR OF PHILOSOPHY

in

EARTH SCIENCES

by

James B. Shope

December 2016

This dissertation of James B. Shope
is approved:

Distinguished Professor Gary Griggs, Chair

Curt Storlazzi, PhD

Associate Professor Noah Finnegan

Tyrus Miller
Vice Provost and Dean of Graduate Studies

TABLE OF CONTENTS

FIGURES AND TABLES

Chapter 1. Changes to extreme wave climates of islands within the Western Tropical Pacific throughout the 21st century under RCP 4.5 and RCP 8.5, with implications for island vulnerability and sustainability

Chapter 2. Projected atoll shoreline and run-up changes in response to sea-level rise and varying wave conditions at Wake and Midway Atolls, Northwestern Hawaiian Islands

Chapter 3. Assessing morphological controls on atoll island shoreline stability due to future sea-level rise

ABSTRACT

Modeling Pacific atoll island shorelines' response to climate change

James B. Shope

Climate change threatens established communities on low-lying Pacific atoll islands by increasing their vulnerability to wave-driven flooding and shoreline instability. Atoll islands are dynamic features whose morphology can quickly respond to changing climate, sea level, and wave conditions. Results from this thesis provide new information about how future wave climates may change near Pacific atoll islands, specific projections for flooding and erosion at two particular atolls, and insights into how atoll morphology affects shoreline susceptibility to erosion. The first study projects how wave climates may change in the western tropical Pacific by 2100 at 25 island locations under two greenhouse gas emissions scenarios. Output from four global climate models were used to run a dynamically-downscaled numerical wave model. The mean of the top 5% of future boreal winter and summer wave heights, and their associated directions and frequencies, were calculated. Large winter wave heights were projected to decrease throughout the study area, and summer large wave directions were projected to change by as much as 30°. These changes were incorporated into the second study, which modeled run-up and erosion along island shorelines at Wake and Midway Atolls under differing oceanographic forcing conditions. Sea-level rise was projected to be the dominant control on flooding and morphological change on these two atolls, indicating that atoll islands are at great risk even if future wave heights decrease. Small changes in the direction of large incident waves also had a significant impact on shoreline flooding and erosion. Better-protected shorelines (e.g., lagoon shorelines) were disproportionately affected by increasing sea level and changing wave directions. While these findings were site specific for two atypical atolls, the third study involved modeling shoreline erosional change on a schematic atoll and evaluating how initial morphology affects shoreline response. Bathymetry for a generic atoll was generated with varying morphological parameters and wave-driven erosion was calculated. The parameters that had a significant impact on shoreline erosion were: reef flat width, reef flat depth, island width, and atoll diameter. Atolls with narrower, deeper reef flats, narrower islands, and smaller diameters were most susceptible to shoreline instability with sea-level rise. Windward islands are projected to lengthen and migrate toward the lagoon, leeward islands are projected to lengthen and migrate toward the reef rim, and oblique islands are projected to migrate leeward and toward the lagoon. Findings from all three studies elucidate shoreline processes along atoll islands and provide critical information that can guide aid allocation and help communities plan for future hazards.

ACKNOWLEDGEMENTS AND DEDICATION

I would like to thank my mother, Juanita, who has always believed in me and supported my educational pursuits throughout my life. Her support has directly contributed to my desire to learn and my successes. I also want to thank my wonderful girlfriend, Sarah, who has provided constant support as I have worked through my dissertation research. As I have been finishing the last chapter of this thesis, due to an injury, Sarah has been helping by writing as I dictate. She has gone above and beyond to help me, and I owe so much of my success to her. I am therefore dedicating this thesis to my mother, Juanita Shope, and my girlfriend, Sarah Beganskas, without either of whom, I would not be who I am today. I appreciate all of their love, hard work, and dedication that has enabled me to buckle down and complete this thesis.

Thank you my advisor, Gary Griggs, who gave me the opportunity to come to California and pursue a PhD at UCSC. Gary gave me the tools and connections necessary to pursue a thesis topic with wide-reaching ramifications. I would also like to thank Curt Storlazzi (USGS). I have worked most closely with Curt during my time at UCSC. As a mentor, Curt has enabled me to tackle difficult issues and provided guidance throughout my graduate school experience. He has pushed me to work hard to produce good, relevant science and has instilled a greater work ethic in me. I am grateful to Noah Finnegan for serving on my dissertation committee and providing valuable feedback each year. Thank you to Matthew Clapham for serving on my qualifying committee. Ron Hoeke, a co-author on my second chapter, shared a lot of data with me, provided thoughtful feedback, and was always happy to help.

I would also like to thank my friends and colleagues at the U.S. Geological Survey. Li Erikson provided consistent support throughout my thesis. She was always welcoming and willing to give me a few minutes of her time to discuss details of my projects. Much of this thesis would be very different, and likely incomplete, without Li's help and input. Edwin Elias was also a great help in my second and third projects. Edwin walked me through the setup of the schematic model in my third chapter and helped me resolve a number of issues with the model output of my second chapter. This thesis is stronger thanks to his efforts. Pat Limber provided guidance on my third chapter, reviewed my second chapter and provided great suggestions, and was always a friendly face with whom I could toss around ideas. Finally, Sean Vitousek was an amazing help setting up my third chapter, was always happy to hear about my progress, and was always excited about my results.

Christie Hegermiller and Juliano Calil were great companions and peers through my time in graduate school. Whether it was discussing careers with Juliano, getting help from Christie when I was just starting to code, or just commiserating with both, I am thankful that I have been able to share part of my graduate school experience with them.

Chapter One

CHANGES TO EXTREME WAVE CLIMATES OF ISLANDS WITHIN THE WESTERN TROPICAL PACIFIC THROUGHOUT THE 21ST CENTURY UNDER RCP 4.5 AND RCP 8.5, WITH IMPLICATIONS FOR ISLAND VULNERABILITY AND SUSTAINABILITY

Published: Shope J.B., C.D. Storlazzi, L.H. Erikson, and C.A. Hegermiller (2016). Changes to extreme wave climates of islands within the Western Tropical Pacific throughout the 21st century under RCP 4.5 and RCP 8.5, with implications for island vulnerability and sustainability. *Global and Planetary Change, 141*, 25–38. doi: 10.1016/j.gloplacha.2016.03.009.

Abstract

Waves are the dominant influence on coastal morphology and ecosystem structure of tropical Pacific islands. Wave heights, periods, and directions for the 21st century were projected using near-surface wind fields from four atmosphere–ocean coupled global climate models (GCM) under representative concentration pathways (RCP) 4.5 and 8.5. GCM-derived wind fields forced the global WAVEWATCH-III wave model to generate hourly time series of bulk wave parameters around 25 islands in the mid to western tropical Pacific Ocean for historical (1976–2005), mid-century, and end-century time periods for the December–February and June–August seasons. The December–February regional wave climate is dominated by strong winds and large swell from extratropical cyclones in the north Pacific while the June–August season brings smaller waves generated by the trade winds and swell from Southern Hemisphere extratropical storms. Extreme significant wave heights decreased (~10.0%) throughout the 21st century under both climate scenarios compared to historical wave conditions and the higher radiative forcing RCP 8.5 scenario displayed a greater and more widespread decrease in extreme significant wave heights compared to the lower forcing RCP 4.5 scenario. An exception was for the end-century June–August season. Offshore of islands in the central equatorial Pacific, extreme significant wave heights displayed the largest changes from historical values. The frequency of extreme events during December–February decreased under RCP 8.5, whereas the frequency increased under RCP 4.5. Mean wave directions rotated more than 30° clockwise at several locations during June–August, which could indicate a weakening of the trade winds' influence on extreme wave directions and increasing dominance of Southern Ocean swell. The results of this study underscore that December–February large wave events will become smaller and less frequent in most regions, reducing the likelihood and magnitude of wave-driven flooding at these island locations over the 21st century. However, relatively large increases in the mean of the top 5% of significant wave heights and large changes to the mean direction of these waves in the June–August season at several islands within 150–180° E will drive greater flooding and island morphological change along previously more stable shorelines. The reported results herein project large changes to tropical Pacific island wave climates that will be necessary for assessing island vulnerability under climate change in future studies.

1.1 Introduction

Large wave events generated from tropical and extratropical cyclones pose a significant threat to low-lying Pacific island nations. Flooding from these events can damage infrastructure, salinate groundwater, and ruin crops; the waves can induce large morphological changes to island coastlines (Terry and Falkland, 2010; Aucan et al., 2012; Hoeke et al., 2013; Smithers and Hoeke, 2014). It is anticipated that sea-level rise (SLR) will increase the severity of flooding events, as more wave energy will reach the shoreline (Nicholls et al., 2007; Storlazzi et al., 2011; Seneviratne et al., 2012). However, these SLR projections do not take changing wave climates into account. Understanding how the magnitude and frequency of large wave events will change over the next century is critical to anticipate hazards to island communities and changes to island morphology.

Previous research projecting the stability and sustainability of tropical Pacific islands (Dickenson, 1999; Woodroffe, 2007; Webb and Kench, 2010) has predominantly focused on inundation from SLR. Sea level in the western tropical Pacific (WTP) rose at a rate of 4.3 mm/yr over 1993–2001, which is significantly faster than the global average of approximately 3.0 mm/yr (Church et al., 2006; 2013). Increased SLR rates in the WTP are associated with increased regional trade wind intensity (Merrifield, 2011; Merrifield and Maltrud, 2011). If SLR in the WTP continues at a fast rate, the region will likely experience more extensive inundation in the near future. However, extreme wave events coupled with SLR will threaten island communities before inundation by SLR alone, as increased sea level will contribute to extreme high water levels along coasts, allowing nearshore waves to be larger and more damaging (Seneviratne et al., 2012).

Global (Hemer et al., 2013; Mori et al., 2013) and regional (Semedo et al., 2013) projections of future WTP wave conditions show general decreases in boreal winter (December–February) and summer (June–August) significant wave heights (H_s) by the end of the 21st century. These projections, however, focus on mean wave parameters instead of extreme events. There has been limited exploration of global extreme wave conditions, but recent studies forecast decreases in Pacific extreme H_s

(Fan et al., 2013; Wang et al., 2014). Regional-scale projected extremes are still uncertain, yet Pacific island nations are increasingly threatened by SLR and depend on these projections as extreme events deliver the most devastating impacts to insular communities and island morphologies (Fletcher and Richmond, 2010; Hoeke et al., 2013).

Many extreme wave events within the WTP are dominated by swell waves generated by extratropical cyclones (Hoeke et al., 2013). In December 2008, an extreme event inundated five island nations in the tropical Pacific over a period of several days, resulting in significant damage to community infrastructure and large-scale coastal erosion (Fletcher and Richmond, 2010; Smithers and Hoeke, 2014). However, there have been few studies projecting how waves from extratropical storms within the WTP will change over the 21st century and how these changes may affect island nations in the region. Combined with King tides (maximum annual spring high tides), El Niño Southern Oscillation (ENSO)–induced seasonal sea level anomalies, and/or tropical cyclone storm surge, extratropical cyclone waves can deliver even more energy to island shorelines via reduced depth-limited breaking (Storlazzi et al., 2011; Seneviratne et al., 2012; Hoeke et al., 2013). Therefore, extratropical swell has the potential to cause significant flooding events along low-elevation Pacific island coastlines throughout the WTP.

In this paper, we present results derived from near-surface wind fields from four Coupled Model Intercomparison Project, phase 5 (CMIP5) global climate models (GCMs) used to force WAVEWATCH-III (WW3) to project wave conditions in the WTP. Projections of December–February (DJF) and June–August (JJA) parameters of the mean of the top 5% of significant wave heights were developed for historical (1976–2005), mid-century (2026–2045), and end-century (2081–2100) time periods. This study focused primarily on waves generated in extratropical regions. These extratropical-generated swell waves, although likely smaller than typhoon-generated waves, will pose a hazard to these islands throughout the 21st century as SLR enables more extensive flooding. A description of the study area's wave climatology and island vulnerability is given in section 2. Section 3 details the GCM and WW3 input parameters and analysis methods. Section 4 presents the model skill analysis, changes in wind speed conditions, and extreme wave parameters (heights, directions, and frequencies) relative to historical values. Wave parameter changes during DJF and JJA for the mid- and end-century are presented separately. A discussion of implications to island vulnerability from these changes is presented in section 5 and conclusions in section 6.

1.2 Study area

1.2.1 Wave and wind climate

This study focused on 25 island locations in the tropical Pacific west of 150° W (Figure 1-1a) that were divided into six regions based on proximity and similarity of general atmospheric patterns (Australian Bureau of Meteorology and CSIRO, 2014): Western, Marianas, Central, Northeast, Eastern Equatorial, and Southern (Figure 1-1b). WTP H_s are generally larger and more energetic during boreal winter than during other seasons (Young et al., 1999; Bromirski et al., 2013). Swell generated by northern hemisphere extratropical cyclones dominates the extreme wave climate of the WTP during boreal winters and summers. Boreal winter waves are generally the largest in the region each year, except for the Southern Hemisphere islands, where waves are largest during the boreal summer (Young, 1999). These waves can traverse more than 4000 km within the basin, delivering energy from mid-latitude cyclones to islands near the equator (Hoeke et al., 2013). During boreal summer, waves generated by easterly trade winds dominate the swell wave spectrum in the eastern half of the study area. Waves generated in the Southern Hemisphere characterize larger swell waves in the western half of the region during the boreal summer (Young, 1999; Australian Bureau of Meteorology and CSIRO, 2014).

Easterly trade winds dominate atmospheric circulation and surface winds within the region throughout most of the year (Australian Bureau of Meteorology and CSIRO, 2014). However, the strongest winds in the region are the result of tropical cyclones and other storm systems. The northeast quadrant of the study area receives strong winds and large waves from mid-latitude storms during boreal winter, despite the influence of the trade winds (Vitousek and Fletcher, 2008; Semedo et al., 2011).

Extreme winds and waves in the western half of the study area are mainly from typhoons and mid-latitude extratropical cyclones (Mori et al., 2010).

1.2.2 Island characteristics and vulnerability

Two primary island types are found within this region: volcanic “high” islands and low-altitude atoll islands. Though most high islands, such as the Mariana and Main Hawaiian Islands, have high mean elevations (10s–1000s of m), their harbors, population centers, and infrastructure are generally concentrated along the coast within a few meters of sea level. These low-elevation areas are vulnerable to large wave events (Mimura, 1999). Many high islands in the tropical Pacific have fringing reefs along their coasts that function as breakwaters for incident waves, protecting coastal areas from larger waves and reducing wave-driven flooding (Ferrario et al., 2014). Coastal groundwater on high islands can become salinated from flooding, but large abundances of fresh groundwater generally flush contaminated water out of the aquifer quickly (Rotzoll and Fletcher, 2012).

Atoll islands, such as the Marshall or Northwestern Hawaiian Islands, are low-lying carbonate islands on atoll reefs that generally have mean elevations of less than 2–3 m above sea level. They have high population densities (e.g., 8300 people/km^2 on Fongafale, Tuvalu) and represent most of the inhabited landmass in the tropical Pacific (Webb and Kench, 2010; Ford, 2012). Due to their low elevation, many atoll islands are vulnerable to inundation, saltwater intrusion, enhanced shoreline erosion, and infrastructure damage due to wave-driven flooding events that will likely be exacerbated by SLR. However, it is unlikely that WTP atoll islands will be completely inundated in the future, as they are dynamic features with shorelines that change considerably over short time periods of days to years in response to changing wave patterns (Kench and Brander, 2006; Rankey, 2011; Beetham and Kench, 2014). Even so, the mechanism by which an atoll island can vertically accrete to keep up with SLR is for wave-driven flooding events to entrain sediment from the adjacent reefs and deposit it onshore. This overwash is beneficial to island growth over geologic timescales, but such wave-induced flooding events may make these islands inhospitable for humans over shorter time scales, due to impacts to infrastructure, agriculture, and freshwater resources (Mimura, 1999; Yamano et al., 2007; Fletcher and Richmond, 2010). Once salinated due to wave-driven overwash, freshwater lenses (the main source of freshwater on atoll islands) take on the order of months to years to completely refreshen, depending on precipitation and climate (Terry and Falkland, 2010). Therefore, the frequency of these events is concerning: if large wave events become more frequent over the next century, the slow freshening process may render freshwater lenses of atoll islands permanently unpotable.

1.2.3 Implication of wave changes to island vulnerability and stability

The results of this study allow for a first-order evaluation of how changing extreme wave conditions from increased radiative forcing due to global climate change may impact processes that govern WTP island coastlines over the next century. It is therefore necessary to briefly outline how potential changes to incident waves can affect set-up, flooding, and erosional patterns along reef line shorelines. Deep-water wave heights serve as a proxy for wave energy reaching island shorelines after attenuation by coral reefs. Shoreline reefs induce depth-limited breaking of larger waves at the reef crest and flat, effectively dissipating as much as 97% of the total wave energy before it reaches shore and reducing incident wave heights up to 84% (Storlazzi et al., 2011; Ferrario et al., 2014). Although large waves may break offshore, a fraction of the energy still progresses towards shore, increasing the cross-shore radiation stress and driving set-up along the reef flat (Pequignet et al., 2011). Set-up from waves can increase local sea levels along reef-protected island coasts by as much as 32% of breaking wave heights at reef crests (Pequignet et al., 2011; Merrifield et al., 2014). Pequignet et al. (2011) and Becker et al. (2014) found that set-up along reef flats was positively correlated with reef face breaking wave heights. Increased set-up on reef flats results from larger wave heights at the reef crest, reducing wave energy dissipation at the reef crest and allows more wave energy to be delivered to the shoreline. Therefore, although much wave energy is dissipated, larger wave heights and greater resulting set-ups deliver greater energy to shore, driving flooding and potential erosion of reef-protected coastlines (Storlazzi et al., 2011; Grady et al., 2013).

1.3 Methods

1.3.1 Global climate models and analyses

Recent historical and future wave conditions were generated for the western tropical Pacific Ocean via a dynamical downscaling approach (Wang et al., 2009). Four separate atmosphere–ocean coupled global climate model (GCM) wind fields under two climate change scenarios forced the WAVEWATCH-III (WW3) numerical wave model (ver. 3.14; Tolman et al., 2002; Tolman, 2009). The selected GCMs and their resolutions are listed in Table 1-1; all GCMs follow the CMIP5 framework (World Climate Research Programme, 2013). Three time periods were simulated: historical (1976–2005), mid-century (2026–2045), and end-century (2081–2100). Two IPCC–defined climate change scenarios forced the GCM runs: representative concentration pathway (RCP) 4.5 characterizes a medium increase of radiative forcing (4.5 W/m^2 by 2100 relative to preindustrial conditions) assuming stabilization starting mid-century, and RCP 8.5 characterizes unabated radiative forcing increase to 8.5 W/m^2 by 2100 relative to preindustrial conditions (Riahi et al., 2010; Thomson et al., 2011).

GCM-derived three-hourly wind speed and direction fields forced WW3 over a near-global domain (NWW3, latitude 80° S–80° N) at a 1.00° × 1.25° spatial resolution (Table 1). Bathymetry was generated from the Naval Research Laboratory's Digital Bathymetric Data Base version 3.0 (2013) and shoreline positions were generated with the National Geophysical Data Center's Global Self-consistent Hierarchical High-resolution Geography Database version 2.2.2 (2013).Wave spectra were computed in 25 frequency bands ranging from 0.04–0.50 Hz with a directional resolution of 15°. Nonlinear quadruplet wave interactions were modeled using the Hasselmann et al. (1985) formulation, and wave growth and whitecapping were simulated via the Tolman and Chalikov (1996) source term package. Diffraction and wind interruption from the small islands within the model domain were not resolved due to the coarse spatial resolution of the WW3 domain. This limitation was accounted for within this study by focusing on trends of offshore, deep water waves that are relatively unaffected by these smaller islands. The larger Hawaiian Islands were resolved, however, and the diffraction and wind effects were accounted for within WW3. Additionally, the effects of ENSO were not considered within this study. It appears that ENSO is only somewhat realistically represented in about half of all CMIP5 GCM models (Kim and Yu, 2012). Also, Stephenson (2012) noted that ENSO variability and amplitudes within 27 CMIP5 multi-model means under climate change projections were statistically indistinguishable from values determined for the 20th century. In the few models where ENSO amplitudes do increase with climate change forcing under RCP 4.5, the changes were smaller than the standard deviation of ENSO amplitudes of all tested CMIP5 models (Kim and Yu 2012). Due to the weak to non-existent changes to ENSO intensity with climate change in these studies, it can be assumed that ENSO did not change significantly within our model runs and affect wave parameters. Hourly time series of H_s, peak wave periods (T_p), and mean wave directions (D_m) were saved at 25 locations from WW3 runs. D_m is defined as the mean direction in which H_s propagates, measured in degrees clockwise from north.

Outputs from each GCM-driven WW3 model run were concatenated into a multi-model dataset on monthly and seasonal scales. An ensemble of models better simulates observed data than any single model for dynamic GCMs and regional climate models with similar parameters (Donat et al., 2010).

Multi-model averages and standard deviations of boreal winter (DJF) and summer (JJA) extreme H_s, T_p, and D_m were calculated for historical, mid-century, and end-century periods. Extreme values are defined as the mean of the top 5% of H_s and associated T_p and D_m each season (those exceeded 36 h/month) over each time period (numbering 175,200 measurements for each future period and 262,800 measurements for the historical period). Seasonal (DJF or JJA) values were first taken from the complete model datasets; the extreme H_s and the T_p and D_m associated with those values were selected and combined into a multi-model extreme H_s value dataset from which seasonal averages were calculated. Extreme significant wave heights are denoted H_{s95}, with a standard deviation of σ_{Hs95}, and associated mean wave direction are denoted D_{m95}, with a standard deviation of σ_{Dm95}. D_{m95} was calculated by converting the wave directions of H_{s95} and H_{s95} magnitudes into rectangular (x,y) vectors and summing the resultant components. These components were then used in the formula: D_{m95} = arctangent (Σy, Σx), where D_{m95} is the mean wave direction of the top 5% of significant wave heights, y is the north–south component of the wave directions in radians and x is the east–west component of the wave directions in radians. The average direction of waves is weighted by H_{s95} and the D_{m95} equation accounts for wave directions at 0° and 360° being the same. Peak wave periods associated with H_{s95} are designated as T_{p95}. Projections of boreal spring and fall seasons are beyond the scope of this report because the selected models do not fully capture tropical cyclones, the dominant wave generation mechanism during these seasons.

For both DJF and JJA, the frequency of extreme wave events with the greatest spectral energy density each season (extrapolated to events per decade, f_{ext}) was calculated, with a standard deviation of σ_f. The power spectrum was calculated for each season on a yearly basis using a Hanning window of 30 d with 50% overlap for each season (~90 d). The power spectrum was calculated by applying an infinite impulse response discrete fast Fourier transform digital filter to the seasonal time series of H_s values of each model year by year. From the Hanning windowed power spectrum, the frequency with the greatest energy density was recorded for each model and year (e.g., 30 years of historical simulations resulted in 120 separate measurements of frequencies as there were four separate GCM-forced WW3 simulations). These frequencies were then combined into multi-model averages for each location for each time period. The selected frequencies represent the events that deliver the most energy to these islands during each season and not the exceedances of a single threshold. Rather, the frequencies recorded were the ones that have the largest potential to drive morphological change within one season. Therefore, these frequencies do not necessarily represent the frequency of H_{s95} events. The dominant frequency of future and historical periods was subsequently derived for DJF and JJA for all GCM-driven WW3 runs. Data provided herein are relegated to deep-water wave conditions in the tropical Pacific, but changes in extreme wave heights, directions, and f_{ext} were broadly extrapolated to determine effects on the coastlines of atoll and volcanic islands in the tropical Pacific. For further detail on model parameters, model output, and bulk wave parameter analysis, refer to Storlazzi et al. (2015).

1.3.2 Model skill

Multi-model historical wave conditions were compared to National Data Buoy Center (NDBC) platform measurements at the same locations in the Hawaiian Island Chain (NDBC, 2013) to evaluate the skill of the models to approximate observed extreme wave climate. The Pacific Ocean historical buoy dataset is scattered, inconsistent, and temporally short. The Hawaiian Island Chain was the only location that had observation platforms (NDBC buoys 51001, 51003, and 51004; Fig. 1b) with sufficiently long datasets (data from 1985–2005 were used in this study) to compare with WW3 historical time series. Other buoys in the Pacific generally offered only a year or less of temporal overlap with the historical simulation period. The models do not approximate the observed H_s, T_p, and f_{ext} datasets on a year-by-year basis, but rather on a multi-annual scale, and therefore an error analysis using buoys offering only limited temporal overlap was not carried out. These NDBC buoys collect hourly deep-water H_s and T_p measurements. These buoys were co-located with WW3

Hawaiian virtual buoy output locations. WW3 historical time series (1976–2005) were shortened to the same range as buoy observations (1985–2005) and the missing times of observation measurements were removed from each model time series to better match the observed historical measurements.

Model performance was assessed by calculating mean absolute error (*MAE*) between modeled and observed H_{s95}, T_{p95}, and f_{ext} during DJF and JJA. f_{ext} was calculated for each year of modeled and observed time periods and the distribution of f_{ext} values was then compared using the *MAE*, as opposed to H_{s95} and T_{p95}, for which bulk data were used. *MAE* provides a measure of model accuracy when modeled and observed values are at approximately the same scale (Hyndman et al., 2006) and is given by:

$$MAE = \frac{1}{N}\sum_{i=1}^{N}|obs_i - mod_i| \tag{1}$$

where obs_i = i^{th} observed value and mod_i = i^{th} modeled value of the empirical cumulative density functions (CDFs) for DJF and JJA H_{s95}, T_{p95}, and f_{ext}. The *MAE* is not time dependent, and the gaps in the observation data had little effect on the assessment of H_{s95} and T_{p95} model error. So long as similar proportion of occurrences for each H_{s95} and T_{p95} value were represented, the incomplete observational dataset was sufficient to determine model error. Large gaps in the time series would affect calculation of f_{ext} model error. Therefore, years without 2 months of mostly temporally continuous (no gaps larger than 24 hours) data were removed from the calculation of the *MAE* as outliers. Small gaps in the time series of a few hours were found to not significantly impact the calculation of f_{ext} and the *MAE*.

Model coherence was evaluated by calculating standard deviation of the mean (*SDOM*) of the multi-model average of H_{s95} and T_{p95} values for the historical period for DJF and JJA as:

$$SDOM = \frac{\sigma}{\sqrt{n}} \tag{2}$$

where σ = standard deviation calculated from the means of each model and n = the number of sample means (within this study n=4, the number of means for each GCM driven WW3 output).

1.4 Results

1.4.1 Model skill

Modeled H_{s95} reproduced observed H_{s95} and T_{p95} magnitudes well (Table 1-2). The H_{s95} DJF *MAE* was the smallest at buoy 51002, 0.28 m (6.1%), and the largest at buoy 51003, 0.53 m (11.5%). The 51003 *MAE* represented the largest error, but this *MAE* value was smaller than the calculated standard deviation of extreme wave heights. T_{p95} showed the opposite pattern, where buoy 51003 *MAE* was 1.30 s (9.0%). H_{s95} JJA *MAE* values were all less than or equal to 0.50 m, with buoy 51003 again being the largest at 0.50 m (18.1%). Buoy 51004 also showed a large *MAE* of 0.40 m

(12.7%). JJA *MAE* values for T_{p95} were all less than 0.50 s (3.0–5.2 %). Buoy 51003 likely had the largest H_{s95} error due to its location to the west of the Hawaiian Islands, whereby both DJF and JJA larger swell waves are refracted by the islands, leading to more variation between models and therefore error compared to historical observations. The H_{s95} and T_{p95} error statistics reported within this study are consistent with the range of similar studies that use dynamically-downscaled GCM-simulated winds to project wave climates (e.g., Hemer et al., 2013), though these statistics were for all wave parameters, not just the extremes. When calculating the *MAE*, the error values for the comparison time period (1985–2005) would be larger for H_{s95} and T_{p95} than for bulk H_s and T_p, as most non-extreme values were be similar. Therefore the error reported herein for the extremes within the range is considered acceptable and consistent with other studies, as the H_{s95} and T_{p95} error is within the range of errors reported for bulk H_s and T_p data.

The multi-model dataset did not approximate f_{ext} as well as H_{s95} and T_{p95} (Table 1-3). The largest DJF *MAE* values were 40 events/decade (24.1%) at NDBC station 51004 and 33 events/decade (18.5%). The largest JJA *MAE* was 33 events/season (25.5%) at station 51002. These larger errors indicate that the multi-model data set did not compare well to the observed datasets within these areas. Otherwise the remaining stations had smaller *MAE* (less than 15.0%). It should be noted, however, that the standard deviation of each observed location was larger than any *MAE* value. However, the model errors, being within one standard deviation of the observed mean, indicated that the even the locations with the largest errors present a possible distribution of events. Additionally, there is not a standard by which to define acceptable error for f_{ext}.

The multi-model dataset approximated DJF H_{s95} conditions well in the Hawaiian Islands, but was not as good a fit for JJA wave conditions (12.7% and 18.1% error for 51004 and 51003, respectively), with the models over-predicting wave magnitudes in both cases. Conversely, T_{p95} was approximated well in JJA compared to DJF with smaller *MAE* values during these months. f_{ext} was not approximated well compared to the *MAE* percentages of H_{s95} and T_{p95} measurements, but the error was less than one standard deviation. Overall, the multi-model dataset acceptably simulated extreme wave conditions at these buoy locations. However, it should be noted that model skill in the Hawaiian Islands is not representative for the entire study area, since the accuracy of GCM-derived results can vary from region to region. The focus of this paper is to use relative changes between modeled historical and future wave conditions to discern trends and give a first-order analysis of implications for islands within the WTP.

H_{s95} *SDOM* was largest in the Marianas Region (0.30 m) (Figure 1-1a). Additionally, extreme wave conditions were less consistent across GCM-forced model runs along the edges of the study area compared to the northern Central Region, the Eastern Equatorial Region, and the Main Hawaiian Islands. In all three regions, *SDOM* was less than 0.20 m. The western half of the study area represents the confluence of waves generated by the trade winds, Southern Hemisphere extratropical cyclones, and Northern Hemisphere extratropical cyclones. This convergence leads to large variation within each model due to the differing GCM physics and likely led to the moderate disagreement in H_{s95} between models. T_{p95} *SDOM* was often less than 1 s in magnitude and it was assumed that the T_{p95} coherence was generally good throughout the study area because of these small magnitudes (Figure 1-1b). Changes of 1–2 s can reflect sizable differences in associated wave-driven run-up values, but the differences in T_{p95} values here are not large enough to indicate that resultant run-up values are significantly affected by model scatter. Overall, model coherence was deemed acceptable throughout the region and a multi-model average mutes individual model variation to more easily discern physical changes.

1.4.2 Wind speed and direction synopsis

Projected changes to trade wind speeds, the top 5% of wind speeds, and wind directions at island locations utilized in this research are reported in-depth in Storlazzi et al. (2015), and are briefly summarized here without analysis on broader meteorological patterns. Mean mid-century wind speed near the equator in all future scenarios did not change much with increased radiative forcing. Most average wind speed changes were less than 0.25 m/s and directions remained constant, travelling west to southwest. By the end-century, DJF averages decreased by 0.25 to 0.5 m/s in most regions within the study area under both scenarios with a larger decrease under

RCP 8.5. This decrease is consistent with modeled wind speed projections documented by Dobynin et al. (2012) and Lauer et al. (2013) for annual projections. JJA saw a small increase of 0.25–0.5 m/s in the Central Region islands with a similarly small decrease in wind speed intensity under RCP 8.5 in the Northeastern region.

Patterns of the means of the top 5% of wind speeds showed much more variability. The mean of the top 5% of RCP 4.5 and RCP 8.5 DJF wind speeds decrease throughout the century, with end-century decreases being 0.25–0.50 m/s and 0.25–0.75 m/s in most regions, respectively. The top 5% of JJA wind speeds increased by 0.25–0.75 m/s in the Central Region by 2100 in both scenarios with smaller decreases of 0.25–0.50 m/s in the Marianas region in RCP 4.5 and decreases of 0.25–0.75 m/s in the Marianas and Northeast Region in RCP 8.5. The mean directions of the top 5% of DJF wind speeds did not change noticeably in each scenario. JJA top 5% wind directions within the central region rotated clockwise by 5–10° in RCP 8.5 by 2100 and 10–20° under RCP 4.5.

1.4.3 Mid-century (2026–2045)

1.4.3.1 Mid-century: RCP 4.5

Mean H_{s95} was generally projected to decrease west of 180° within the study area and in the Southern Region. Decreases of approximately 0.10–0.30 m (1.0–5.0 %) in DJF H_{s95} compared to hindcast DJF values (see Supplementary Figure S1-1a) were concentrated in the Central Region (Figure 1-2a), but the Southern Region experienced a decrease in DJF H_{s95} of 0.20–0.30 m (5.0–7.0%). The only exception to this trend was at Asuncion where DJF H_{s95} increased by 0.11 m (4.1%). σ_{Hs95} did not change significantly throughout the study area, except at American Samoa, where it increased by 0.30 m (43.0%). JJA H_{s95} decreased primarily within the Marianas Region by approximately 0.30–0.45 m (7.0–9.0%) (Figure 1-2b) compared to hindcast JJA values (see Supplementary Figure S1-1b).

D_{m95} changes primarily occurred west of 180°, with the majority in the Central Region. DJF σ_{Dm95} increased by 5–15° at Palau, Pohnpei, Kosrae, and the Big Island of Hawaii, and by 16° at Chuuk (Figure 1-3a). The largest DJF D_{m95} change (20° counterclockwise) occurred at American Samoa, accompanied by a small σ_{Dm95} decrease. JJA σ_{Dm95} decreased non-uniformly in the Central Region and at Howland by 5–10°, but showed a somewhat strong increasing trend of 5–15° in the Marianas Region and at Johnston Atoll (Figure 1-3b). The greatest JJA D_{m95} shifts were in the Western and equatorial Central Regions, where D_{m95} rotated counter clockwise by approximately 15°.

Compared to hindcast frequencies, DJF f_{ext} non-uniformly increased north of 5° N by 5–15 events/decade (2.0–12.0%), with Wake (11.0%), Molokai (7.0%), and Midway (12.0%) featuring the largest departures (Figure 1-4a). The only exception to this trend was at Kosrae, where f_{ext} decreased by 5–10 events/decade (6.5%). JJA f_{ext} showed similarly variable changes, with Howland having the largest decrease of 10–

15 events/decade (12.0%) and Guam, Kosrae, and Kwajalein decreasing by 5–10 events/decade (8.0–10.0%) (Figure 1-4b). The Big Island of Hawaii and Jarvis displayed an f_{ext} increase of 5–10 events/decade (6.0–7.0%). σ_f decreased at Kosrae, Kwajalein, Howland, and all Western Region islands.

1.4.3.2 Mid-century: RCP 8.5

Mean DJF H_{s95} was projected to generally decrease in the northern Central, western Northeast, and Western Regions by 0.10–0.30 m (2.0–6.0%) (Figure 1-2c) with the exception of the Big Island of Hawaii, which increased by 0.15 m (3.3%). DJF H_{s95} increased in the Southern Region by 0.10–0.30 m (5.0–16.0%), and σ_{Hs95} increased by 0.6 m (50.0%) at American Samoa. JJA H_{s95} values increased within the Central Region by 0.10–0.20 m (2.0–6.0%), accompanied by a small increase in σ_{Hs95} within its northern islands (Figure 1-2d). The Northeast Region exhibited scattered decreases in H_{s95} of 0.10–0.20 m (3.0–4.0%).

DJF σ_{Dm95} generally increased at Palau, the Northeast Region, and equatorial islands in the Central Region by 5–10° with the exception of the Big Island of Hawaii where σ_{Dm95} decreased by 5–10° (Figure 1-3c). This season did not exhibit many significant D_{m95} changes except at Johnston and Rose whereby values rotated approximately 15° clockwise. The majority of changes occurred during JJA. σ_{Hs95} decreased by 5–15° in Guam, the Western Region, and the equatorial Central Region islands (Figure 1-3d). σ_{Hs95} increased in the Northeastern Region and at Wake by 5–15°. The largest D_{m95}

changes during this season were at Asuncion, Kosrae, and Wake, each rotating clockwise by approximately 20°.

DJF f_{ext} decreased for the most part at every region except for Midway, Johnston, the Northwest Hawaiian Islands, and the Southern Region islands (Figure 1-4c). The largest decreases were at Kosrae and Palmyra, each decreasing by 15–20 events/decade (13.0–16.0%). Midway's f_{ext} increased by 22 events/decade (12.8%). σ_f at most islands decreased from hindcast values, with the greatest decreases (15–25 events/decade [30.0–32.0%]) at the Big Island of Hawaii, Kingman Reef, and Palmyra Atoll. JJA f_{ext} generally increased in the far eastern part of the study area, especially at Palmyra Atoll and the Big Island of Hawaii (Figure 1-4d). f_{ext} decreased in the Western Region, the northern Marianas Region, and at Wake, Enewetak, Kosrae, and Howland, with most points showing a decrease of 5–10 events/decade (7.0–13.0%) and Enewetak and Palau decreasing by 10–15 events/decade (13.7% and 13.0%, respectively). σ_f increased east of 107° E by 5–15 events/decade (2.0–30.0%), except at Wake. σ_f decreases characterized the western remainder of the study area, with the strongest decreases at Palau and Wake. These trends, however, were weak and non-uniform for each area.

1.4.4 End-century (2081–2100)

1.4.4.1 End-century: RCP 4.5

The majority of projected DJF changes in H_{s95} occurred west of 180°, with the Central and Western Regions displaying decreases of 0.10–0.30 m (3.0–7.0%) (Figure 1-2e). As opposed to mid-century values, JJA H_{s95} values increased within the Central Region; the largest increases were at Enewetak (0.32 m [10.0%]) and Bikini (0.23 m [7.5%]) (Figure 1-2f). Both islands and the majority of the Northeast islands experienced an increase in σ_{Hs95}, with the easternmost Hawaiian Islands showing the largest change.

DJF σ_{Dm95} displayed a small increase (5–15°) in the equatorial Central Region islands of Kosrae, Pohnpei, and Chuuk as well as at Howland, Palau, Midway, and the Northwest Hawaiian Islands (Figure 1-3e). In general, these changes were similar to the patterns present in both mid-century scenarios. D_{m95} did not change significantly except at Rose, where it rotated clockwise 17°. JJA σ_{Dm95} increased east of 160° E, north of 5° N, and in the northern Marianas Region (Figure 1-3f). The largest increases were at Molokai (~17°), Johnston Atoll (~17°), and Bikini (~30°). σ_{Dm95} decreased at Enewetak, Pohnpei, and Chuuk by approximately 20°. The largest D_{m95} changes occurred in the Central Region, specifically at Bikini (clockwise 33°), Enewetak (clockwise 66°), Wake (clockwise 25°), Kwajalein (clockwise 19°), and Kosrae (clockwise 21°).

Every Northeast Region island, Wake, and Kingman Reef showed an increase in DJF f_{ext}. Midway and the Northwest Hawaiian Islands exhibited the largest change of 15–20 events/decade (8.0–14.0%) and the trend became stronger progressing northeast (Figure 1-4e). σ_f increased in the Central Region and at Yap despite no significant changes in f_{ext}. JJA f_{ext} trends were inconsistent, with only the Southern Region clearly defined by a decrease in f_{ext} at both locations (Figure 1-4f). The largest increase was at the Big Island of Hawaii (20 events/decade [6.0%]), but other islands within the region had small decreases of 5–10 events decade (Kauai [6.1%] and the Northwest Hawaiian Islands [8.6%]) or showed no significant change. Similarly, σ_f changes were not consistent across the study area, with Palau, Chuuk, Wake, Majuro, and Kingman Reef decreasing while Enewetak, Kwajalein, American Samoa, and the Big Island of Hawaii increased.

1.4.4.2 End-century: RCP 8.5

Projected H_{s95} were similar to RCP 4.5 trends, but tended to be greater in magnitude and more widespread. DJF decreases affected every region except the Southern Region (Figure 1-2g). The mean H_{s95} of most points within the Northern Hemisphere decreased by more than 0.30 m, with the strongest decreases in the Central Region of approximately 0.45 m (11.0%). Decreased H_{s95} at these islands was often accompanied by a 0.15–0.30 m (30.0–40.0%) decrease in σ_{Hs95}. The H_{s95} increased by 0.46 m (13.3%) at American Samoa and by 0.13 m at Rose (3.2%), with the σ_{Hs95} of American Samoa increasing by 0.30–0.45 m. JJA patterns exhibited an increase in

Central Region H_{s95} values of 0.10 to more than 0.30 m (3.0–10.0%), and the largest increases were at Enewetak (0.32 m [9.7%]) and Bikini Atoll (0.23 m [7.6%]) (Figure 1-2h). H_{s95} decreased throughout the surrounding regions. H_{s95} decreased by 0.10–0.20 m (2.0–4.0%) in the Marianas Region, by 0.10–0.30 m (5.0–10.0%) in the western Northeast Region islands, and by 0.35 m (10.0%) at the Northwest Hawaiian Islands. Similar to RCP 4.5, σ_{Hs95} increased in the northern Central Region and the Northeast Region, with the largest increases occurring at Enewetak, Bikini, and Wake. The similarity between the two end-century scenarios was in contrast to the differences in mid-century scenarios. Boreal winter values were projected to undergo the largest changes in both scenarios.

DJF σ_{Dm95} did not change significantly except in the Northern Hawaiian Islands and at Chuuk, where values increased by 5–10° and Jarvis, where σ_{Dm95} decreased by 5–10° (Figure 1-3g). The largest changes in D_{m95} were at Asuncion (clockwise 15.0°) and American Samoa (counter-clockwise 15.0°). JJA σ_{Dm95} followed a similar increasing pattern within most Northern Hemisphere islands east of 160°, but increased by 5–10° (Figure 1-3h). σ_{Dm95} at Bikini had the largest increase (15°). JJA σ_{Dm95} decreased by 5–10° at Enewetak and Palau. The Central Region islands displayed a clockwise D_{m95} shift of about 15°. Though smaller than the RCP 4.5 scenario, shifts in D_{m95} were again largest at Enewetak (35°) and Bikini (26°).

DJF f_{ext} decreased weakly by 5–10 events/decade at many islands and strongly (15–20 events/decade [16.8%]) at Kosare. At the Big Island of Hawaii and Midway, f_{ext} increased by 5–10 events/decade (5.7% and 4.1%, respectively) (Figure 1-4g). Otherwise f_{ext} showed no significant trend. f_{ext} at Kosrae and Molokai decreased by the largest amounts: 16 (17.0%) and 14 events/decade (9.0%), respectively. σ_f similarly decreased across the study area, with stronger, more consistent decreases to the east. JJA f_{ext} decreased within the Central and Southern Regions (Figure 1-4h). Again these decreases were small, generally less than 10 events/decade (5.0–10.0%). The Northwest Hawaiian Islands and Jarvis also saw decreases of 5–10 events/decade (5.2% and 8.7% respectively) while Yap and Johnston had increases of 5–15 events/decade (7.4% and 12.2% respectively). σ_f decreased within the Central Region and at Palau. There was a small increase in σ_f (5–15 events/decade [15.0–30.0%]) in the easternmost islands, at Johnston, and in the Southern Region.

1.4.5 Statistical significance

Statistical significance of H_{s95} trends was assessed by fitting a least-squares linear regression line to yearly averages of the seasonal concatenated H_{s95} data for hindcast, mid-century, and end-century periods. The significance of the regression trend was assessed using an F-test with the null hypothesis that the regression slope is zero and an alternative hypothesis that the slope is significant at the 95% confidence level (Emery and Thomson, 2001; See Supplemental Material: Significance Tests). Effectively, if the trend is determined to be significant, then the forecast data is interpreted as significantly different (higher or lower) than the hindcast data. The significance of the H_{s95} regression model was assessed for each radiative forcing scenario and for the DJF and JJA seasons. The DJF RCP 8.5 H_{s95} trends significantly decreased at Midway, Chuuk, Asuncion, Kosrae, Palau, Pohnpei, Yap, Majuro, Enewetak, Bikini, the Northwest Hawaiian Islands, Kwajalein, Wake, Johnston, Kingman Reef, Palmyra, Howland, and Jarvis over the century. The DJF RCP 4.5 H_{s95} decreasing trend was significant at Chuuk, Kosrae, Palau, Pohnpei, Enewetak, Bikini, Kwajalein, and Wake.

JJA H_{s95} trends for both RCP 4.5 and RCP 8.5 were mostly not significant. The JJA RCP 8.5 H_{s95} trend significantly decreased at Kauai, Midway, the Northwest Hawaiian Islands, and Johnston. The JJA H_{s95} RCP 4.5 decreasing trend was statistically significant at Jarvis, though the mean values decreased by less than 0.10 m. The increase of H_{s95} during JJA at the Central region islands was not significant. As the standard deviations of H_{s95} increased by the end of the century, there was a worse fit of a least-squares trend line, effectively demonstrating no significant change.

The statistical significance of the changes in D_{m95} was assessed by comparing the directional distributions of the hindcast, mid-century, and end-century periods using a directional Kuiper test at the 95% confidence level (Stephens, 1965; Marida and Jupp, 2009; See supplemental Material: Significance Tests). The change in mid-century

RCP 4.5 DJF D_{m95} from hindcast was significant at the Big Island of Hawaii, Chuuk, Yap, Johnston, and Howland. The mid-century DJF D_{m95} change was statistically significant at Asuncion, Palau, Molokai, and Kingman Reef. Mid-century RCP 4.5 JJA D_{m95} changed significantly at the Big Island of Hawaii, Chuuk, Asuncion, Yap, Enewetak, Kingman Reef, and Rose. Mid-century RCP 4.5 JJA D_{m95} changed significantly at Chuuk, Saipan, Asuncion, Palau, Yap, the Northwest Hawaiian Islands, Wake, Rose, and Jarvis.

End-century RCP 4.5 DJF D_{m95} changed significantly at American Samoa, Saipan, Molokai, Wake, Johnston, and Rose. End-century RCP 8.5 DJF D_{m95} significantly rotated at American Samoa, Saipan, Palau, Yap, Guam, Wake, and Howland. End-century changes in RCP 4.5 JJA D_{m95} were significant at Kauai, Chuuk, Saipan, Kosrae, Palau, Pohnpei, Enewetak, Bikini, Molokai, the Northwest Hawaiian Islands, Kwajalein, Howland, and Jarvis. End-century RCP 8.5 JJA D_{m95} changed significantly at Kauai, the Big Island of Hawaii, Chuuk, Asuncion, Palau, Yap, Enewetak, Bikini, Molokai, Wake, Howland, and Jarvis.

f_{ext} changes were found, in all instances, to not be statistically significant. In general, many of the changes in f_{ext} tended to be small (generally < 16%) with only a few locations seeing a change of 25 events/decade. However, the changes observed may not necessarily be noise in the data. To adequately assess whether these changes signify an (admittedly) weak trend or noise, a larger forecast period (past 2100) will need to be simulated. These small projected changes can have larger ramifications by slightly increasing/decreasing the risk of a larger wave event coinciding with transient high sea levels.

1.5 Discussion

1.5.1 Comparison with previous studies

Most studies of mean and extreme Pacific Ocean wave climate projections in recent years have been part of larger, global-scale studies, and many only offer changes to annual means. Present model results are broadly consistent with the results from these studies under various climate change scenarios.

Hemer et al. (2013) and Semedo et al. (2013) projected that mean boreal winter H_s decreased in the western Pacific by as much as 10%, consistent with the results presented herein whereby many of the largest changes in H_{s95} at island locations decreased by 7–11% with smaller decreases throughout the entire region (Figures 1-2e, 1-2g). Similarly, Fan et al. (2014) projected a small decrease in swell and wind sea energy density west of Hawaii during the this season and Wang et al. (2014) found a decrease in maximum H_s within the region by 0.15–0.30 m under RCP 8.5 by the end of the century. The magnitudes of DJF decrease under RCP 8.5 reported in this study were as much as 0.45 m at some locations, but followed the same broad decreasing trend. Additionally, Mori et al. (2010, 2013) describe annual-scale changes to H_s averages on a global scale under climate change, projecting 0.05–0.10

m decrease in annual means. While these values are for annual means, the boreal winter is typically the most energetic season and likely dominates annual averages. Comparing these results with the end-century winter values, the decrease in wave heights west of Hawaii is still discernible, despite the different averaging scales.

JJA trends differed from Hemer et al. (2013) July–September projections within the Central Region. Their projections show a weak decreasing trend in wave heights by less than 5% whereas Figure 1-2(f, h) demonstrate an increase in H_{s95} by as much as ~10% (0.32 m) within this region, consistent with Semedo et al. (2013). Conversely, Wang et al. (2014) reported a small increase in mean and maximum July–September H_s of west of the Hawaiian Islands by as much as 0.15–0.30 m, which is within the range of reported increases within the Central Region. Similarly, they reported a decrease in mean H_s near Hawaii that is also represented in our JJA RCP 8.5 result (Figure 1-2h).

DJF directions are projected to broadly remained unchanged, often changing by less than 5° (Figure 1-3), which is supported by Hemer et al. (2013) and Fan et al (2014), where wave directions during this season did not change significantly. The greatest differences observed between studies in boreal summer wave directions were within the central region. Hemer et al. (2013) projected little change in wave directions within this region while Fan et al. (2014) demonstrated that July–September sea and swell wave directions within the region rotate clockwise in response to climate change, with the swell becoming oriented almost directly north. Figure 1-3(f, h) similarly denote a clockwise rotation in Dm_{95} for many of the islands west of 180°. The frequency of large wave events within the WTP has not been previously reported, and a discussion of potential causes of frequency changes are listed in the following section.

1.5.2 Potential cause of changes in extreme waves

Under both RCP 4.5 and 8.5 for the mid-century and end-century, DJF H_{s95} is projected to decrease throughout much of the study area, likely driven by changes to the intensity and frequency of North Pacific extatropical cyclones. It is generally agreed that there will be poleward shifts in storm tracks and resultant wave energy under warming conditions (Bengtsson et al., 2006; Ulbrich et al., 2008; Catto et al., 2011; Wu et al., 2011; Semedo et al., 2013) and that these shifts will be accompanied by decreased frequency of storm events within the extratropics (Bengtsson et al., 2006; Chang et al., 2012; Eichler et al., 2013). As the DJF wave climates of the central Pacific are greatly influenced by swell from the north Pacific storms (Alves, 2006; Semedo et al. 2011), the projected decrease in DJF H_{s95} in the Northern Hemisphere are attributed to the poleward shifts of storm tracks and reduced storm frequency. The reduction of the frequency of north Pacific storm events and the decrease of wave period and swell energy within the northwest Pacific in response to climate change (Hemer et al., 2013; Fan et al. 2014) accounts for the lower mean DJF values reported within his study. Similarly, projected increases in end-century JJA

H_{s95} likely result from increased Southern Hemisphere storm intensity, generating large swell that arrives at the Central Region islands (Bengtsson et al., 2006). A future study will need to analyze the pressure fields of the four GCM forcings used in this study to determine the magnitude of changes to storm tracks or storm frequency under the radiative forcing scenarios. However, it is beyond the scope of this study to ascertain the broader meteorological/climatological trends of storms and pressure fields through the Pacific over the 21st century. Therefore, the results are presented within the context of other studies of storm tracks, swell, and wave magnitude changes.

Changes in end-century JJA D_{m95} likely result from changes in the types of waves that dominate Central Region islands during boreal summer months. Historical mean wave directions demonstrate that Central Region islands receive most JJA wave energy from trade wind waves from the east (Figure 1-3b), with Southern Hemisphere swell becoming more dominant progressing west through the region, as can be seen by the broad clockwise rotation of D_{m95} (Figure 1-3). Southern Ocean extratropical cyclone swell waves can influence areas well into the Northern Hemisphere and dramatically affect local wave climates of the WTP (Young, 1999; Alves, 2006; Semedo et al., 2011). Clockwise shifts in wave direction at some of the Central islands suggests that, relative to trade wind seas, Southern Hemisphere swell will contribute more to extreme incident waves in the future compared to historical conditions. Fan et al. (2014) documented a strong increase in projected southern

Pacific swell energy density during the boreal summer, accompanied by a clockwise rotation of mean swell propagation direction within the central Pacific with climate change. The clockwise rotation of mean D_{m95} within the Central Region indicates a similar pattern, whereby increasing swell energy from the south will generate larger waves within the Central Region compared to today, despite projected increases to trade wind strength (and, by extension, waves) under climate changes as demonstrated by Merrifield (2011) and Merrifield and Maltrud (2011). The resultant directional shifts could dramatically alter the erosional patterns of the shorelines of both atoll and high islands. Mid-century RCP 4.5 DJF H_{s95} at the Big Island of Hawaii increased by 0.10–0.20 m compared with Midway, the Northeast Hawaiian Islands, and Kauai, where H_{s95} decreased by 0.10–0.30 m. A possible cause for this difference within the region could stem from increased energy in the generation region of larger swell that reaches the Big Island. The DJF D_{m95} for the location is broadly to the southwest, very different from the other locations, whose waves propagate towards the southeast. This increase compared to others could be due to an increase in storminess in the northeastern Pacific (Eichler et al., 2013), which would affect the Big Island of Hawaii's wave heights, but not necessarily the other Northeast Region Islands that receive the most of their DJF energy from the northwest.

f_{ext} results showed much varying trends between mid- and end-centuries for each forcing scenario. Mid-century DJF RCP 8.5 trends show the largest general decrease in f_{ext} by as much as 20 events/decade in the Northern Hemisphere, following the trend of decreasing northern hemisphere storm frequency (Bengtsson et al., 2006; Chang et al., 2012; Eichler et al., 2013). By the end-century, while there is a very weak decreasing trend, it is not as strong as during the mid-century period. The smaller magnitudes of change indicate possible changes to these storm frequencies between mid- and end-century, whereby there is a relative increase in storminess relative to the mid-century period, though this finding would be at odds with the trends of Bengtsson et al. (2006), Chang et al. (2012), and Eichler et al. (2013). The smaller magnitudes of change indicate possible changes to these storm frequencies between mid- and end-century, whereby there is a relative increase in storminess relative to the mid-century period. However, under climate change, Catto et al. (2011) noted greater storm track density in the northeastern Pacific extratropics under four times present CO_2 levels compared to a two times CO_2 levels scenario during the DJF season. This increase in frequency coupled with an eastward shift in the high storm density regions can account for the difference between frequencies. In both cases, the shifts cause a decrease in DJF large wave event frequency compared to present, but increasing storm frequency under the higher climate change scenario (reflecting greater radiative forcing during the end-century) in the northeast Pacific would likely drive smaller than mid-century changes. This change is not reflected in the H_{s95} values for the DJF season, indicating that the incident waves may be smaller as a result of this shift. The increase of 15–25 events/decade in DJF f_{ext} in the Northeast Region projected under RCP 4.5 for both mid- and end-centuries reflects increases in linear storm tack frequency trends for RCP 4.5 in the northeastern Pacific observed by Eichler et al. (2013) that were not present for RCP 8.5. The increase in storminess in the northeastern Pacific can result in an increased frequency of swell from this region reaching the islands of the Northeast Region (Alves, 2006). JJA changes were mainly attributed to changes in trade wind intensity and southern hemisphere storminess. Under most scenarios, f_{ext} decreased weakly throughout the study region, with the largest exception being the eastern islands under RCP 8.5. The general decrease here is attributed to the poleward shift of and decrease in the number of extratropical storms in the southern hemisphere, and therefore the instances of large swell that these storms generate (Bengtsson et al., 2006). These above trends are not applicable everywhere. Mid-century RCP 4.5 DJF f_{ext} for Midway increased by 25 events/decade in contrast to most other regions seeing a decrease. This difference could be due to Midway's position (being the most northern island in the study area) whereby it receives more frequent waves compared to the remainder of the study area due to storm proximity. Similarly, there is an increase in the eastern islands' f_{ext} during the JJA season during the mid-century RCP 4.5 scenario as well as the Big Island of Hawaii's f_{ext} by 2100. The rest of the Northeast region does not change dramatically, but the Big Island point's f_{ext} increases by 15–20 events/decade by 2100. It is currently unclear as to what the true drivers of the smaller scale variability could be. Therefore, further research into storm systems changes within the GCM pressure fields would need to address why these locations are singularly different during these time periods.

1.5.3 Implications for island sustainability

H_{s95} is projected to decrease throughout the mid- to western tropical Pacific during DJF throughout the 21st century under both RCP 4.5 and 8.5, with the largest decreases occurring within the Central Region by as much as 0.45 m (12.0%). Wave driven set-up along reef flats and run-up levels onshore would therefore be smaller (Becker et al., 2014, see section 2.3). Furthermore, the decrease in σ_{Hs95} under RCP 8.5 by 2100 in the Central Region indicates that H_{s95} would be consistently lower. However, with sea levels increasing by approximately 0.5–1.5 m by 2100 (Vermeer and Rhamstorf, 2009; Church et al., 2013), the effects of the projected decrease in H_{s95} will be muted and more energy will propagate to shore relative to the historical period. Increased energy at the shoreline will drive stronger reef flat currents that could result in enhanced coastal erosion (Storlazzi et al., 2011; Grady et al., 2013). Additionally, vertical reef flat accretion at atolls and fringing reefs is anticipated to be negligible due to slower growth rates compared to projected SLR rates (Buddemeier and Smith, 1988; Montaggioni, 2005), reducing the effectiveness of these reefs as a buffer for these reef-lined island shorelines into the future. More inundation and more sediment resuspension from large waves propagating onto the reef flat are certain with SLR (Storlazzi et al., 2011). The results of this study suggest that projected DJF run-up and longshore current strength along island shorelines will not be as great in magnitude throughout the Central Region, where end-century wave heights decrease by as much as 12.0% under RCP 8.5 and 7.0% under RCP 4.5 compared to using contemporary H_{s95} values to project future values under SLR (Figures 1-1e, 1-1g).

JJA run-up will increase considerably in the Central Region by the end of the century under both climate change scenarios as increased H_{s95} of as much as 10% (Figures 1-1f, 1-1h) will increase wave-driven set-up along reefs, reducing depth-limited breaking and increasing inland flooding and longshore drift magnitudes. Consequently, morphological changes of these quasi-equilibrated shorelines will be more dramatic compared to present. Increasing JJA H_{s95} at the Central Region islands coupled with SLR will drive more extensive flooding of these islands during this season.

Atoll island erosional patterns will change due to increasing wave heights and SLR, but the dominant control on island morphodynamic change is the magnitude of wave direction change. Changing wave directions in turn alters longshore current strength and possibly direction (Kench et al., 2009). The D_{m95} rotation of 15–30° in the Central Region islands (Figures 1-3f, 1-3h) could drive large shifts in coastline erosional patterns and alter longshore current intensity (Kench et al., 2009). Atoll island shorelines vary considerably over shorter time scales in response to changing wave directions and shorelines can migrate several meters over a few years under new conditions (Rankey et al., 2011). The projected clockwise rotation of JJA D_{m95} by 30–40° in the Central Region in some locations (Figure 1-3f) will cause incident waves to arrive along parts of the island coastlines that are currently not subject to larger wave events, or at least not to events of that frequency or magnitude. Historical run JJA D_{m95} within the Central Region propagated toward the west to northwest. By

2100, JJA D_{m95} under both climate scenarios is markedly different at Wake, Bikini, and Enewetak, with dominant waves travelling to the northwest to north. A D_{m95} shift of 20° could result in rapid shoreline adjustment and new erosional patterns, which would threaten island communities, especially on urbanized or human-altered islands where current extrema induce flooding and damage to infrastructure (Yamano et al., 2007; Ford, 2012). Seasonal changes in wave direction can cause significant fluctuation in atoll island shorelines; for example, Kench and Brander (2006) found that Maldivian atoll shorelines can change considerably between monsoon seasons. Therefore, the large variation in D_{m95} by 2100 between DJF and JJA at many islands, especially Enewetak and Bikini, could result in significant inter-seasonal oscillations in island shoreline areas.

f_{ext} changes can impact islands in two ways. First, a long-term increase in the frequency of large H_s events on the order of 10 events/decade, as projected for the Northeast Region under RCP 4.5 (Figure 1-4e) can alter shoreline erosion patterns by increasing episodes of strong longshore drift and the number of flooding episodes. A decrease in f_{ext} would result in the opposite pattern: fewer large erosional episodes and less frequent flooding. Second, an increase in frequency also increases the likelihood that one of these events will coincide with other contributors to anomalously high water levels (e.g., King tides or ENSO). Under RCP 4.5, DJF f_{ext} increased by 15–20 events/decade (8.0–14.0%) over the 21st century in the Northeast Region. Combined with little to no change in H_{s95} under this scenario and increasing

SLR, it is likely that the increase will drive larger and more frequent flooding along these island shorelines. An atoll island aquifer can take months to a year to freshen after a large flooding event (Terry and Falkland, 2010), and more frequent flooding from the DJF f_{ext} increase projected in the Northeast Region (Figure 1-4) may create conditions where the islands' freshwater resources are brackish for extended periods. JJA RCP 4.5 f_{ext} decreased by 5–10 events/decade (1.0–10.0%) throughout the Northern Hemisphere, but the changes were spatially scattered. Possible future damage and hazards posed to Central islands from SLR will be somewhat mitigated, as it is less likely that large waves will coincide with transient high sea levels. DJF f_{ext} under RCP 8.5 decreased largely by mid-century, by 5–20 events/decade (1.0–14.0%) throughout most regions (Figure 1-4c), and the likelihood that large wave events will occur simultaneously with temporary high sea levels will decrease. Therefore, it seems that under RCP 8.5, aside from SLR, the potential risk for large swell events to cause significant onshore damage will decrease compared to current conditions as H_{s95} will decrease by 0.20–0.40 m throughout the Northern Hemisphere regions, indicating reduced set-up and flooding potential, and the most energetic of these waves each season will become somewhat less frequent throughout the study area.

1.6. Conclusions

Coastal flooding risk will increase within the WTP due to SLR; changes in the WTP wave climate during the 21st century will modulate the magnitude and frequency of flooding. The trends observed under RCP 8.5 are an intensification of similar trends observed under RCP 4.5, except for f_{ext}. It is apparent, and expected, that a greater amount of radiative forcing (RCP 8.5) will result in the strongest changes. Under RCP 8.5, H_{s95} within the WTP during DJF will become smaller and less frequent. It is therefore possible that RCP 8.5 boreal winter waves in particular may become less hazardous as large waves will less frequently coincide with King tides or ENSO–driven water levels. Regardless, the decrease in f_{ext} will reduce any anticipated wave-driven modification of island shorelines as there will be less incident wave energy arriving at island coastlines. The biggest divergence is the increase in DJF f_{ext} in the Northeast Region under RCP 4.5, possibly leading to more flooding and more erosion of island shorelines. The large D_{m95} changes seen during JJA will also lead to dramatic shifts in island morphology and potentially damage infrastructure under both scenarios.

The projected decreases in H_{s95} during DJF, the season that typically delivers the most wave energy, throughout the study area by 2100 do not indicate that these islands will be safe from inundation. A decrease in H_{s95} results in less set-up and therefore less energy reaching island shorelines, assuming no changes to local sea level. However, even conservative estimates of SLR project a global increase of 0.50 m by 2100 (Church et al., 2013), so island shorelines will be subject to more incident wave energy regardless of changes in wave climate. Future flooding events will inevitably be larger and more frequent, affecting a larger inland area. However, the DJF H_{s95} we project indicates that flooding events and morphological changes to islands will not be as severe as if hindcast values are assumed to couple with SLR. Conversely, the large JJA D_{m95} rotations at both end-century scenarios coupled with increased sea levels and increased H_{s95} within the Central Region will drive large changes to island shorelines that will threaten infrastructure.

Future studies will need to create a more detailed picture of the changing wave climates within the WTP and the effects these changes will have on island morphologies and populations. Although the results from this study generally correlate with the changes in wave climates published by other studies (Semedo et al., 2011; Hemer et al., 2013; Fan et al., 2014), it will be important for future studies to incorporate larger multi-model ensembles of GCMs to increase result robustness. This study focused on extratropical cyclone and trade wind swell, but high water levels associated with tropical cyclones will be a necessary addition to modeling future hazards to island communities. Additionally, hazard projections will have to take into account changing f_{ext}, which has not been discussed previously. The current DJF 10-year flooding event will become more frequent due to SLR, but larger 50–100-year events that depend on the synergy of large waves and other temporarily elevated sea levels are projected to become rarer under RCP 8.5 throughout the WTP. Under RCP 4.5 this trend reverses within the Northeastern Region, where the extreme events are projected become more frequent. Otherwise, the uncertain nature of how atoll islands will respond to both rapid SLR and changing wave climates over the next century will also need to be addressed. The coral reef flats make run-up from large events by empirical relationships likely inaccurate due to wave energy reductions and changing bathymetry. Therefore it will be necessary to employ high-resolution, nearshore, hydrodynamic models to ascertain island response to the changing wave conditions presented here. Overall, the future effects of extratropical storm swell on tropical Pacific islands will be island-specific and accurate individual island response models will require detailed bathymetries and in situ ground truthing measurements.

Acknowledgments

This work was carried out under the USGS's Pacific Coral Reef Project as part of an effort in the United States and its trust territories to better understand the effect of geologic and oceanographic processes on coral reef systems and the USGS's Climate Change Impacts to the U.S. Pacific and Arctic Coasts Project to understand the impact of climate change on U.S. and U.S.-affiliated island shorelines. This project was funded by the USGS's Coastal and Marine Geology Program and the Pacific Islands Climate Change Cooperative (PICCC). P. Dalyander (USGS) contributed numerous excellent suggestions and a timely review of our work. Use of trademark names does not imply USGS endorsement of products.

References

Alves, J., 2006. Numerical modelling of ocean swell contributions to the global wind-wave climate. Ocean Modelling, 11(1–2), 98–122. Doi: doi:10.1016/j.ocemod.2004.11.007

Australian Bureau of Meteorology and CSIRO (2014). Climate Variability, Extremes and Change in the Western Tropical Pacific: New Science and Updated

Country Reports. Pacific-Australia Climate Change Science and Adaptation Planning Program Technical Report, Australian Bureau of Meteorology and Commonwealth Scientific and Industrial Research Organisation, Melbourne, Australia.

Aucan, J., Hoeke, R., Merrifield, M.A., 2012. Wave-driven sea level anomalies at the Midway tide gauge as an index of North Pacific storminess over the past 60 years: NORTH PACIFIC STORMINESS. Geophysical Research Letters 39, 1–6. doi:10.1029/2012GL052993

Becker, J.M., Merrifield, M.A., Ford, M., 2014. Water level effects on breaking wave setup for Pacific Island fringing reefs. J. Geophys. Res.-Oceans 119, 914–932. doi:10.1002/2013JC009373

Beetham, E.P., Kench, P.S., 2014. Wave energy gradients and shoreline change on Vabbinfaru platform, Maldives. Geomorphology 209, 98–110. doi:10.1016/j.geomorph.2013.11.029

Bengtsson, L., Hodges, K.I., Roeckner, E., 2006. Storm tracks and climate change. Journal of Climate 19, 3518–3543.

Bromirski, P.D., Cayan, D.R., Helly, J., Wittmann, P., 2013. Wave power variability and trends across the North Pacific. J. Geophys. Res.-Oceans 118, 6329–6348. doi:10.1002/2013JC009189

Buddemeier, R.W., Smith, S.V., 1988. Coral reef growth in an era of rapidly rising sea level: predictions and suggestions for long-term research. Coral Reefs 7, 51–56.

Catto, J.L., Shaffrey, L.C., Hodges, K.I., 2011. Northern Hemisphere Extratropical Cyclones in a Warming Climate in the HiGEM High-Resolution Climate Model. Journal of Climate 24, 5336–5352. doi:10.1175/2011JCLI4181.1

Chang, E., Guo, Y., Xia, X., 2012. CMIP5 miltimodel ensemble projection of storm track change under global warming. Journal of Geophysical Research, 117(D23), 1–19. doi: 10.1029/2012JD018578

Church, J.A., White, N.J., Hunter, J.R., 2006. Sea-level rise at tropical Pacific and Indian Ocean islands. Global and Planetary Change 53, 155–168. doi:10.1016/j.gloplacha.2006.04.001

Church, J.A., P.U. Clark, A. Cazenave, J.M. Gregory, S. Jevrejeva, A. Levermann, M.A. Merrifield, G.A. Milne, R.S. Nerem, P.D. Nunn, A.J. Payne, W.T. Pfeffer, D. Stammer and A.S. Unnikrishnan, 2013: Sea Level Change. In: Climate Change 2013: The Physical Science Basis. Contribution of Working

Group I to the Fifth Assessment Report of the Intergovernmental Panel on Climate Change [Stocker, T.F., D. Qin, G.-K. Plattner, M. Tignor, S.K. Allen, J. Boschung, A. Nauels, Y. Xia, V. Bex and P.M. Midgley (eds.)]. Cambridge University Press, Cambridge, United Kingdom and New York, NY, USA.

Dickinson, W.R., 1999. Holocene sea-level record on Funafuti and potential impact of global warming on central Pacific atolls. Quat. Res. 51, 124–132. doi:10.1006/qres.1998.2029

Dickinson, W.R., 2009. Pacific Atoll Living: How Long Already and Until When. GSA Today 19, 4. doi:10.1130/GSATG35A.1

Dobrynin, M., Murawsky., J., Yang, S., 2012. Evolution of the global wind wave climate in CMIP5 experiments. Geophysical Research Letters, 39(18), 1–6. doi: 10.1029/2012GL052843

Donat, M., Leckebusch, G., Wild, S., Ulbrich, U., 2010. Benefits and limitations of regional multi-model ensembles for storm loss estimations. Climate Research 44, 211–225. doi:10.3354/cr00891

Emery, W.J., Thomson R.E, 2001. Data Analysis Methods in Physical Oceanography. 2nd ed. Elsevier Science B.V., New York, New York, USA. pp. 638.

Eichler, T., Gaggini, N., Pan, Z., 2013. Impacts of global warming on Northern Hemisphere winter storm tracks in the CMIP5 model suite. Journal of Geophysical Research, 118(10), 3919–3932. doi: 10.1002/jgrd.50286

Fan, Y., Held, I.M., Lin, S.J., Wang, X.L., 2013. Ocean Warming Effect on Surface Gravity Wave Climate Change for the End of the Twenty-First Century. Journal of Climate 26, 6046–6066. doi:10.1175/JCLI-D-12-00410.1

Fan, Y., Lin, S.J., Griffies, S.M., Hemer, M.A., 2014. Simulated Global Swell and Wind-Sea Climate and Their Responses to Anthropogenic Climate Change at the End of the Twenty-First Century. J. Clim. 27, 3516–3536. doi:10.1175/JCLI-D-13-00198.1

Ferrario, F., Beck, M.W., Storlazzi, C.D., Micheli, F., Shepard, C.C., Airoldi, L., 2014. The effectiveness of coral reefs for coastal hazard risk reduction and adaptation. Nature Communications 5. doi:10.1038/ncomms4794

Fletcher, C.H., Richmond, B.M., 2010. Climate change in the Federated States of Micronesia: Food and water security, climate risk management, and adaptive strategies: University of Hawaii Sea Grant Report TT-10-02, 32.

Ford, M., 2012. Shoreline Changes on an Urban Atoll in the Central Pacific Ocean: Majuro Atoll, Marshall Islands. Journal of Coastal Research 279, 11–22. doi:10.2112/JCOASTRES-D-11-00008.1

Grady, A.E., Moore, L.J., Storlazzi, C.D., Elias, E., Reidenbach, M.A., 2013. The influence of sea level rise and changes in fringing reef morphology on gradients in alongshore sediment transport. Geophys. Res. Lett. 40, 3096–3101. doi:10.1002/grl.50577

Hemer, M.A., Fan, Y., Mori, N., Semedo, A., Wang, X.L., 2013. Projected changes in wave climate from a multi-model ensemble. Nature Climate Change 3, 471–476. doi:10.1038/nclimate1791

Hoeke, R.K., McInnes, K.L., Kruger, J.C., McNaught, R.J., Hunter, J.R., Smithers, S.G., 2013. Widespread inundation of Pacific islands triggered by distant-source wind-waves. Global and Planetary Change 108, 128–138. doi:10.1016/j.gloplacha.2013.06.006

Hoeke, R., Storlazzi, C., Ridd, P., 2011. Hydrodynamics of a bathymetrically complex fringing coral reef embayment: Wave climate, in situ observations, and wave prediction. J. Geophys. Res.-Oceans 116, C04018. doi:10.1029/2010JC006170

Hyndman, R.J., Koehler, A.B., 2006. Another look at measures of forecast accuracy. International Journal of Forecasting 22, 679–688. doi:10.1016/j.ijforecast.2006.03.001

Kench, P.S., Brander, R.W., 2006. Response of reef island shorelines to seasonal climate oscillations: South Maalhosmadulu atoll, Maldives. Journal of Geophysical Research 111. doi:10.1029/2005JF000323

Kench, P.S., Brander, R.W., Parnell, K.E., McLean, R.F., 2006. Wave energy gradients across a Maldivian atoll: Implications for island geomorphology. Geomorphology 81, 1–17. doi:10.1016/j.geomorph.2006.03.003

Kench, P.S., Parnell, K.E., Brander, R.W., 2009. Monsoonally influenced circulation around coral reef islands and seasonal dynamics of reef island shorelines. Marine Geology 266, 91–108. doi:10.1016/j.margeo.2009.07.013

Kim, S., Yu, J., 2012. The two types of ENSO in CMIP5 models. Geophysical Research Letters, 39(11), 1–6. doi: 10.1029/2012GL052006

Lauer, A., Zhang, C., Elison-Timm, O., 2013. Downscaling of climate change in the Hawaii region using CMIP5 results: on the choice of forcing fields. Journal of Climate, 26(24), 10006–10030. doi: 10.1175/JCLI-D-13-00126.1

Marida, K.V., Jupp, P.E., 2009. Directional Statistics. John Wiley and Sons, Ltd, New York, New York, USA. pp. 460.

Merrifield, M.A., 2011. A Shift in Western Tropical Pacific Sea Level Trends during the 1990s. Journal of Climate 24, 4126–4138. doi:10.1175/2011JCLI3932.1

Merrifield, M.A., Maltrud, M.E., 2011. Regional sea level trends due to a Pacific trade wind intensification: SEA LEVEL AND PACIFIC TRADE WINDS. Geophysical Research Letters 38, n/a–n/a. doi:10.1029/2011GL049576

Merrifield, M.A., Becker, J.M., Ford, M., Yao, Y., 2014. Observations and estimates of wave-driven water level extremes at the Marshall Islands. Geophysical Research Letters 41, 7245–7253. doi:10.1002/2014GL061005

Mimura, N., 1999. Vulnerability of island countries in the South Pacific to sea level rise and climate change. Climate research 12, 137–143.

Mori, N., Yasuda, T., Mase, H., Tom, T., Oku, Y., 2010. Projection of Extreme Wave Climate Change under Global Warming. Hydrological Research Letters 4, 15–19. doi:10.3178/hrl.4.15

Mori, N., Shimura, T., Yasuda, T., Mase, H., 2013. Multi-model climate projections of ocean surface variables under different climate scenarios—Future change of waves, sea level and wind. Ocean Engineering 71, 122–129. doi:10.1016/j.oceaneng.2013.02.016

National Data Buoy Center (NDBC), 2013. National Oceanic and Atmospheric Administration online data [URL: http://www.ndbc.noaa.gov/].

National Geophysical Data Center (NGDC), 2013. Global Self-consistent Hierarchial High-resolution Geography Database version 2.2.2 online data [URL: http://www.ngdc.noaa.gov/mgg/shorelines/gshhs.html].

Naval Research Laboratory (NRL), 2013. Digital Bathymetric Database version 3.0 online data [URL: http://www7320.nrlssc.navy.mil/DBDB2_WWW/v3.0/NRLCOM_dbdb2.html].

Nicholls, R.J., P.P. Wong, V.R. Burkett, J.O. Codignotto, J.E. Hay, R.F. McLean, S. Ragoonaden and C.D. Woodroffe, 2007: Coastal systems and low-lying areas. Climate Change 2007: Impacts, Adaptation and Vulnerability. Contribution of Working Group II to the Fourth Assessment Report of the Intergovernmental Panel on Climate Change, M.L. Parry, O.F. Canziani, J.P. Palutikof, P.J. van der Linden and C.E. Hanson, Eds., Cambridge University Press, Cambridge, UK, 315–356.

Pequignet, A.C., Becker, J.M., Merrifield, M.A., Boc, S.J., 2011. The dissipation of wind wave energy across a fringing reef at Ipan, Guam. Coral Reefs, 36(3), 71–82.

Rankey, E.C., 2011. Nature and stability of atoll island shorelines: Gilbert Island chain, Kiribati, equatorial Pacific: Atoll shoreline change, equatorial Pacific. Sedimentology 58, 1831–1859. doi:10.1111/j.1365-3091.2011.01241.x

Riahi, K., Krey, V., Rao, S., Chirkov, V., Fischer, G., Kolp, P., Kindermann, G., Nakicenovic, N., and Rafai, P., 2010. RCP-8.5: Exploring the consequence of high emission trajectories. Climatic Change, 109(1–2), 33–57.

Rotzoll, K., Fletcher, C.H., 2012. Assessment of groundwater inundation as a consequence of sea-level rise. Nature Climate Change 3, 477–481. doi:10.1038/nclimate1725

Semedo, A., Sušelj, K., Rutgersson, A., Sterl, A., 2011. A Global View on the Wind Sea and Swell Climate and Variability from ERA-40. Journal of Climate 24, 1461–1479. doi:10.1175/2010JCLI3718.1

Semedo, A., Weisse, R., Behrens, A., Sterl, A., Bengtsson, L., Günther, H., 2013. Projection of Global Wave Climate Change toward the End of the Twenty-First Century. Journal of Climate, 26(21), 8269–8288. doi: 10.1175/JCLI-D-12-00658.1

Seneviratne, S.I., N. Nicholls, D. Easterling, C.M. Goodess, S. Kanae, J. Kossin, Y. Luo, J. Marengo, K. McInnes, M. Rahimi, M. Reichstein, A. Sorteberg, C. Vera, and X. Zhang, 2012: Changes in climate extremes and their impacts on the natural physical environment. In: Managing the Risks of Extreme Events and Disasters to Advance Climate Change Adaptation [Field, C.B., V. Barros, T.F. Stocker, D. Qin, D.J. Dokken, K.L. Ebi, M.D. Mastrandrea, K.J. Mach, G.-K. Plattner, S.K. Allen, M. Tignor, and P.M. Midgley (eds.)]. A Special Report of Working Groups I and II of the Intergovernmental Panel on Climate Change (IPCC). Cambridge University Press, Cambridge, UK, and New York, NY, USA, pp. 109–230.

Smithers, S.G., Hoeke, R.K., 2014. Geomorphological impacts of high-latitude storm waves on low-latitude reef islands — Observations of the December 2008 event on Nukutoa, Takuu, Papua New Guinea. Geomorphology 222, 106–121. doi:10.1016/j.geomorph.2014.03.042

Stephens, M.A., 1965. The goodness-of-fit statistic VN: distribution and significance points. Biometrics 52(3–4), 309–321.

Stevenson, S., 2012. Significant changes to ENSO strength and impacts in the twenty-first century: Results from CMIP5. Geophysical Research Letters, 39(17), 1–5. doi: 10.1029/2012GL052759

Storlazzi, C.D., Elias, E., Field, M.E., Presto, M.K., 2011. Numerical modeling of the impact of sea-level rise on fringing coral reef hydrodynamics and sediment transport. Coral Reefs 30, 83–96. doi:10.1007/s00338-011-0723-9

Storlazzi, C.D., Shope, J.B., Erikson, L.H., Hegermiller, C.A., and Barnard, P.L., 2015, Future wave and wind projections for United States and United States-affiliated Pacific Islands: U.S. Geological Survey Open-File Report 2015–1001, 426. [URL: http://dx.doi.org/10.3133/ofr20151001].

Terry, J.P., Falkland, A.C., 2010. Responses of atoll freshwater lenses to storm-surge overwash in the Northern Cook Islands. Hydrogeology Journal 18, 749–759. doi:10.1007/s10040-009-0544-x

Thomson, A.M., Calvin, K.V., Smith, S.J., Kyle, G.P., Volke, A., Patel, P., Delgado-Arias, S., Bond-Lamberty, B., Wise, M.A., Clarke, L.E., Edmonds, J.A., 2011. RCP4.5: a pathway for stabilization of radiative forcing by 2100. Climatic Change 109, 77–94. doi:10.1007/s10584-011-0151-4

Tolman, H.L., 2009. User manual and system documentation of WAVEWATCH III version 3.14: NOAA/NWS/NCEP/MMAB Technical Note 276, 19.

Ulbrich, U., Pinto, J.G., Kupfer, H., Leckebusch, G.C., Spangehl, T., Reyers, M., 2008. Changing Northern Hemisphere Storm Tracks in an Ensemble of IPCC Climate Change Simulations. Journal of Climate 21, 1669–1679. doi:10.1175/2007JCLI1992.1

Vermeer, M., Rahmstorf, S., 2009. Global sea level linked to global temperature. Proceedings of the National Academy of Sciences 106, 21527–21532.

Vitousek, S., Fletcher, C.H., 2008. Maximum Annually Recurring Wave Heights in Hawai'i 1. Pacific Science 62, 541–553.

Wang, X.L., Swail, V.R., Zwiers, F.W., 2006. Climatology and changes of extratropical cyclone activity: Comparison of ERA-40 with NCEP-NCAR reanalysis for 1958-2001. Journal of Climate 19, 3145–3166.

Wang, X., Swail, V., Cox, A., 2009. Dynamical versus statistical downscaling methods for ocean wave heights. International journal of climatology, 30(3), 317–332. doi: 10.1002/joc.1899

Wang, X.L., Feng, Y., Swail, V. R., 2014. Changes in global ocean wave heights as projected using multimodel CMIP5 simulations. Geophysical Research Letters 41(3), 1026–1034. doi: 10.1002/2013GL058650.

Webb, A.P., Kench, P.S., 2010. The dynamic response of reef islands to sea-level rise: Evidence from multi-decadal analysis of island change in the Central Pacific. Global and Planetary Change 72, 234–246. doi:10.1016/j.gloplacha.2010.05.003

Woodroffe, C.D., 2008. Reef-island topography and the vulnerability of atolls to sea-level rise. Glob. Planet. Change 62, 77–96. doi:10.1016/j.gloplacha.2007.11.001

World Climate Research Programme, 2013. CMIP5 - Coupled Model Intercomparison Project Phase 5 overview. [URL: http://cmip-pcmdi.llnl.gov/cmip5/].

Wu, Y., Ting, M., Seager., R., Huang, H., Cane, M.A., 2011. Changes in storm tracks and energy transports in a warmer climate simulated by the GFDL CM2.1 model. Climate Dynamics 3(1–2), 53–72. doi: 10.1007/s00382-010-0776-4

Yamano, H., Kayanne, H., Yamaguchi, T., Kuwahara, Y., Yokoki, H., Shimazaki, H., Chikamori, M., 2007. Atoll island vulnerability to flooding and inundation revealed by historical reconstruction: Fongafale Islet, Funafuti Atoll, Tuvalu. Global and Planetary Change 57, 407–416. doi:10.1016/j.gloplacha.2007.02.007

Young, I.R., 1999. Seasonal variability of the global ocean wind and wave climate. International Journal of Climatology 19, 931–950.

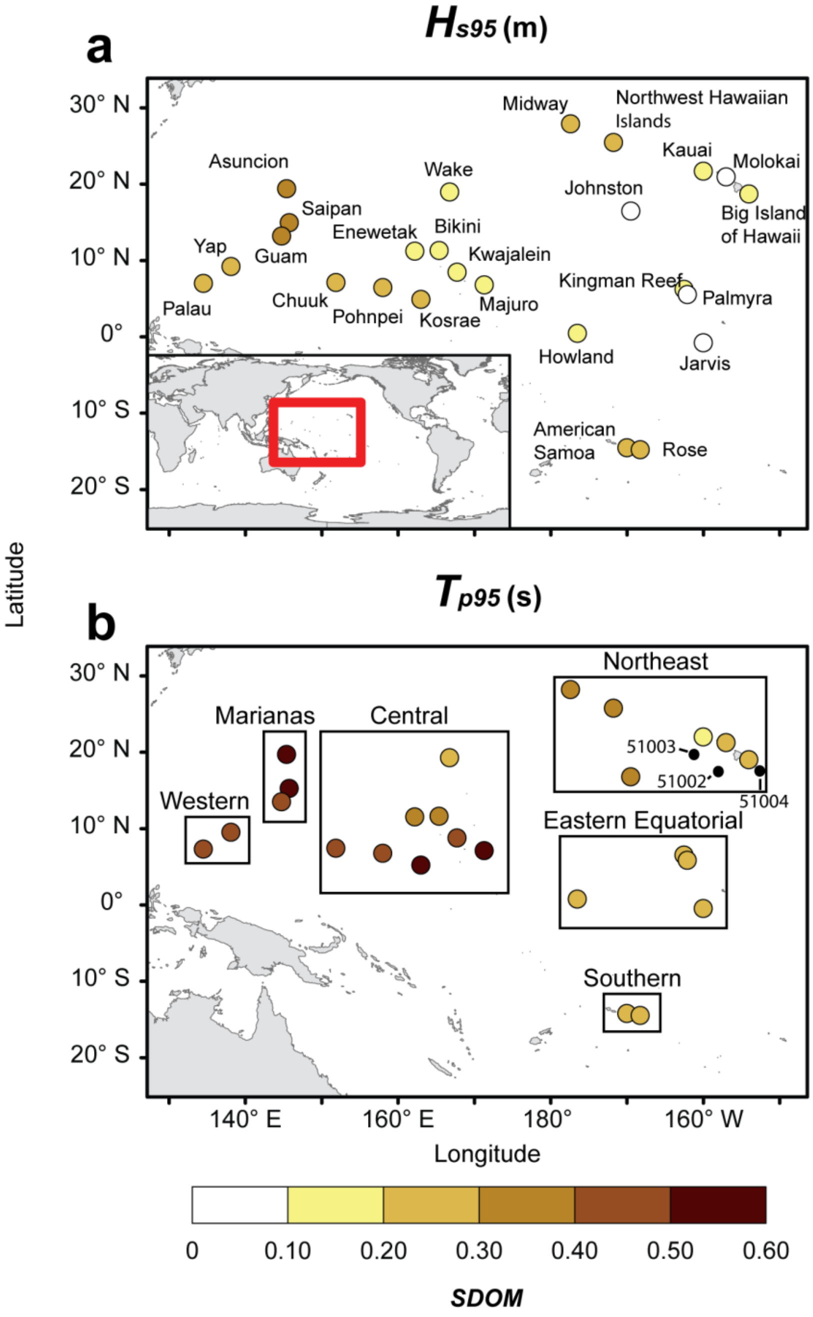

Figure 1-1. Extent map of the study area displaying model coherence over the hindcasted period (1976-2005). (**a**) H_{s95} and (**b**) T_{p95}. The colors represent the magnitude of the standard deviation of the mean (SDOM) for (**a.**) H_{s95} and (**b.**) T_p of H_{s95} values. The red box in (**a**) indicates the study area within the global map. Black boxes in (**b**) represent regional groupings of output points based on proximity and similar variation. Black points in (**b**) represent National Data Buoy Center station names and locations near the Hawaiian Islands.

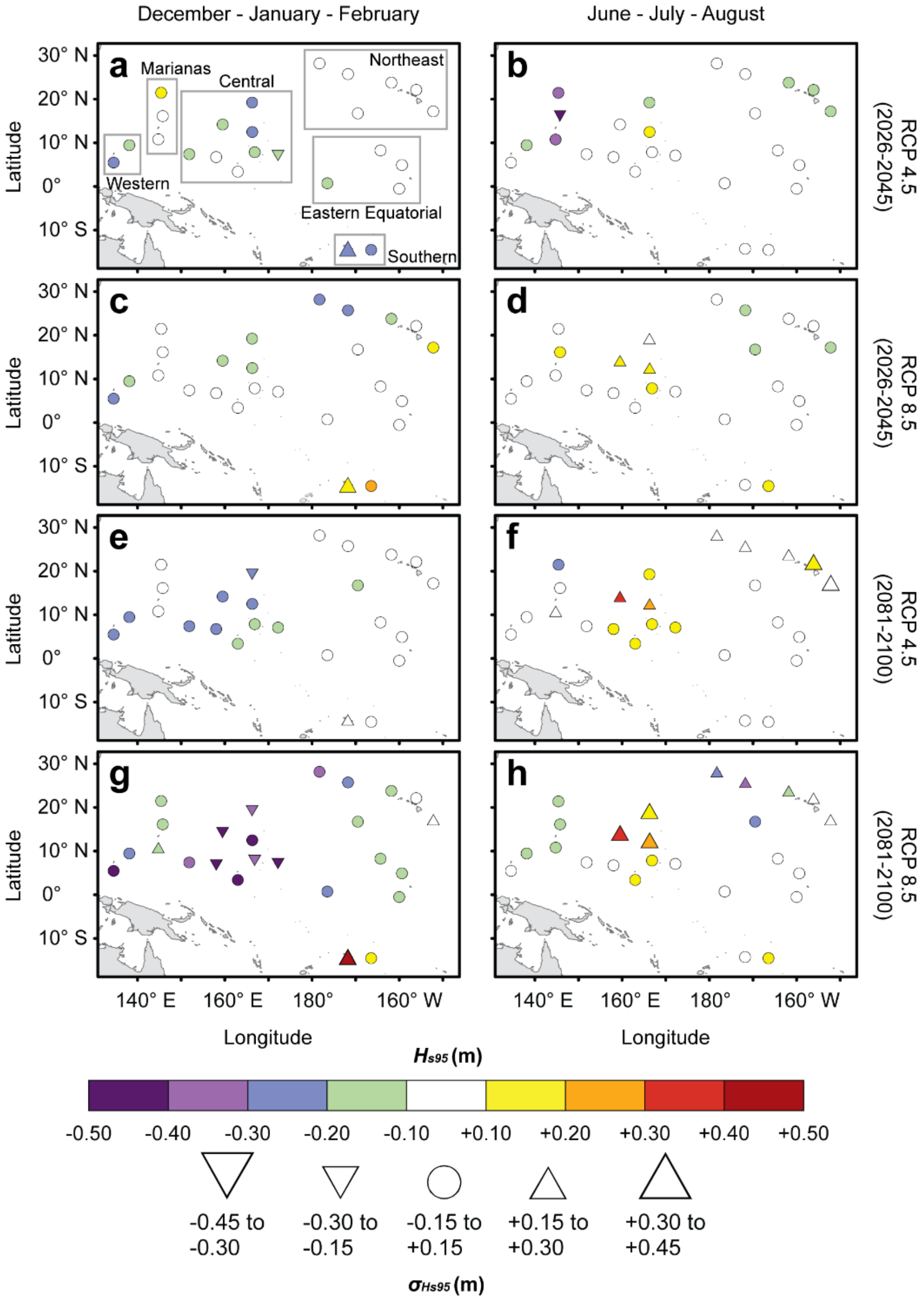

Figure 1-2. Changes in ensemble H_{s95} and the change in σ_{Hs95} from hindcast (1976–2005) values. Change in 2026–2045 from hindcast for RCP 4.5 during (**a**) the DJF season, and (**b**) the JJA season. Change in 2026–2045 from hindcast for RCP 8.5 during (**c**) the DJF season, and (**d**) the JJA season. Change in 2081-2100 from hindcast for RCP 4.5 during (**e**) the DJF season, and (**f**) the JJA season. Change in 2081–2100 from hindcast for RCP 8.5 during (**g**) the DJF season, and (**h**) the JJA season. Colors represent change in H_{s95} in meters and shapes correspond to changes in σ_{Hs95}.

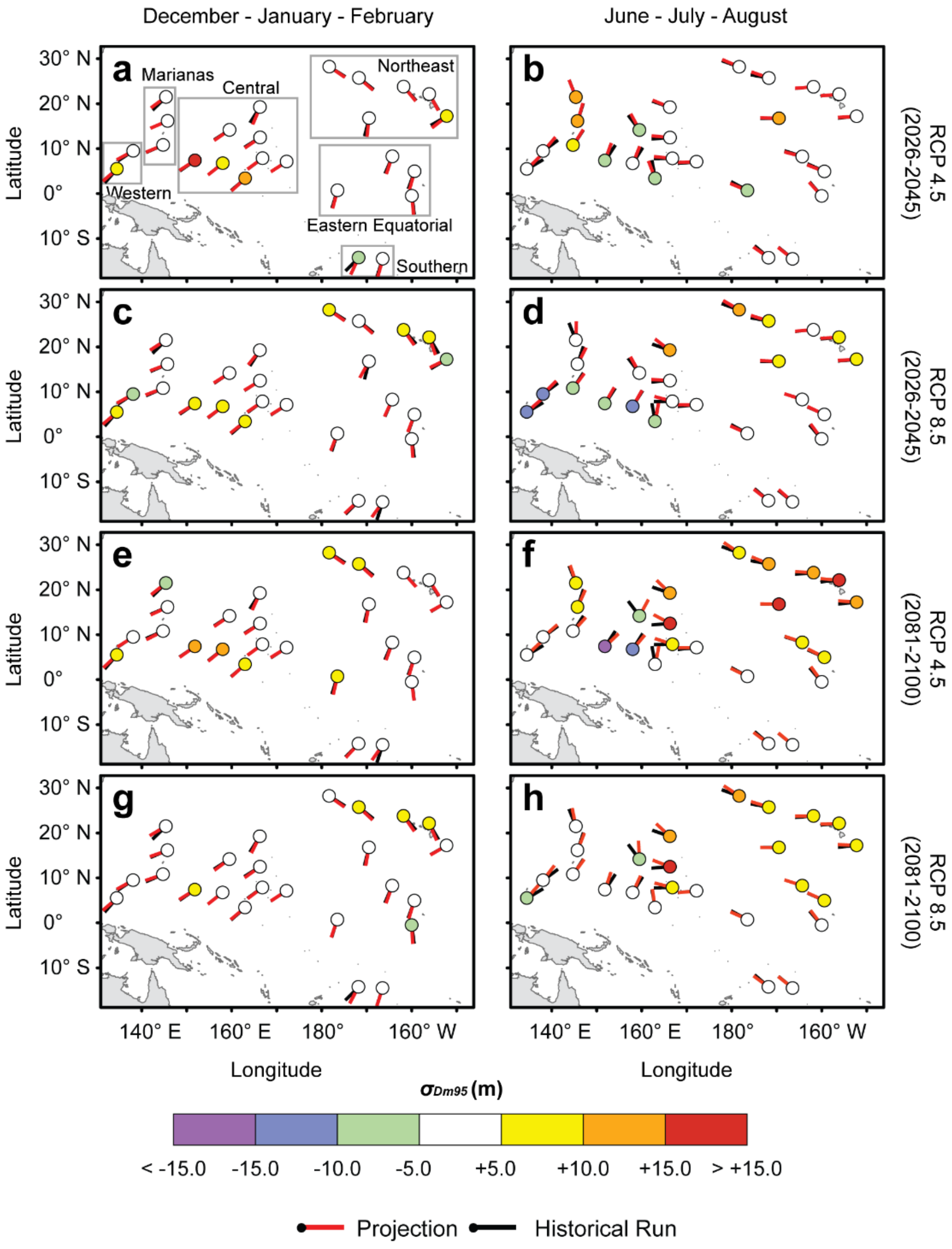

Figure 1-3. Changes in ensemble D_{m95} and the change in σ_{Dm95} from hindcast (1976–2005) values. Change in 2026-2045 from hindcast for RCP 4.5 during (**a**) the DJF season, and (**b**) the JJA season. Change in 2026–2045 from hindcast for RCP 8.5 during (**c**) the DJF season, and (**d**) the JJA season. Change in 2081–2100 from hindcast for RCP 4.5 during (**e**) the DJF season, and (**f**) the JJA season. Change in 2081–2100 from hindcast for RCP 8.5 during (**g**) the DJF season, and (**h**) the JJA season. Black ticks indicate hindcast directions (D_{m95}), blue RCP 4.5 directions, and red RCP8.5 directions. Colors correspond to changes in σ_{Dm95}. Tick orientation indicates wave propagation towards island location.

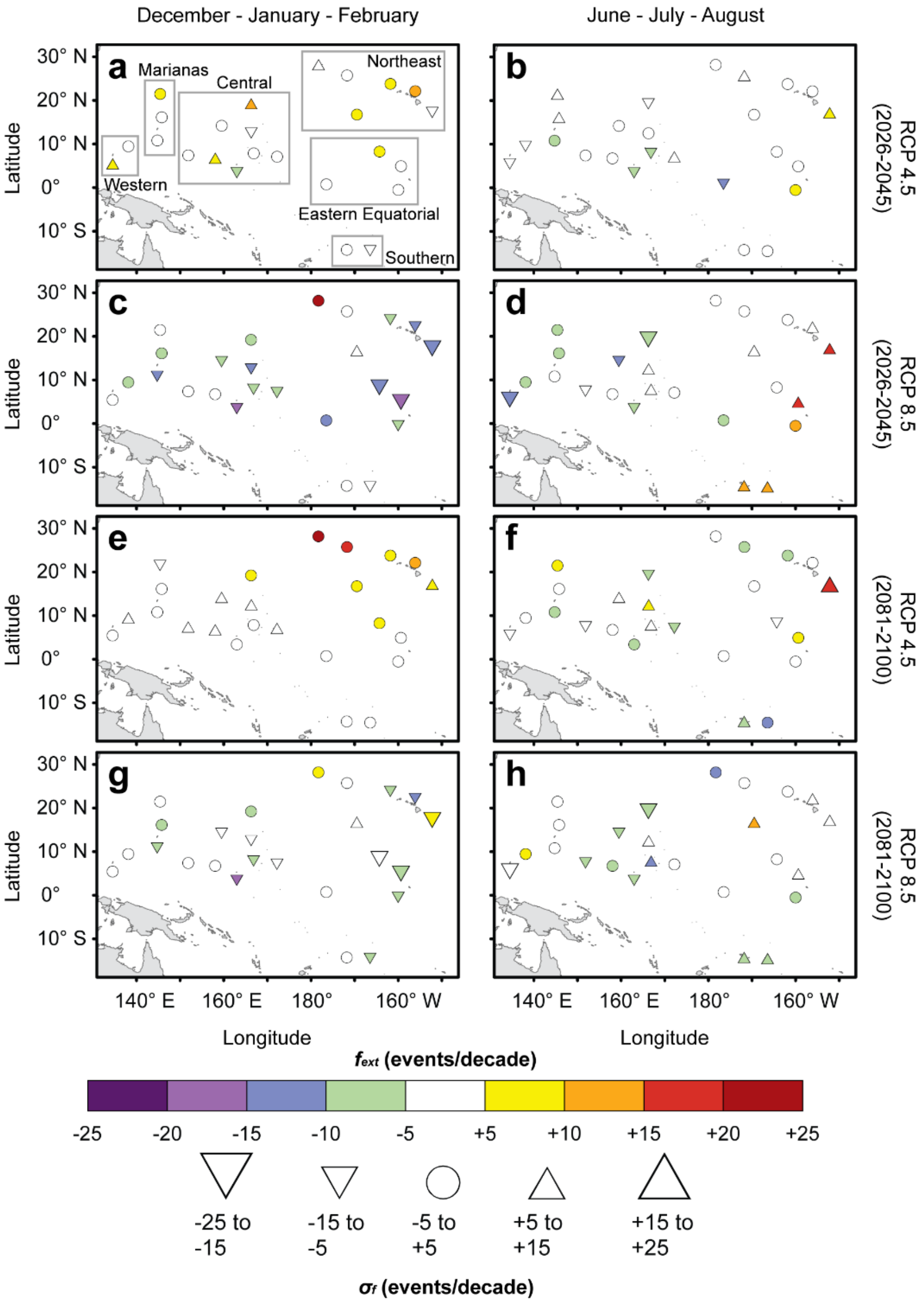

Figure 1-4. Changes in ensemble f_{ext} and the change in σ_f from hindcast (1976–2005) values. Change in 2026–2045 from hindcast for RCP 4.5 during (**a**) the DJF season, and (**b**) the JJA season. Change in 2026-2045 from hindcast for RCP 8.5 during (**c**) the DJF season, and (**d**) the JJA season. Change in 2081–2100 from hindcast for RCP 4.5 during (**e**) the DJF season, and (**f**) the JJA season. Change in 2081–2100 from hindcast for RCP 8.5 during (**g**) the DJF season, and (**h**) the JJA season. Colors represent change in f_{ext} in events/decade and shapes correspond to changes in σ_f.

Table 1-1. List of Global Climate Models used, wave model used, and the model resolutions.

Model	Resolution (longitude x latitude) in Degrees
BCC-CSM1.1	2.8 x 2.8
INM-CM4	2.0 x 1.5
MIROC5	1.4 x 1.4
GFDL-ESM2M	2.5 x 1.5
WAVEWATCHIII	1.25 x 1.00

Table 1-2. Average and standard deviation of H_{s95} and T_{p95} of observed values at selected NDBC stations within the Hawaiian Islands for 1985–2005 and *MAE* values calculated for multi-model hindcast H_{s95} and T_{p95}, at co-located WW3 virtual buoy output points by season. *MAE* statistics are represented in meters (seconds) and as a percentage of mean observed H_{s95} (T_{p95}).

Season	NDBC Station	Averaged H_{s95} (m)	*MAE* H_{s95} (m)	*MAE* H_{s95} (%)	Averaged T_{p95} (s)	*MAE* T_{p95} (s)	*MAE* T_{p95} (%)
DJF	51002	4.53 ± 0.38	0.28	6.1	12.15 ± 3.20	1.61	13.2
	51003	4.60 ± 0.46	0.53	11.5	14.47 ± 4.93	1.30	9.0
	51004	4.52 ± 0.51	0.35	7.7	13.10 ± 3.19	1.73	13.2
JJA	51002	3.19 ± 0.39	0.18	5.6	9.33 ± 1.52	0.48	5.2
	51003	2.75 ± 0.38	0.50	18.2	9.73 ± 2.67	0.40	4.2
	51004	3.18 ± 0.53	0.40	12.5	9.97 ± 2.20	0.32	3.2

Table 1-3. Average and standard deviation of f_{ext} of observed values at selected NDBC stations within the Hawaiian Islands for 1985–2005 and *MAE* values calculated for multi-model hindcast f_{ext}, at co-located WW3 virtual buoy output points by season. *MAE* statistics are represented in events/decade and as a percentage of mean observed f_{ext}.

Season	NDBC Station	Averaged Freq	MAE f_{ext}	
		(events/decade)	(events/decade)	(%)
DJF	51002	177.61 ± 68.50	32.78	18.5
	51003	153.81 ± 50.16	18.50	12.0
	51004	166.84 ± 64.61	40.22	24.1
JJA	51002	130.51 ± 46.64	33.33	25.5
	51003	128.37 ± 41.95	16.79	13.1
	51004	123.14 ± 47.49	7.17	5.8

SUPPLEMENTARY TEXT AND FIGURES

Significance tests

F-test

Within this study, the significance of the trend of H_{s95} data obtained by linear regression was ascertained via an F-test at the 95% confidence level. The null hypothesis of the test is that non-constant coefficients in the regression are zero (the slope of the regression line is not significantly different from flat), and the alternative hypothesis that at least one of the non-constant coefficients in the regression does not equal zero. Here, the simple regression line is in the form $y = mx + b$. where y is the response variable (H_{s95}), x is the predictor variable (time), m is the slope (non-constant coefficient), and b is the intercept with the y axis. Rejecting the null hypothesis implies that the best fit regression line has a significant non-zero slope, and denotes that the trend of the data is significant. The F-statistic is calculated by (Emery and Thomson, 2001):

$$F = \frac{\frac{\sum_{i=1}^{n}(y_i - \widehat{y_i})^2}{\nu_{reg}}}{\frac{\sum_{i=1}^{n}(\bar{y} - \widehat{y_i})^2}{\nu_{res}}} \qquad \text{(S1)}$$

where: y_i is the sample at data point i (here, a yearly H_{s95} value); $\widehat{y}_i$ is the predicted value for y_i at datapoint i; $\bar{y}$ is the mean of the sample data; ν_{reg} is the degrees of freedom of the regressor = number of non-constant coefficients of the model (in a linear regression $\nu_{reg} = 1$), ν_{res} is the degrees of freedom of the residual = $[n-(k+1)]$ n= number of samples and k=number of non-constant coefficients.

Kuiper test

Kuiper's test compares the empirical cumulative distribution functions derived from two sets of directional data and is considered a modification of the Kolgomorov-Smirnov test for circular data (Marida and Jupp, 2009). The test statistic for the 2 sample Kuiper test is given as:

$$V_{n1,n2} = sup_{\theta}\{S_1(\theta) - S_2(\theta)] - inf_{\theta}[S_1(\theta) - S_2(\theta)\} \tag{S2}$$

Where $V_{n1,n2}$ is the test statistic; $S_i(\theta)$ is the empirical cumulative distribution function of the directional data in i, θ ; sup_{θ} is the operator denoting maximum difference between distributions where $S_1 > S_2$; and inf_{θ} is the operator denoting maximum difference between distributions where $S_1 < S_2$. For larger sample sizes, $N > 20$, the statistic is further modified as:

$$V_a = V_{n_1,n_2}\sqrt{N} \tag{S3}$$

Where N is the number of samples in the distribution (Stephens, 1965). But as there are 2 separate distributions, n is modified to be: $N=(N_1N_2)/N_{total}$. The test statistic was then compared to a table of critical values at the 95% confidence level. The null hypothesis states that the two empirical cumulative distribution functions are identical and the alternative hypothesis are that the two distributions are significantly different.

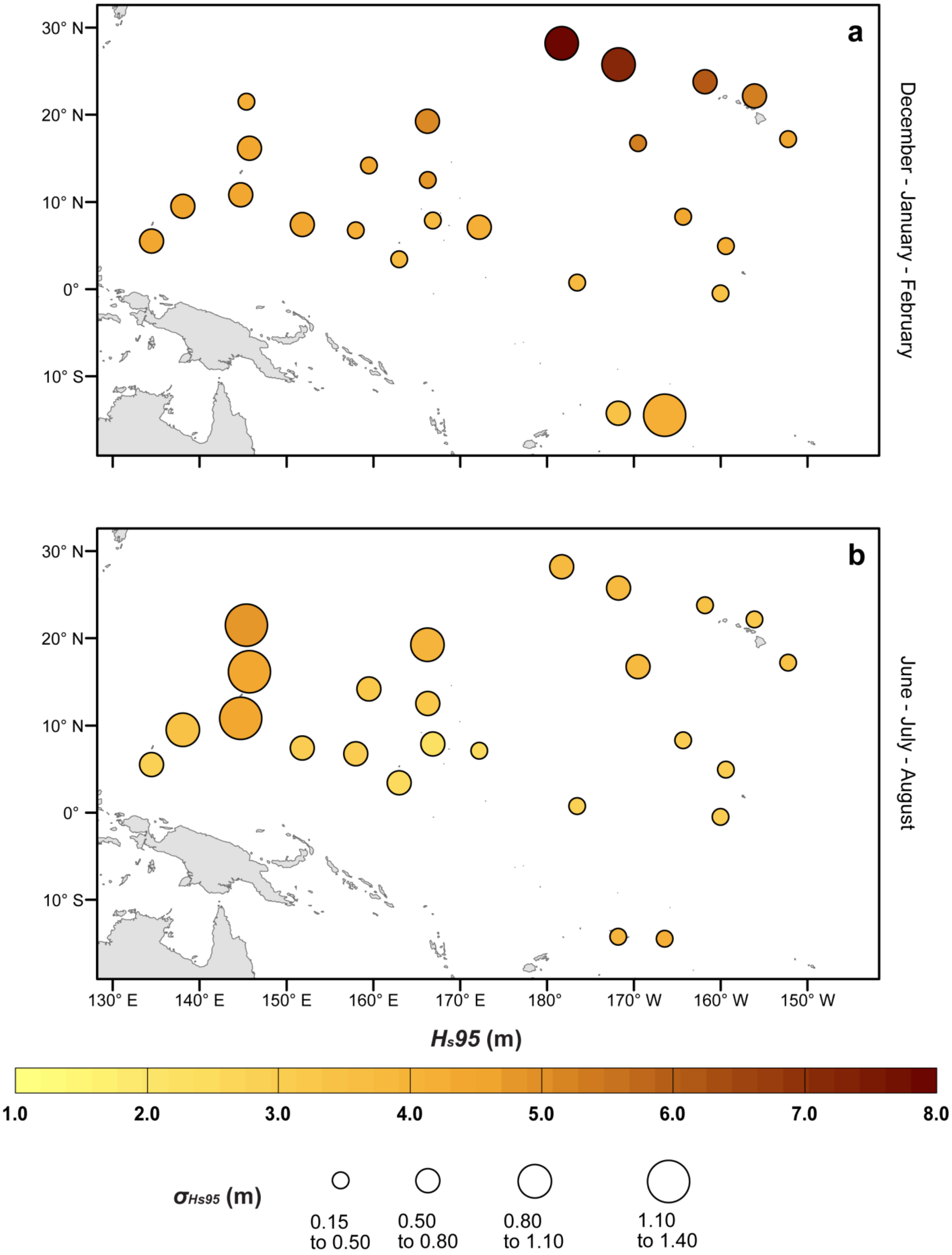

Figure S1-1. Multi-model mean H_{s95} and σ_{Hs95} over the hindcasted period (1976–2005). (**a**) DJF season and (**b**) JJA season. The color ramp represents the magnitude of H_{s95} and the size of each do represents the magnitude of σ_{Hs95}.

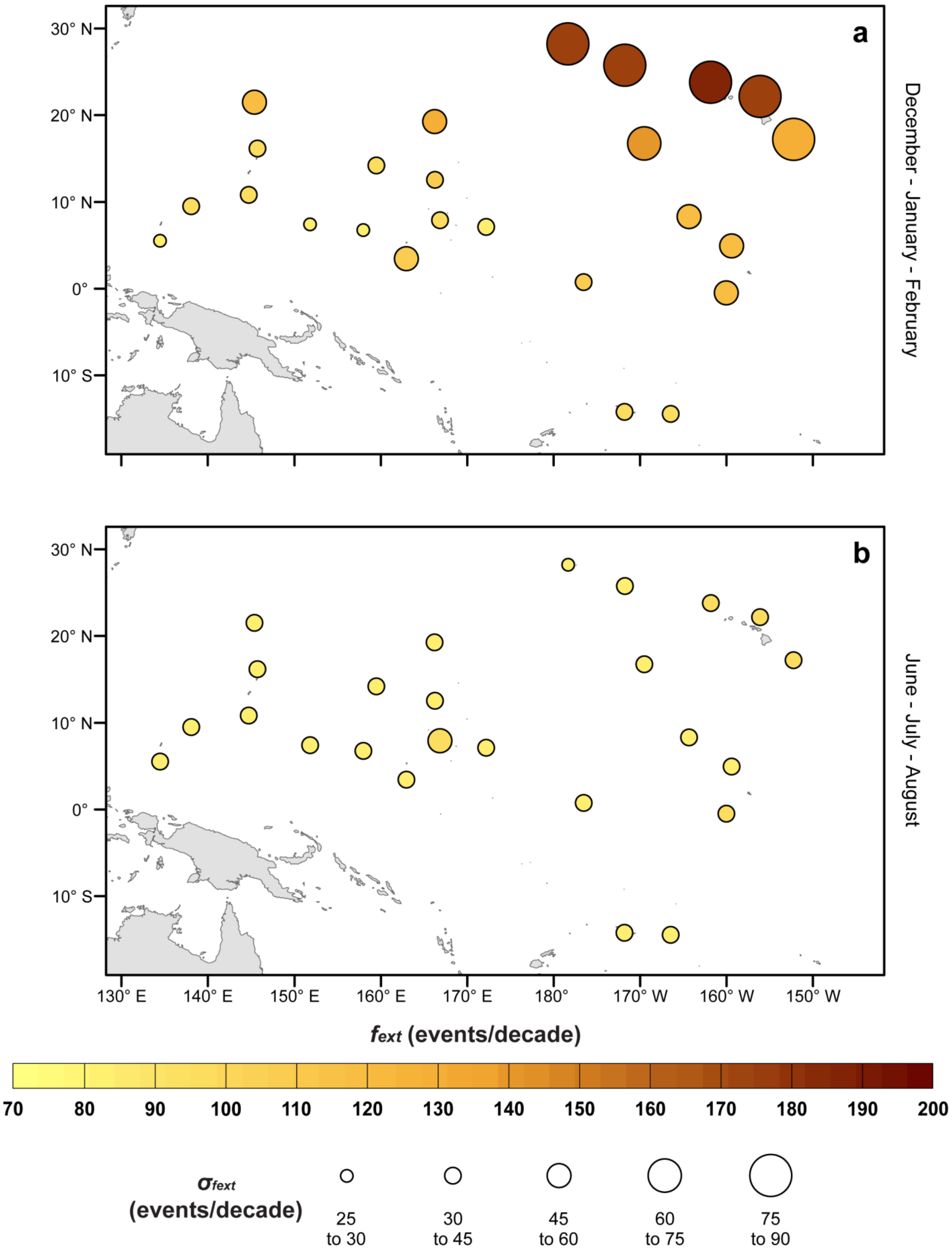

Figure S1-2. Multi-model mean f_{ext} and σ_f over the hindcasted period (1976–2005). (**a**) DJF season and (**b**) JJA season. The color ramp represents the magnitude of f_{ext} and the size of each do represents the magnitude of σ_f.

Chapter Two

PROJECTED ATOLL SHORELINE AND RUN-UP CHANGES IN RESPONSE TO SEA-LEVEL RISE AND VARYING WAVE CONDITIONS AT WAKE AND MIDWAY ATOLLS, NORTHWESTERN HAWAIIN ISLANDS

Submitted: Shope J.B., C.D. Storlazzi, and R.K. Hoeke (2016). Projected atoll shoreline and run-up changes in response to sea-level rise and varying large wave conditions at Wake and Midway Atolls, Northwestern Hawaiian Islands. *Geomorphology,* **In Review.**

Abstract

Atoll islands are dynamic features that respond to seasonal alterations in wave conditions and sea level. It is unclear how shoreline wave run-up and erosion patterns along these low elevation islands will respond to projected sea level rise (SLR) and changes in wave climate over the next century, hindering communities' preparation for the future. To elucidate how these processes may respond to climate change, extreme boreal winter and summer wave conditions under future sea-level rise (SLR) and wave climate scenarios were simulated at two atolls, Wake and Midway, using a shallow-water hydrodynamic model. Nearshore wave conditions were used to compute the potential longshore sediment flux along island shorelines via the CERC empirical formula and wave-driven erosion was calculated as the divergence of the longshore drift; run-up and the locations where the run-up exceed the berm elevation were also determined. SLR is projected to predominantly drive future island morphological change and flooding. Seaward shorelines (i.e., ocean fronted shorelines directly facing incident wave energy) were projected to experience greater erosion and flooding with SLR and as changes in deep water wave directions caused nearshore waves to become more shore normal, increasing wave attack along previously protected shorelines. With SLR, leeward shorelines (i.e., an ocean facing shoreline but sheltered from incident wave energy) became more accretive on windward islands and marginally more erosive along leeward islands. These shorelines became more accretionary and subject to more flooding with nearshore waves becoming more shore normal. Lagoon shorelines demonstrated the greatest

SLR-driven increase in erosion and run-up. They exhibited the greatest relative change with increasing wave heights where both erosion and run-up magnitudes increased. Wider reef flat-fronted seaward shorelines became more accretive as all oceanographic forcing parameters increased in magnitude and exhibited large run-up increases following increasing wave heights. Island end shorelines became subject to increased flooding, erosion at Wake, and accretion at Midway with SLR. Under future conditions, windward and leeward islands are projected to become thinner as ocean facing and lagoonal shorelines erode, with leeward islands becoming more elongate. Island shorelines will change dramatically over the next century as SLR and altered wave climates drive new erosional regimes. It is vital to the sustainability of island communities that the relative magnitudes of these effects are addressed when planning for projected future climates.

2.1 Introduction

Climate change imminently threatens small, reef-lined atoll islands that are home to tens of thousands of people and associated infrastructure, along with dozens of endemic species (e.g. Reynolds et al., 2015). Due to their low elevation (often less than 4 m above sea level), these islands are vulnerable to wave-driven erosion and flooding (Hoeke et al., 2013; Smithers and Hoeke, 2014; Cheriton et al., 2016). Changes in wave climate and particularly sea-level rise (SLR) will likely exacerbate these hazards. Sea level is projected to increase by as much as 1.5–2.0 meters by 2100 due to thermal expansion of seawater and glacial melt in a warming climate (Vermeer and Rhamstorf, 2009; Grinstead et al., 2009; Nicholls and Cazenave, 2010). Presently, the islands' fringing reefs filter most incident wave energy (Ferrario et al., 2014), protecting the shorelines from large waves. SLR will reduce depth-limited breaking of incident waves by fringing reef crests, causing more wave energy to reach island shores (Gourlay, 1996; Pequignet et al., 2011; Hoeke et al., 2015; Taebi and Pattiaratchi, 2014). Larger waves drive greater set-up along the shoreline, increasing run-up and coastal flooding (Becker et al., 2014; Storlazzi et al., 2011, 2015; Quataert et al., 2015). Flooding from large wave events can damage infrastructure, salinize limited freshwater resources, and ruin crops (Mimura, 1999; Yamano et al., 2007; Terry and Falkland, 2010; Hoeke et al., 2013). Large wave events can also cause morphological changes along island coastlines (Smithers and Hoeke, 2014). The pattern of erosion along island shorelines will likely change because greater wave energy causes increased bed shear stresses and sediment flux over the reefs and along the shoreline (Storlazzi et al., 2011; Grady et al., 2013). There have been few studies, however, projecting how atoll islands will morphologically respond to these changes. With SLR, we know that reef-lined atoll shorelines will likely experience greater run-up and flooding (Storlazzi et al., 2015), but there is limited information on how atoll islands' morphologies will respond to changing sea level and wave climates. Projecting how atoll islands will respond to a warming climate is vital so that their communities can best prepare for the future.

Atoll islands are typically dynamic features whose morphology can change quickly in reaction to changing wave conditions (Kench and Brander, 2006; Rankey, 2011; Beetham and Kench, 2014). Kench and Brander (2006) noted that atoll island shoreline morphologies in the Maldives shifted on seasonal timescales following dominant wave direction reversals associated with the Indian monsoon. Although the seasonal fluctuations resulted in limited net annual change, the gross changes in shoreline area between seasons were on the order of thousands of m^2. Webb and Kench (2010) and Yates et al. (2013) similarly found that in response to climate change and historic SLR, many atoll islands within the Central and South Pacific have increased in planform area over the 20th century. It is unknown whether this trend will continue with accelerated SLR projected for the 21st century.

As noted by Webb and Kench (2010), while net island areas appear to have modestly increased over the 20th century, gross changes were much larger. It is unclear whether all atolls' morphology will respond the same way with predicted increased SLR rates. The closest observed analogue to the shoreline impact of increased SLR rates along reef-protected shorelines has been viewed in the form of reef flat degradation. A large coral die off (95% mortality) along fringing reefs in the Seychelles in response to seawater warming created conditions of "pseudo SLR" that reduced reef-induced wave breaking, simulating possible future reef flat conditions with a greater sea level (Sheppard et al., 2005). The shorelines that had been protected by the adjacent fringing reefs experienced wave-driven coastal erosion after the die off. Storlazzi et al. (2011), Grady et al. (2013), and Quataert et al. (2015), using physics-based numerical modeling, forecast similar resulting changes in nearshore wave energy due to coral reef degradation. Whether by reef degradation or increased sea levels, many reefs within the tropical Pacific will likely experience reductions in depth-limited wave breaking with accelerated SLR (Storlazzi et al., 2011; Grady et al., 2013), resulting in similar changes to wave-driven coastal erosion patterns described by Sheppard et al. (2005) and Quataert et al. (2015). Additionally, the growth of new coral will not necessarily abate the wave-driven flooding and erosional hazards from SLR, as reef flat vertical accretion rates in high energy areas are 1–4 mm/yr (Montaggioni, 2005), while the projected rates of SLR through 2100 are 8–16 mm/yr (Grinstead et al, 2009; Nicholls and Cazenave, 2010). As sea levels are rising faster than vertical reef accretion, there will be an increase in water levels over reefs in the future even without reef degradation, and therefore nearshore wave energy will increase due to reduced depth limited breaking on the reef crest and reef flat. With these observations, it is clear that previously stable regions on atoll islands may be subject to large morphological change with SLR. It does not necessarily mean that island areas will decrease, but the islands' shapes or position on the reef flat may change considerably over the next century as SLR enhances shoreline erosional processes.

While previous studies have explored atoll response to SLR hazards (Roy and Connel, 1991, Woodroffe, 2008, Dickinson, 2009, Storlazzi et al., 2015), few have addressed how changing wave climates will interact with SLR to affect atoll island morphology and flooding patterns. Although sea level is an important concern, future projections for atoll islands also need to include the impact of changing wave climates. Recent studies have projected a 5–10% decrease in Northern Hemisphere winter (winter for the remainder of the text) mean significant wave heights (H_s) within the western tropical Pacific by the end of the 21st century (Hemer et al., 2013; Semedo et al., 2013; Wang et al., 2014). Boreal summer (summer for the remainder of the text) mean H_s is projected to increase by approximately 5% in some tropical Pacific regions (Wang et al., 2014). Extreme wave height projections in these regions follow a similar pattern, decreasing during the winter and increasing during the summer (Wang et al., 2014; Shope et al., 2016). Shope et al. (2016) projected changes in the mean of the top 5% of H_s within the mid-to-western tropical Pacific Ocean at many island locations. They found that extreme H_s varied by as much as ± 0.3 m from historical conditions within the western tropical Pacific and the mean direction of these waves could change within the range of ±15°. The projected changes to sea level, extreme H_s, and wave directions have the potential to dramatically impact the run-up, flooding, and erosion patterns along atoll shorelines.

Here we explore the potential effects of SLR and changes in wave climate on atoll island run-up, berm overtopping (and thus island flooding), and erosion patterns. We present results of a coupled hydrodynamic modeling system (Delft3D and SWAN), along with empirical sediment transport and run-up equations, to estimate the changes in these processes in response to changes in wave height, direction, and SLR at two Pacific atolls: Wake and Midway. A general overview of the atolls, with morphologic and wave climate specifics for Wake and Midway, is provided. The Delft3D and SWAN model set-up and run conditions for each atoll and the calculations of run-up, flooding, and accretion/erosion values along each island shoreline are then presented. Finally, the results of changes in shoreline erosion, run-up, and berm overtopping are presented, followed by a discussion of these trends in relation to previous studies. Projections of island change with climate change forcings (SLR and wave climates) are then advanced followed by concluding remarks.

2.2 Study area

2.2.1 Atoll morphology

Atolls are raised carbonate platforms, created from successive episodes of vertical coral reef accretion, found in the tropical regions of the world’s oceans. Atolls are generally characterized by steep offshore bathymetry, with depths rapidly decreasing from kilometers to a few meters at the crest of the atoll reef, and a relatively shallow central lagoon. Waves and currents rework coral rubble and carbonate sediment generated by the reef (Ohde et al., 2002) into islands that are situated atop underpinning mid-Holocene paleoreef flats (Dickinson, 2004). Atoll islands are generally low in elevation, often with mean elevations of 2–3 m above sea level, and are primarily composed of a mixture of unconsolidated carbonate sediment, weakly lithified carbonate sediment (beach rock), and emergent paleoreef material. Many of these islands have high population densities, representing much of the inhabited landmass of many Pacific and Indian Ocean nations, and associated infrastructure (Webb and Kench, 2010; Ford, 2012). These islands are also host a number of endemic species, many of which are threatened or endangered (Reynolds et al., 2015).

Midway (28.2° N, 177.4° W) and Wake (19.25° N, 166.75° W) atolls in the Northwestern Hawaiian Islands (Figure 2-1A) were selected for analysis because there are high-resolution topographic/bathymetric data and future wave climate projections for both atolls (Shope et al., 2016). Midway is on the order of 66 km^2, whereas Wake's area is approximately 32 km^2; these are smaller than most atolls throughout the Pacific (Figure 2-1). Midway has three islands (Sand, East, and Spit) situated along the southern rim of the reef flat. Spit Island is omitted from analysis as it is unvegetated and significantly smaller (0.02 km^2) than the other islands and may react to wave processes differently. The approximate mean elevation of Sand and East Islands is 2.9 m above sea level and the depth of the lagoon exceeds 10 m due to dredging. Wake also has three islands: Peale, Wilkes, and Wake. The islands are aligned along the northern, southern, and eastern rims of the reef flat, respectively. The approximate mean elevation of these islands is 3.5 m above sea level and Wake's lagoon is less than 5 m deep.

2.2.2 Oceanographic forcing

This study assesses the impacts of large wave events on the shorelines of Wake's and Midway's islands during the boreal winter and summer seasons. The largest wave heights at both locations are observed during winter due to Northern Hemisphere extratropical cyclones (Alves, 2006; Semedo et al., 2011). The non-declustered historical (1976–2005) mean of the top 5% of December–February (DJF) significant wave height (H_s) from a global climate model-driven WAVEWATCH III outputs are 7.8±1.0 m for Midway and 5.1±0.6 m for Wake (Shope et al., 2016). The direction of incident waves (θ_w) during the winter approach Midway from the northwest (302±20°) with a mean period (T_m) of 14.4±2 s and Wake from the northeast (33±51°) with a T_m of 12.5±2 s (Shope et al., 2016). Less wave energy occurs during the summer than the winter, with the largest summer waves generated by trade winds and Southern Hemisphere swell from extratropical cyclones (Alves, 2006). The historical mean of the top 5% of June–August (JJA) H_s is 3.6±0.8 m for Midway and 4.0±0.8 m for Wake (Shope et al., 2016). Large summer waves approach both Wake and Midway from the east (109±60° and 110±45°, respectively) with T_m of 12.5±1.3 s and 9.9±2 s, demonstrating the trade winds' dominance on summer wave conditions.

2.3 Methods

2.3.1 Numerical modeling

In this study, the Delft3D modeling suite's FLOW and WAVE modules (Lesser et al., 2004) were used to simulate nearshore hydrodynamics at both atolls. FLOW simulates water levels and currents by numerically solving the Navier-Stokes equations for unsteady flow. WAVE, a version of the Simulating Waves Nearshore (SWAN) spectral wave model (Booij et al., 1999; Ris et al., 1999), simulates wave transformations nearshore by solving the spectral action balance equation. Radiation (total dissipation) stresses calculated by WAVE are passed to FLOW to compute wave-induced residual flow and Stokes drift; the subsequent water levels and currents calculated by FLOW are passed back to the wave module to calculate an updated wave field. Wave propagation over Pacific reefs, including Midway, has been accurately simulated using numerical models (Rogers et al., 2016) including Delft3D and SWAN (Lowe et al., 2009; Hoeke et al., 2011; Taebi and Pattiaratchi, 2014; Storlazzi et al., 2011, 2015). Due to limited *in situ* measurements for validation, the results and validation from Hoeke (2010) and Storlazzi et al. (2015), are used as justification for model setup and application.

Each model run was forced under constant H_s, period, and direction parameters until nearshore water levels and wave heights stabilized (approximately 6 h of model time for Wake and 24 h for Midway). The model boundary forcings were determined from the aforementioned WAVEWATCH III output summarized in Table 2-1 (Shope et al., 2016). The mean of the top 5% of winter and summer non-declustered H_s outputs were selected as model boundary conditions for each run as they represent the largest H_s values of at least 36 h per month. Short duration, high energy events dominate most geomorphic processes nearshore, and this cutoff simulates large wave conditions that are sustained for long enough periods to fully entrain sediment by wave orbital motions (Storlazzi and Reid, 2010), driving significant morphological change, and ensures that these conditions will coincide with high tide for at least part of the month, which would drive greater run-up and sediment transport with increased nearshore wave energy (e.g., Cheriton et al., 2016). To determine the relative impact of each parameter in controlling run-up and erosion patterns along atoll shorelines, H_s, incident wave directions, and sea levels were varied independently between model runs. Incident wave heights were varied over a range of ±0.3 m in 0.1 m increments and θ_w over a range of ±15° in 5° increments from initial conditions to simulate potential changes in average extreme wave conditions by 2100 (Shope et al., 2016). Water levels were varied over a range of 0.0–2.0 m in 0.5 m increments to simulate potential sea-level rise estimates by 2100 (Vermeer and Rhamstorf, 2009; Grinstead et al., 2009; Nicholls and Cazenave, 2010). The model had open water level boundary conditions without astronomical forcing.

2.3.2 Bathymetric/topographic data and model specifications

Most standard Delft3D settings were used per Hoeke (2010) and Storlazzi et al. (2015), and are summarized here. Nested bathymetric and topographic grids were created and used as boundaries for the models. All topographic and bathymetric datasets are referenced to current mean higher water, and will likely remain approximately accurate over the next century due to the slow vertical accretion of reef flats (Montaggioni, 2005) and nominal vertical land motion. Therefore, vertical reef accretion and other potential topographic/bathymetric changes over time were neglected within this study. The large size of Midway atoll necessitated a coarse grid of 50 m resolution (180,851 cells) with a maximum depth of 2,767 m. Finer 10-m resolution grids for Sand and East Islands (73,125 cells and 147,000 cells, respectively) were nested within the coarser grid. Wake is smaller and did not necessitate finer nested grids. The resolution of the Wake grid was 40 m with 52,056 cells; it has a maximum depth of 1,987 m. Different hydrodynamic roughness values for sand and reef areas were used for Midway per Hoeke (2010). A similar hydrodynamic roughness dataset was created for Wake by identifying satellite imagery of reef versus sand coverage. Many of the coral species at Midway are also present at Wake, though the exact percentages differ (Kenyon et al., 2010, 2013). Due to this similarity, it was assumed that the hydrodynamic roughness of Wake's reef would be similar to that of Midway, and the same roughness values for sand and reef cover were used.

2.3.3 Run-up modeling and island overtopping analysis

Both run-up and erosion modeling utilized SWAN outputs at island shorelines. Larger incident waves break at the reef crest but subsequently reform as smaller waves over the reef flat that then break at the shoreline, driving longshore sediment movement and run-up. Run-up was calculated using the van Gent (2001) formulation (equation 1 a-b) for dikes with shallow foreshores, which mimics atoll reef flat and beach morphologies (Quataert et al., 2015). The run-up equation is given as:

$$Z_{2\%} = \gamma H_s\ (c_0 \xi_{s-1}) \qquad for\ \xi_{s-1} \leq p \tag{1a}$$

$$Z_{2\%} = \gamma H_s \left(c_1 - \frac{c_2}{\xi_{s-1}}\right) \qquad for\ \xi_{s-1} \geq p \tag{1b}$$

where: $Z_{2\%}$ is the wave run-up exceeded by 2% of incident waves (m), γ is the reduction factor for wave run-up (1.0 was selected), H_s is significant wave height at the toe of the beach (m), $c_0 = 1.35$, $c_1 = 4.7$, $c_2 = 0.25c_1^2/c_0$, $p = 0.5c_1/c_0$, and ξ_{s-1} is the surf-similarity parameter at the toe of the beach defined as:

$$\xi_{s-1} = \frac{tan(\varphi)}{\sqrt{\frac{2\pi}{g} * H_s T_{m-1}^2}} \tag{2}$$

where: φ = slope of the beach, $g = 9.8$ m/s^2, T_{m-1} = wave period based on the zeroth and first negative spectral moment (s). This empirical run-up formulation was derived by fitting a generalized curve it to a combination of numerical and physical flume model outputs for a variety of wave conditions (van Gent, 2001). The equation was calibrated using the c coefficients to approximate the physical model observations and their values delineated above were derived for use with both long and short period waves. These c coefficients were also specifically to be used with H_s and T_{m-1} variables within the run-up equation (van Gent, 2001).

Beach slope (φ) was calculated using elevation differences between wet coastal grid cells and the nearest inland dry grid cell in the direction of wave propagation. Overtopping was defined as any location where the calculated run-up value exceeded the elevation of the inland cell used to calculate beach slope, representing the berm crest of the beach. Calculating the area of the islands that are flooded by overtopping during the modeled events is beyond the scope of this paper. Flooding values were represented as the fraction of the coastline cells experiencing overtopping.

2.3.4 Divergence of longshore drift modeling

Island erosion patterns were modeled by calculating the instantaneous divergence of the longshore drift of island shorelines. The longshore drift rate was calculated at each shoreline grid cell using the Coastal Research Engineering Center (CERC) equation as formulated by Komar (1971) and Rosati (2002) and used in previous shoreline change studies by, for example, Ashton and Murray (2006) and Adams et al. (2011). Here, values were modified for carbonate sand density and scaling parameters (Equation 2 a-b). The longshore sediment transport rate calculation is:

$$Q_l = \frac{I_l}{(p_s - p_w) g N_O} \tag{3a}$$

$$I_l = K \frac{1}{8} p_w g H_b^2 C n \sin(\alpha) \cos(\alpha) \tag{3b}$$

where Q_l is the longshore sediment transport rate (m^3/s), p_s is the density of carbonate sand (in the absence bulk carbonate sediment density, the bulk density of coral, 1400 kg/m^3, was used (Grigg, 1982; Harney and Fletcher, 2003), p_w is the density of seawater (1024 kg/m^3), N_O is the volumetric concentration of solid grains (0.6), I_l is the immersed weight transport rate, H_b is the breaking wave height at the shoreline (from secondary breaking), C is nearshore wave celerity (m/s), n is the shallow water assumption for wave group velocity (0.5), and α is the local angle of incidence between θ_w and shoreline direction. As with the run-up calculations, SWAN outputs at the cells neighboring the shorelines were used to calculate the longshore sediment transport, as opposed to Adams et al. (2011) where the wave parameters were derived from the breaking wave characteristics at 5 m water depth. Along reef-lined shorelines, incident waves experience breaking at the reef crest and have a second point of breaking in the relatively shallow depths along the island's shoreline. These nearshore wave characteristics, after heavy refraction and energy dissipation from reef crest breaking and subsequent traversal of the rough reef flat, determine nearshore wave-driven sediment dynamics and were utilized to derive erosion/accretion patters. To make magnitudes of longshore drift more realistic for each type of island shoreline, the tuning parameter (K) in equation 2b was varied at each cell following Smith et al. (2009). K was calculated as:

$$K = 0.7\xi_b = 0.7\frac{m}{\sqrt{\frac{H_b}{L_o}}} \qquad (4)$$

where m is the beach slope, H_b is the breaking wave height, and L_o is the wavelength. To better represent breaking wave conditions along atoll shorelines, L_o was defined as the wavelength at each nearshore coastal cell rather than the deep-water wavelength. The calculated *K* values compare favorably with the suggested value for reef-fronted beaches in Hawaii of 0.07 (Eversole and Fletcher, 2002).

Within this study, it is assumed that island shorelines are unconsolidated, despite the physical examples of weakly lithified carbonate sands and carbonate shingle along parts of atoll shorelines that can inhibit wave-driven sediment transport (Vousdoukas et al., 2007). Therefore, the calculated magnitudes of sediment transport are likely greater than using more accurate sediment cover data and shorelines that are projected to change significantly may remain relatively unchanged. Additionally, an instantaneous calculation of the alongshore erosion patterns does not capture the shoreline dynamics that determine the long-term steady-state shoreline shape. During analysis, it was assumed that these instantaneous trends were maintained for a sufficiently long period as to dictate long-term island morphological change. It should be noted that Delft3D does include a sediment transport/evolving morphology module (MOR) that can be coupled to the WAVE and FLOW modules. MOR was not used within this study for a few reasons. The first is that while calculating sediment flux with Delft3D would be more accurate than using the CERC estimate, the computation time for each model run would increase dramatically, limiting the number of scenarios that could be investigated. The CERC formulation is less accurate and lacks cross-shore processes, but it allows for a comparably fast computation of potential erosion/accretion sites. Additionally, there is a lack of spatially-varying sedimentologic and stratigraphic data for Wake and Midway to provide as input for a numerical transport model and field measurements by which to assess the model's accuracy. Finally, the purpose of this research is to gauge the relative changes in alongshore erosion patters under differing forcing conditions and not calculate exact magnitudes, a goal that the CERC formula fulfills. Although the exact transport values presented here may not be accurate, they demonstrate the relative importance of the changes in forcing parameters to the resulting patterns.

The concatenated longshore drift values for each island shoreline were low-pass filtered to remove any variation occurring at the scale of 5% of the alongshore island distance or smaller. This cutoff was determined to be the threshold by which the longshore drift patterns were preserved for each island without being over-generalized. Erosion and accretion values were calculated from the divergence of the longshore drift: $\partial Q_l / \partial x$, where *x* is the alongshore distance (e.g., Pelnard-Considere, 1956). Positive divergence of drift values were defined as locations of erosion and negative of deposition (Figure 2-2). Erosion and accretion were only modeled in the alongshore direction, and did not include cross-shore sediment input or removal from the system. However, Kench and Brander (2006) and Kench et al. (2009) indicated that sediment transport along atoll island shorelines is dominated by alongshore processes, with a decreased emphasis on cross shore transport that more characterizes siliciclastic shorelines. These values were then divided by the model resolution to represent erosion per meter of shoreline (Figure 2-2). Additionally, the CERC formulation assumes an unlimited nearshore sediment supply, but atolls are sediment-limited environments relative to most passive margins/sandy shorelines that would be better approximated by this assumption. Therefore, calculated magnitudes represent potential sediment movement and not a prediction of absolute volumes. An additional caveat of this analysis is that it neglects the role of overwash driven transport of sediment. While beyond the scope of this study, overwash from large waves and the deposition of sediment onshore has been shown to be an important process in vertical island accretion and sediment redistribution along atoll islands (Woodroffe et al., 1999; Kench et al., 2008; Smithers and Hoeke, 2014; McLean and Kench, 2015).

2.3.5 Data analysis

For analysis, individual island shorelines were divided into five types based on island position and exposure to incident wave energy: seaward, leeward, lagoon, island ends, and wide-reef (Figures 2-2, 2-3). Seaward shorelines front the ocean and are exposed to direct incident wave energy and lagoon shorelines face inward toward the lagoon. Leeward shorelines are ocean fronted, but are either oriented away from the deep water θ_w or are sheltered by other islands. The island ends are defined as locations where the islands taper and there is a transition from ocean facing to lagoon shorelines. Finally, wide-reef shorelines are the shorelines fronting the ocean whose reef flats are several times wider than adjacent ocean-facing shorelines of the island. For example, the east coast of East Island at Midway (Figure 2-1B) has a reef flat that is approximately 1 km wide, as opposed to its southern shoreline where the reef flat is on the order of 250–300 m wide. This categorization varied between seasons as θ_w changed. Seasonal mean run-up, net divergence of drift, and the ratio of overtopping cells to total number of cells were calculated for each shoreline type. Net divergence of drift values for each shoreline indicated potential erosion of sediment for an individual shoreline if the values were positive and potential deposition if the net values were negative. Each model output (net erosion rate, mean run-up, and overtopping ratios) was compared to each model input (H_s, θ_w, and sea-level) for each shoreline. The mean trends for each shoreline type with parameter change were calculated. These trends are expressed as the percent change from initial condition means. When interpreting percent changes of divergence of drift values, it is important to note that the shoreline described does not switch from net eroding (accreting) to net accreting (eroding) in most cases, but rather the shoreline erodes (accretes) more or erodes (accretes) less compared to initial conditions. Additionally, the results from Midway and Wake are presented separately, as the trends varied considerably between atolls due to reasons addressed in later sections.

2.4 Results

2.4.1 Sea-level rise

At both atolls, lagoon, seaward, and wide-reef shorelines displayed similar erosional trends (Figures 2-4A, 2-5A). The trends presented within these figures represent the change in the net erosion/accretion values for a specified shoreline type by atoll. For Midway, this means the aggregate sums of both Sand and East Islands’ shorelines and for Wake, the sums of its island's shorelines. With +2.0 m of SLR, lagoon shorelines became more erosive (the greatest erosional increase at both locations), as did seaward shorelines. Wide-reef shorelines became more accretive with increasing sea level. Island ends became increasingly accretive with SLR at Midway, whereas Wake's were erosive for all SLR values but trended towards more accretive with 2.0 m of SLR. Leeward shoreline trends differed, as Wake's became more accretive and Midway's slightly more erosive with 2.0 m of SLR.

Run-up changes at Midway and Wake followed the same pattern: Run-up along all shorelines increased with SLR (Figures 2-4D, 2-5D). Similarly to the erosion/accretion results, the run-up changes were generally greater at Wake than Midway. At Wake, the greatest increases were observed at wide-reef and island end shorelines. At Midway the greatest increases were at lagoon, seaward, and island end shorelines. Following run-up increases, overtopping ratios generally increased with SLR at both locations. At Wake, the greatest changes were along seaward and wide-reef shorelines, with lagoon shorelines experiencing reduced folding with SLR (Figure 2-4G). Midway's greatest change in flooding was along island end shorelines (Figure 2-5G). The remaining shorelines displayed a broad increase in overtopping ratios ranging from 17% to 47%, with leeward shorelines showing the smallest increase after an initial decrease in flooding ratios.

2.4.2 Changing H_s

With increasing H_s, erosion patterns at both atolls generally reacted similarly (Figures 2-4B, 2-5B). Potential erosion increased following increasing H_s for lagoon shorelines at both atolls with +0.3 m H_s, the greatest change at Midway. With -0.3 m H_s, lagoon shorelines became more accretive, though to a much smaller degree at Wake (~1%). Seaward shorelines became more erosive with increasing H_s representing the greatest change at Wake. At both atolls, island ends showed a more complex trend of being more erosive under all wave heights (Midway) or accretive under all wave heights. In general, when one island end is more exposed to wave energy, it erodes, whereas the end on the more sheltered part of the island tends to accrete. Averaging these values results in the comparably muted trends for the island ends. Wide-reef and leeward shorelines experienced more accretion with increasing H_s.

Run-up values increased with increasing H_s and decreased with decreasing H_s (Figures 2-4E, 2-5E). At Wake, the greatest changes were at wide-reef and seaward shorelines. The remaining shorelines changed by less than +/-2%. At Midway, there was more variation, but the increasing trends remained the same. Here, the largest increases were at leeward and lagoon shorelines. The remaining changes were generally less than ±2% from initial conditions. The relatively small changes in run-up resulted in neither Wake nor Midway exhibiting much change in flooding ratios with changing H_s. At Wake, the seaward shorelines were the only ones to show any change, but were less than 1% (Figure 2-4H). At Midway all shorelines did not show significant changes until +0.3 m, where wide-reef, leeward, and island end shorelines' flooding ratios increased by 1–2% (Figure 2-5H).

2.4.3 Changing θ_w

For this analysis, a positive θ_w change indicates wave rotation toward a particular shoreline (more shore normal), and a negative θ_w change indicates wave rotation away from the shoreline (more shore parallel). Waves that are positive-shifted at the model boundary may have positive or negative rotations relative to each individual shoreline. For example, incident winter waves that are shifted clockwise +15° at the model boundary are more shore parallel with the north shore of Wake than the non-shifted waves, so this shift is a –15° rotation for that shoreline. An additional clarification is that the average erosion rate and run-up trends (Figures 2-4C, 2-4F, 2-5C, 2-5F) tended to reverse or level-off at ± 15° when compared to the general trend of the data. The general trends are thought to be more robust than the behavior at the extremes. With large θ_w changes, shorelines may become increasingly protected from incident waves (so that little to no energy reaches the shoreline), or the wave angle of incidence may become too small to generate the same magnitude of sediment transport. When the deep water incident waves are close to shore parallel, the waves experience extreme refraction, especially with the rapid shoaling of the bathymetry along an atoll. This refraction reduces the near shore wave heights, that, in turn, reduce the alongshore sediment transport.

At Wake, seaward shorelines become more erosive with increasing wave exposure (more shore normal incident waves) (Figure 2-4C). Midway's seaward shorelines followed the same trend, but to a smaller degree (Figure 2-5C). Island ends largely experienced more accretion at Midway and more erosion at Wake with increased wave energy exposure. Lagoon shores generally became more accretive with increasing wave energy exposure, though Midway's broadly remained more erosive compared to initial conditions. Midway's leeward shorelines became more erosive with increased shoreline exposure and Wake's trended to become more accretionary, though the values remained positive. At both locations, wide-reef shorelines experienced more accretion with increasing wave energy exposure, with this being the greatest change at Midway for this parameter.

Run-up increased with increasing exposure to wave energy from incident wave reorientation (Figures 2-4F, 2-5F). At Wake, the island end shorelines experienced the greatest increase in run-up with increased exposure to wave attack and leeward shorelines displayed the greatest increase in run-up with increased wave exposure. In general, Midway displayed an increase in flooding ratios with increasing exposure to wave energy, with leeward and seaward shoreline flooding ratios increasing by 4–5% (Figure 2-4I). Wake's shorelines did not show a discernable trend (Figure 2-5I), and most changes observed at Wake were less than 1% except for leeward shorelines, which increased by 2% with increased exposure and by 4% with reduced exposure.

2.5 Discussion

Throughout the results, percent changes in Wake’s divergence of drift and run-up with SLR were larger than those projected for Midway. This is because erosion and run-up values for initial conditions at Midway shorelines were greater than those at Wake, due to differing morphology (Figure 2-1) and oceanographic forcing (Shope et al., 2016). At both atolls, the same magnitude changes were applied, resulting in larger percent changes at Wake than at Midway.

In all scenarios, either from changing incident wave heights, SLR, or from reorientation of incident waves, run-up levels increased. Storlazzi et al. (2015) projected increasing run-up for each island at Midway with increasing water levels and Quataert et al. (2015) for reef-lined shorelines in general. However, these past studies have not reported run-up changes by shoreline type along an atoll. Additionally, there have been discussions and documentation of overtopping on atoll islands in previous studies (Hoeke et al., 2013; Smithers and Hoeke, 2014; Storlazzi et al., 2015), which document increases in overtopping with increasing sea levels and wave heights. However, these studies reported the occurrence of overtopping and did not quantify it as presented here (the ratio of locations where run-up values exceed the elevation of the berm), so a direct comparison of results is difficult.

2.5.1 Sea-level rise

Changes in erosion/accretion due to SLR are generally consistent with previous studies' findings. Webb and Kench (2010) found that in response to climate change, the windward side of atolls eroded. At both Wake and Midway, seaward shorelines became more erosive with increasing sea level (Figures 2-4A, 2-5A). Leeward shorelines showed a more complex pattern. In previous studies, these shorelines generally showed an accreting trend in response to historical SLR (Woodroffe, 2008; Webb and Kench, 2010). Leeward accreting trends were only observed on Wake (Figure 2-4A), where sediment is mobilized along the seaward (east) shoreline and is deposited along leeward shorelines. At Midway, the trend is different. Midway's leeward shorelines were the southern ends of Sand and East during the winter; these shorelines became more erosive despite being on the leeward side of the atoll (Figure 2-5A). The southern shorelines of these islands experience larger waves compared to other shorelines types during the winter because of the narrower reef flats fronting them compared to the other parts of the islands. Despite being leeward, these shorelines act more like seaward shorelines, becoming more erosive with SLR, contrary to long-term accretional trends noted by Woodroffe (2008) for ocean-facing shorelines. In contrast to some observed historical changes (Webb and Kench, 2010) of lagoon shorelines being stable or accretive with historical SLR, modeled SLR resulted in increased lagoonal erosion (Figures 2-4A, 2-5A), as noted at some atoll shorelines by Woodroffe (2008), Ford (2012), and Yates et al. (2013). Accelerated SLR is projected to result in more sediment mobilization along reef-lined shorelines

(Storlazzi et al., 2011; Grady et al., 2013), which can account for the increase in erosion along lagoon shorelines. Purkis et al. (2016) found that lagoon shorelines had the most dynamic erosional shifts in response to climate change at Diego Garcia, indicating that lagoon shoreline stability is not assured with SLR. Within this study, the sediment eroded from lagoon, seaward, Midway's leeward, and Wake's island end shorelines is transported to Midway's island end, Wake's leeward shorelines, and both atolls' wide-reef shorelines. These differing trends indicate that individual shoreline response to accelerated SLR may be more complex compared to the past trends outlined by Woodroffe (2008) and Webb and Kench (2010), with island and shoreline position in relation to the dominant θ_w needing to be considered when projecting future morphological change. An additional complication that is beyond the scope of this work will be island and shoreline response to overwash and onshore sedimentation from large waves (Kench et al., 2008; Smithers and Hoeke, 2014; McLean and Kench, 2015). Islands may be subject to more overwash in the future due to SLR, increasing onshore transport and altering nearshore sediment budgets, resulting differing morphological changes than from alongshore processes alone.

It should be noted that most island ends encompass some portion of both ocean- and lagoon-facing shorelines. These types of island ends, although net accreting at Midway and eroding at Wake with +2.0 m SLR, tend to have zones of erosion on their seaward sections and accrete more along lagoon-facing sections. This pattern could account for observations of lagoon accretion in previous studies. The results from this study only delineate short-term trends. Although much of island morphology can be dominated by larger events, such as storms (Woodroffe, 2008), slower processes over decades could result in marked differences from projected erosion patterns. Another caveat is that these changes to sea level were instantaneous within the model and did not include island adjustment over time. Island morphology will likely change with gradual SLR and erosion patterns will change accordingly.

With SLR, the wide-reef, island end (at Midway), and leeward (at Wake) shorelines became more accretive (Figures 2-4A, 2-5A). Along these shorelines, accretion was due to the alongshore wave energy gradients influenced by reef flat morphology and shoreline orientation. Sediment was mobilized along the more energetic seaward shorelines, which had a narrower reef flat, and was transported towards regions with wider reef flats or reduced wave energy. As the reef flat increases in front of the shoreline either by becoming wider or the shoreline tapering to an end, wave heights and resulting sediment transport capacity decreased, resulting in sediment deposition along these shorelines. A similar process occurs along Wake’s leeward shorelines, with decreasing wave energy alongshore relative to seaward shorelines resulting in greater deposition.

The greatest increases in run-up were along shorelines that were initially protected from wave attack by wider reef flats (island end, lagoon, and Wake’s wide-reef shorelines; Figures 2-4D, 2-5D). With SLR, larger waves propagate over the deeper reef crest and reef flat, generating greater run-up along the shoreline (Storlazzi et al., 2011; Quataert et al., 2015). These previously well-protected areas experience a more dramatic increase in run-up from initial values compared to ocean-fronted shorelines with narrower reefs, indicating that these regions will become subject to more flooding in the future. The increase in Midway's wide-reef run-up was not relatively greater compared to other shorelines despite being protected by a wider reef flat. This difference is due to the initial depth of Midway's reef flat (~2–3.5m), and the depth increase due to SLR would not necessarily result much larger nearshore wave height increases compared to other shoreline types. Overtopping ratios similarly generally increased with SLR (Figures 2-4G, 2-5G) following Storlazzi et al. (2015), though many show an initial decrease in flooding at +1.0 m of SLR. The Wake lagoon and Midway leeward shorelines were an exception, along which less island area flooded. Additionally, the overtopping ratios at Wake decreased with +2.0 m of SLR. These deviations are due to sea level: As the islands are inundated from SLR, the coastline recedes inland, presenting greater topographical variation at the new shoreline and preventing run-up values from exceeding the elevation of these inland locations. The lagoon shorelines at Wake have relatively low slopes and are inundated over a large extent by SLR; under SLR scenarios, however, the run-up is then interacting with higher coastal topography further inland. Midway's leeward shorelines are generally steeper and elevations increase more rapidly inland, resulting in less flooding. At +2.0 m of SLR, all the shorelines of Wake experience this process. Shoreline cells defined for lower sea levels are permanently inundated, and the new shorelines cells neighbor inland cells with a greater elevation compared to the +1.5 m SLR scenario and the calculated run-up does not exceed the elevation of these new inland cells.

2.5.2 Changing H_s

With increasing H_s, shoreline erosion increased along many shorelines (Figures 2-4B, 2-5B). The exceptions were the wide-reef and leeward shorelines. Increasing H_s at the boundary of the model results in increased set-up and larger waves over the reef flat (Gourlay, 1996; Becker et al., 2014; Cheriton et al., 2016), mobilizing more sediment. This results in proportionally more erosion along seaward, lagoon, and some island end shorelines. The aforementioned accretive shorelines act as the catchment for the mobilized sediment, where the increase in wave energy is not as large due to width of the reef flat and shoreline position. Additionally, the increased wave energy mobilizes more sediment along lagoon shorelines. This erosional trend along lagoonal shorelines may not extend to extremely large waves. Smithers and Hoeke (2014) noted that in response to a large overwash event from extra-tropical cyclone swell, Nukutoa Island experienced erosion along most shorelines, with accretion along lagoonal spits, similar to the accretionary trend of Wake’s lagoon. However, by the schematization in this research, these areas of accretion would likely have been included in the island end averages, indicating erosion of island ends and transfer of sediment to the lagoon may dominate at larger wave height scales.

Increasing H_s at the boundary of the model increased offshore wave heights, but due to depth-limited breaking, increases in H_s along the shoreline and associated run-up were relatively small (Figures 2-4E, 2-5E). Larger waves break and dissipate more energy at the reef crest, whereas smaller waves are able to bypass the crest and traverse the reef flat along with the residual energy from the broken waves. Additionally, the rough reef flat further dissipates much of the incident wave energy, which culminates into much smaller wave heights at the shoreline. It is important to note that DelftD and SWAN do not simulate infragravity wave dynamics and the impacts infragravity waves are beyond the scope of this analysis of wave driven run-up and sediment transport. The inclusion of infragravity waves could affect run-up (Quataert et al., 2015) and overwash deposition magnitudes, as these waves become a larger proportion of nearshore wave energy along shorelines with narrow (~100 m) reef flats (Ford et al, 2013), as seen along many Pacific island coastlines (Hoeke et al., 2013; Smithers and Hoeke, 2014, Cheriton et al., 2016). However, it is unlikely that these waves would significantly impact calculated nearshore sediment transport due to low bottom shear stresses (van Dongeren et al., 2013; Pomeroy et al., 2015). Wide-reef and seaward shorelines saw the greatest H_s increases at Wake, as other shorelines remained well protected from wave attack. At Midway, leeward and lagoon shorelines exhibited the greatest changes in run-up (Figure 2-5E) as smaller perturbations in incident wave heights appear to have a greater proportional impact on more well-protected shorelines with the deeper reef flats at Midway. The deeper reef flats allow comparably more wave energy to reach these protected areas than at

Wake, and the small changes in incident energy have a comparably greater impact on the run-up. Lagoon shorelines at Midway experienced slightly higher run-up values because of the channel in the reef rim in the northwest portion of the atoll (Figure 2-1B) that allows larger waves to filter into the lagoon with reduced depth-limited breaking. These small changes in run-up resulted in mostly negligible (~3%) changes to overtopping ratios for all shorelines (Figures 2-4H, 2-5H). Overall, small changes to H_s had a negligible effect on run-up and overtopping values along atoll islands in the absence of SLR.

2.5.3 Changing θ_w

Kench and Brander (2006) and Kench et al. (2009) noted that Maldivian atoll island shorelines can oscillate greatly between the monsoon seasons. They identified changes in θ_w as the greatest factor driving changes to island shorelines on the seasonal to annual scale. Similarly, Figures 2-4C and 2-5C demonstrate that erosion/accretion changes were greater under changing θ_w than with changing H_s. Generally, when exposed to more wave energy, an individual shoreline became more erosive, and when more sheltered from incident wave attack, more accretive. This process mimics the motion of sediment reported by Kench et al. (2009), whereby the sediment migrated alongshore towards the leeward shorelines between monsoon seasons. Wide-reef, lagoon, Midway's island ends, and Wake's leeward shorelines showed accreting trends when exposed to increased wave energy. At Midway, when the island ends and wide-reef shorelines were exposed to more wave energy, so too were neighboring ocean facing shorelines, which become more erosive. Assuming that these trends are maintained over longer periods of time and are the dominant processes shaping the coastline, the sediment sourced from these shorelines would migrate to these areas of comparatively lower energy (the island ends), where it would be deposited. At Wake, a similar process prevailed; here, the eroding island end, lagoon, and seaward shorelines acted as a source of sediment for the leeward and wide-reef shorelines. This process is especially evident at the southern shoreline of Wake, which became much more accretive in response to the eastern seaward shoreline becoming more erosive, this trend was especially evident during winter conditions.

With increasing shoreline exposure to wave attack (becoming less leeward), run-up and many overtopping ratios increased (Figures 2-4F, 2-4I, 2-5F, 2-5I). Leeward shorelines exemplify this trend. With the reorientation of incident θ_w more perpendicular to a leeward shoreline (especially at Wake during the summer), these shorelines become seaward shorelines and the run-up increases dramatically, though overtopping ratios do not necessarily follow this trend (Figures 2-4F, 2-4I). Given the projected changes to incident extreme θ_w (Shope et al., 2016), atoll shorelines will likely see significant changes to flooding hazards under future wave climates, particularly along currently leeward shorelines, though these results suggest that the change in the number overtopping locations alongshore will not be dramatic, increasing by 1–5% at Midway; instead, flooding hazards along current flooding locations will increase.

2.5.4 Island stability and schematic for morphological change

For atoll islands overall, SLR will likely be the dominant factor in causing future run-up and erosion changes, and changing θ_w will likely play a smaller role. Future changes in mean extreme H_s have been projected to be relatively small (<0.30 m, Shope et al., 2016), and are projected to negligibly alter island morphologies and run-up compared to other parameters. Schematizing these results provides a rough guideline of how different atoll islands may change under various forcing conditions (Figure 2-6). This schematization assumes that the baseline wave processes (mean H_s and θ_w for each season) remains the same and only these extreme H_s events change in the future. It also assumes that the instantaneous erosional trends are maintained over long periods and are the primary driver of morphological change. It also assumes that with SLR, the islands' overall position would remain approximately stable on the reef flat rim.

Seaward and lagoon shores are projected to erode with SLR (Figure 2-6B). Leeward shorelines will generally accrete, provided there is a neighboring seaward shoreline or erosive island end. For example, leeward shorelines on Wake and Midway responded differently to SLR due to their differing configuration (see above). Wide-reef shorelines are projected to accrete as sediment mobilized from other ocean-facing shorelines is deposited here. The trends of island ends will likely depend on the erosional trends along nearby shorelines and whether the island is on the windward or leeward rim of the atoll as Wake's broadly became more erosive and Midway's more accretive. It appears as though islands may not necessarily migrate across the reef flat towards the lagoon in response to SLR as seen in some historical observations (Webb and Kench, 2010), but rather they will become thinner and more elongate, accreting towards their longitudinal ends and non- seaward shorelines, possibly shifting toward the leeward side of the atoll. However, these trends assume no overwash deposition, which would likely modify the island erosional patterns and the process of moving sediment onshore could result in net island lagoonward migration.

With increasing H_s, seaward and lagoon shorelines are projected to become more erosive, whereas leeward and wide-reef shorelines become more accretive as the alongshore carrying capacity decreases with reduced wave energy compared to more exposed shorelines (Figure 2-6C). The increased wave energy drives sediment transport around the leeward island from the lagoon and island end shorelines towards its leeward shoreline. Seaward islands become wider along non-seaward, ocean-facing shorelines, accreting towards leeward, wide-reef shorelines. Island end shorelines in both cases have a more muted response. Generally, seaward island ends erode while the more leeward ends accrete, on average making seaward islands slightly longer and leeward slightly shorter as they both extend away from the direction of wave forcing. And generally, leeward islands appear to migrate toward the reef rim. Decreasing H_s is projected to generate opposite patterns (Figure 2-6D).

A 15° clockwise shift in θ_w erodes the newly exposed leeward shorelines of leeward islands and their lagoon shorelines (Figure 2-6E). The leeward island end in the direction of wave rotation will accrete and the other will erode. Along seaward islands, the seaward, leeward, and lagoon shorelines accrete as sediment mobilized along the now more seaward island end shorelines and corners between shoreline types, where the shoreline direction changes dramatically, is transported to these areas. The wide-reef shoreline that becomes more leeward will tend to erode due to the lack of sediment from the seaward shoreline being carried to the lower energy location. The more exposed island ends erode due to a higher angle of incidence and the nearby leeward or lagoon shorelines accrete, though the lagoons overall tend to erode. The opposite generally occurs when θ_w rotates counterclockwise (Figure 2-6F), except leeward island lagoon shorelines continue to accrete and leeward shorelines continue to erode as they become less protected by the remainder of the island from incident wave attack under this scenario as well. In both scenarios, leeward islands appear to migrate lagoonward when exposed to more wave attack.

2.6 Conclusions

Atoll island shorelines are dynamic and will likely change under new forcing conditions (Kench and Brander, 2006; Rankey, 2011; Beetham and Kench, 2014).

The results presented here suggest that projected SLR (higher rise rates than previous studies) will be a greater force of change to atoll island morphology in the future than due to changes in H_s or θ_w, as erosion/accretion values demonstrated the greatest deviation from initial conditions with SLR. With SLR, seaward islands are anticipated to become thinner along seaward and lagoon shorelines, accreting towards leeward, and wide-reef effectively creating longer, thinner islands. Leeward islands are expected to follow a similar pattern of becoming thinner and more elongate. Shifts in incident θ_w and small changes to H_s slightly modify these larger, SLR-driven changes, with changing θ_w playing a more important role. Whether the erosional changes presented within this study will result in significant island migration across the reef flat is currently unknown.

A schematized summary of morphological change (Figure 2-6) for the different changes in forcing shows that erosion/accretion patterns shift with alongshore wave energy gradients dictated by island and reef morphology. For example, wide-reef and leeward shorelines were consistently regions of increased accretion when neighboring seaward shorelines and the corners of the island (for example, Wake’s southeast corner, experienced greater wave attack and became more erosive). A wide reef flat generally attenuates enough wave energy such that the carry capacity of longshore drift decreases along wide-reef shorelines compared to shorelines with a narrower reef flat (Grady et al., 2013), and similarly the wave energy gradient decreases along leeward shorelines, resulting in accretion along these shorelines when neighboring a seaward shoreline. Increasing wave energy along seaward shorelines increases the wave energy gradient between the seaward and wide-reef / leeward shorelines. Therefore when seaward shorelines become more erosive, the extra mobilized sediment is deposited in these relative calmer environments.

Shoreline change patterns calculated using the CERC formulation with Delft3D output seemed to compare favorably with patterns of island change noted in previous studies (Beetham and Kench, 2014). It is again important to note a number of limitations of this method. CERC assumes an infinite amount of unconsolidated (sand-sized) material. In these sediment-limited environments with outcroppings of beach rock and conglomerate, absolute magnitudes of erosion/accretion along a shoreline are likely erroneous. However, the relative changes of these erosion potential values under differing conditions elucidate how islands may change under new forcing conditions. A second caveat is that this analysis disregards manmade structures on the islands (such as seawalls or groins) that alter projected changes. Finally, the sediment transport was only calculated in the alongshore direction. Cross-shore transport and the deposition of sediment onshore from large wave overwash were neglected, which can alter erosional pattern by sequestering sediment onshore and transport sediment towards the lagoon. The exact role of island morphology as a control on island erosion and flooding patterns will need to be studied further. This study provides insight into longshore sediment transport in relation to reef flat width (seaward vs. wide-reef shorelines) and depth (Wake vs. Midway) at atoll islands.

However, future studies will need to model changes to island morphology and varying reef flat characteristics, and island morphology to adequately assess the relative importance of morphological factors.

Future projections of run-up followed an intuitive pattern: larger nearshore wave heights led to more run-up and usually more inland flooding. Using the results of Shope et al. (2016), whereby extreme H_s are generally projected to decrease in the western tropical Pacific but θ_w may change dramatically, run-up will continue to cause flooding along Pacific atoll islands over the next century, but the shorelines that are currently protected may see greater amounts of run-up and damage from more consistent exposure to large waves and SLR.

Acknowledgements

This work was carried out under the USGS's Pacific Coral Reef Project as part of an effort in the United States and its trust territories to better understand the effect of geologic and oceanographic processes on coral reef systems and the USGS's Climate Change Impacts to the U.S. Pacific and Arctic Coasts Project to understand the impact of climate change on U.S. and U.S.-affiliated island shorelines. This project was funded by the USGS's Coastal and Marine Geology Program and Department of Defense's Strategic Environmental Research and Development Program (SERDP) under RC-2334. P. Limber (USGS) contributed numerous excellent suggestions and a timely review of our work. Use of trademark names does not imply USGS endorsement of products.

References

Adams, P. N., D. L. Inman, and J. L. Lovering (2011), Effects of climate change and wave direction on longshore sediment transport patterns in Southern California, *Clim. Change, 109,* 211–228, doi:10.1007/s10584-011-0317-0.

Alves, J. (2006), Numerical modeling of ocean swell contributions to the global wind-wave climate, *Ocean Model., 11*(1–2), 98–122, doi:10.1016/j.ocemod.2004.11.007.

Ashton, A. D., & Murray, A. B. (2006). High-angle wave instability and emergent shoreline shapes: 1. Modeling of sand waves, flying spits, and capes. *Journal of Geophysical Research: Earth Surface, 111*(F4).

Aucan, J., R. Hoeke, and M. A. Merrifield (2012), Wave-driven sea level anomalies at the Midway tide gauge as an index of North Pacific storminess over the past 60 years, *Geophys. Res. Lett., 39*, L17603, doi:10.1029/2012GL052993.

Becker, J. M., M. A. Merrifield, and M. Ford (2014), Water level effects on breaking wave setup for Pacific Island fringing reefs, *J. Geophys. Res.-Oceans, 119*(2), 914–932, doi:10.1002/2013JC009373.

Beetham, E., P. S. Kench, J. O'Callaghan, and S. Popinet (2016), Wave transformation and shoreline water level on Funafuti Atoll, Tuvalu, *J. Geophys. Res.-Oceans, 121*(1), 311–326, doi:10.1002/2015JC011246.

Beetham, E. P., and P. S. Kench (2014), Wave energy gradients and shoreline change on Vabbinfaru platform, Maldives, *Geomorphology, 209*, 98–110, doi:10.1016/j.geomorph.2013.11.029.

Booij, N., R. C. Ris, and L. H. Holthuijsen (1999), A third-generation wave model for coastal regions - 1. Model description and validation, *J. Geophys. Res.-Oceans, 104*(C4), 7649–7666, doi:10.1029/98JC02622.

Cheriton, O. M, C. D. Storlazzi, K. J. Rosenberger (2016), Observations of wave transformation over a fringing coral reef and the importance of low-frequency waves and offshore water levels to runup, overwash, and coastal flooding, J. *Geophys. Res.-Oceans, 121*(5), 3121–3140, doi:10.1002/2015JC011231.

Collen, J. D., D. W. Garton, and J. P. A. Gardner (2009), Shoreline Changes and Sediment Redistribution at Palmyra Atoll (Equatorial Pacific Ocean): 1874–Present, *J. Coast. Res., 253*, 711–722, doi:10.2112/08-1007.1.

Dickinson, W. (2004), Impacts of eustasy and hydro-isostasy on the evolution and landforms of Pacific atolls, *Palaeogeogr. Palaeoclimatol. Palaeoecol., 213*(3–4), 251–269, doi:10.1016/j.palaeo.2004.07.012.

Dickinson, W. R. (2009), Pacific Atoll Living: How Long Already and Until When, *GSA Today*, *19*(3), 4, doi:10.1130/GSATG35A.1.

Van Dongeren, A., Lowe, R., Pomeroy, A., Trang, D., Roelvink, D., Symonds, G., and R. Ranasinghe (2013), Numerical modeling of low-frequency wave dynamics over a fringing coral reef, *Coast. Eng., 73*, 178–190, doi:10.1016/j.coastaleng.2012.11.004.

Eversole, D., and C. H. Fletcher (2003), Longshore sediment transport rates on a reef-fronted beach: field data and empirical models Kaanapali Beach, Hawaii, *J. Coast. Res.*, 649–663.

Ferrario, F., M. W. Beck, C. D. Storlazzi, F. Micheli, C. C. Shepard, and L. Airoldi (2014), The effectiveness of coral reefs for coastal hazard risk reduction and adaptation, *Nat. Commun., 5*, 3794, doi:10.1038/ncomms4794.

Ford, M. (2012), Shoreline Changes on an Urban Atoll in the Central Pacific Ocean: Majuro Atoll, Marshall Islands, *J. Coast. Res., 28*(1), 11–22, doi:10.2112/JCOASTRES-D-11-00008.1.

Ford, M., Becker, J., and M. Merrifield (2013), Reef flat wave processes and excavation pits: observations and implications for Majuro Atoll, Marshall Islands, *J. Coast. Res., 29*(3), 545–554, doi:10.2112/JCOASTRES-D-12-00097.1.

van Gent, M. R. A. (2001), Wave Runup on Dikes with Shallow Foreshores, J. Waterw. Port Coast. *Ocean Eng., 127*(5), 254–262, doi:10.1061/(ASCE)0733-950X(2001)127:5(254).

Gourlay, M. R. (1996), Wave set-up on coral reefs. S. Set-up on reefs with various profiles, *Coast. Eng., 28*, 17–55.

Grady, A. E., L. J. Moore, C. D. Storlazzi, E. Elias, and M. A. Reidenbach (2013), The influence of sea level rise and changes in fringing reef morphology on gradients in alongshore sediment transport, *Geophys. Res. Lett., 40*(12), 3096–3101, doi:10.1002/grl.50577.

Grigg, R. W. (1982), Darwin point: a threshold for atoll formation, *Coral Reefs, 1*, 29–34. doi:10.1007/BF00286537.

Grinsted, A., J. C. Moore, and S. Jevrejeva (2010), Reconstructing sea level from paleo and projected temperatures 200 to 2100 ad, *Clim. Dyn., 34*(4), 461–472, doi:10.1007/s00382-008-0507-2.

Harney, J. N. and C. H. Fletcher, III (2003), A budget of carbonate framework and sediment production, Kailua Bay, Oahu Hawaii, *J. Sed. Res., 73*(6), 865–868. doi:10.1306/051503730856.

Hemer, M. A., Y. Fan, N. Mori, A. Semedo, and X. L. Wang (2013), Projected changes in wave climate from a multi-model ensemble, *Nat. Clim. Change, 3*(5), 471–476, doi:10.1038/NCLIMATE1791.

Hoeke, R. K. (2010), An investigation of wave-dominated coral reef hydrodynamics. PhD thesis, James Cook University.

Hoeke, R. K., K. L. McInnes, J. C. Kruger, R. J. McNaught, J. R. Hunter, and S. G. Smithers (2013), Widespread inundation of Pacific islands triggered by distant-source wind-waves, *Glob. Planet. Change, 108,* 128–138, doi:10.1016/j.gloplacha.2013.06.006.

Hoeke, R., McInnes, K., O'Grady, J., 2015. Wind and Wave Setup Contributions to Extreme Sea Levels at a Tropical High Island: A Stochastic Cyclone Simulation Study for Apia, *Samoa. J. Mar. Sci. Eng. 3*, 1117–1135. doi:10.3390/jmse3031117

Huang, Z.-C., L. Lenain, W. K. Melville, J. H. Middleton, B. Reineman, N. Statom, and R. M. McCabe (2012), Dissipation of wave energy and turbulence in a shallow coral reef lagoon, *J. Geophys. Res.-Oceans, 117,* C03015, doi:10.1029/2011JC007202.

Kench, P. S., and R. W. Brander (2006), Response of reef island shorelines to seasonal climate oscillations: South Maalhosmadulu atoll, Maldives, *J. Geophys. Res., 111*(F1), doi:10.1029/2005JF000323.

Kench, P. S., R. W. Brander, K. E. Parnell, and R. F. McLean (2006), Wave energy gradients across a Maldivian atoll: Implications for island geomorphology, *Geomorphology, 81*(1–2), 1–17, doi:10.1016/j.geomorph.2006.03.003.

Kench, P., Nichol, S., Smithers, S., McLean, R., and R. Brander (2008), Tsunami as agents of geomorphic change in mid-ocean reef islands, *Geomorphology, 95*(3–4), 364–383, doi:10.1016/j.geomorph.2007.06.012.

Kench, P. S., K. E. Parnell, and R. W. Brander (2009), Monsoonally influenced circulation around coral reef islands and seasonal dynamics of reef island shorelines, *Mar. Geol., 266*(1–4), 91–108, doi:10.1016/j.margeo.2009.07.013.

Kenyon, J. C., C. B. Wilkinson, G. S. Aeby, and others (2010), Community structure of hermatypic corals at Midway Atoll in the Northwestern Hawaiian Islands: A legacy of human disturbance, National Museum of Natural History, Smithsonian Institution.

Kenyon, J. C., V. Bonito, and C. B. Wilkinson (2013), Characterization of coral communities at Wake Atoll in the remote central Pacific Ocean, *Atoll Res. Bull., 30*(600).

Komar, P. D. (1971), The mechanics of sand transport on beaches, *J. Geophys. Res., 76*, 713– 721.

Lesser, G.R., Roelvink, J.A., van Kester, J.A.T.M., Stelling, G.S., 2004. Development and validation of a three-dimensional morphological model. *Coast. Eng. 51*, 883–915. doi:10.1016/j.coastaleng.2004.07.014

Lowe, R. J., J. L. Falter, S. G. Monismith, and M. J. Atkinson (2009), A numerical study of circulation in a coastal reef-lagoon system, *J. Geophys. Res.-Oceans, 114*, C06022, doi:10.1029/2008JC005081.

McLean, R. and P. Kench (2015), Destruction or persistence of coral atoll islands in the face of 20th and 21st century sea-level rise? *WIRES Climate Change*, *6*(5), 445–463, doi:10.1002/wcc.350.

Mimura, N. (1999), Vulnerability of island countries in the South Pacific to sea level rise and climate change, *Clim. Res., 12*(2–3), 137–143, doi:10.3354/cr012137.

Montaggioni, L. F. (2005), History of Indo-Pacific coral reef systems since the last glaciation: Development patterns and controlling factors, *Earth-Sci. Rev., 71*(1–2), 1–75, doi:10.1016/j.earscirev.2005.01.002.

Nicholls, R. J., and A. Cazenave (2010), Sea-level rise and its impact on coastal zones, *Science, 328*(5985), 1517–1520.

Ohde, S., M. Greaves, T. Masuzawa, H. A. Buckley, R. Van Woesik, P. A. Wilson, P. A. Pirazzoli, and H. Elderfield (2002), The chronology of Funafuti Atoll: revisiting an old friend, *Proc. R. Soc. Math. Phys. Eng. Sci., 458*(2025), 2289–2306, doi:10.1098/rspa.2002.0978.

Pelnard-Considere´, R. (1956), Essai de theorie de l’evolution des formes de rivage en plages de sable et de galets, in 4th Journees de l’Hydraulique, *Les Energies de la Mer, III*, pp. 289– 298, La Houille Blanche, Grenoble, France.

Pequignet, A. C., J. M. Becker, M. A. Merrifield, and S. J. Boc (2011), The dissipation of wind wave energy across a fringing reef at Ipan, Guam, *Coral Reefs, 30*, 71–82, doi:10.1007/s00338-011-0719-5.

Pomeroy, A., Lowe, R., Van Dongeren, A., Ghisalberti, M., Bodde, W., and D. Roelvink (2015), Spectral wave-driven sediment transport across a fringing reef, *Coast. Eng., 98*, 78–94, doi:10.1016/j.coastaleng.2015.01.005.

Purkis, S. J., R. Gardiner, M. W. Johnston, and C. R. C. Sheppard (2016), A half-century of coastline change in Diego Garcia - The largest atoll island in the Chagos, *Geomorphology, 261*, 282–298, doi:10.1016/j.geomorph.2016.03.010.

Quataert, E., C. Storlazzi, A. van Rooijen, O. Cheriton, and A. van Dongeren (2015), The influence of coral reefs and climate change on wave-driven flooding of tropical coastlines, *Geophys. Res. Lett., 42*(15), 6407–6415, doi:10.1002/2015GL064861.

Rankey, E. C. (2011), Nature and stability of atoll island shorelines: Gilbert Island chain, Kiribati, equatorial Pacific: Atoll shoreline change, equatorial Pacific, *Sedimentology, 58*(7), 1831–1859, doi:10.1111/j.1365-3091.2011.01241.x.

Reynolds, M. H., K. N. Courtot, P. Berkowitz, C. D. Storlazzi, J. Moore, and E. Flint (2015), Will the Effects of Sea-Level Rise Create Ecological Traps for Pacific Island Seabirds?, edited by P. Quillfeldt, *PLOS ONE, 10*(9), e0136773, doi:10.1371/journal.pone.0136773.

Ris, R. C., L. H. Holthuijsen, and N. Booij (1999), A third-generation wave model for coastal regions - 2. Verification, *J. Geophys. Res.-Oceans, 104*(C4), 7667–7681, doi:10.1029/1998JC900123.

Rogers, J. S., S. G. Monismith, D. A. Koweek, and R. B. Dunbar (2016), Wave dynamics of a Pacific Atoll with high frictional effects: WAVE DYNAMICS WITH HIGH FRICTION, *J. Geophys. Res. Oceans, 121*(1), 350–367, doi:10.1002/2015JC011170.

Rosati, J. D., T. L. Walton, and K. Bodge (2002), Longshore sediment transport, in Coastal Engineering Manual, part II, Coastal Sediment Processes, edited by D. B. King, chap. III-2, U.S. Army Corps of Eng., Washington, D. C.

Roy, P., and J. Connell (1991), Climatic-Change and the Future of Atoll States, *J. Coast. Res., 7*(4), 1057–1075.

Semedo, A., R. Weisse, A. Behrens, A. Sterl, L. Bengtsson, and H. Guenther (2013), Projection of Global Wave Climate Change toward the End of the Twenty-First Century, *J. Clim., 26*(21), 8269–8288, doi:10.1175/JCLI-D-12-00658.1.

Sheppard, C., D. J. Dixon, M. Gourlay, A. Sheppard, and R. Payet (2005), Coral mortality increases wave energy reaching shores protected by reef flats: Examples from the Seychelles, *Estuar. Coast. Shelf Sci., 64*(2–3), 223–234, doi:10.1016/j.ecss.2005.02.016.

Shope, J. B., C. D. Storlazzi, L. H. Erikson, and C. A. Hegermiller (2016), Changes to extreme wave climates of islands within the Western Tropical Pacific throughout the 21st century under RCP 4.5 and RCP 8.5, with implications for island vulnerability and sustainability, *Glob. Planet. Change, 141*, 25–38, doi:10.1016/j.gloplacha.2016.03.009.

Smith, E. R., P. Wang, B. A. Ebersole, and J. Zhang (2009), Dependence of Total Longshore Sediment Transport Rates on Incident Wave Parameters and Breaker Type, *J. Coast. Res., 25*(3), 675–683, doi:10.2112/07-0919.1.

Smithers, S. G., and R. K. Hoeke (2014), Geomorphological impacts of high-latitude storm waves on low-latitude reef islands — Observations of the December 2008 event on Nukutoa, Takuu, Papua New Guinea, *Geomorphology, 222,* 106–121, doi:10.1016/j.geomorph.2014.03.042.

Storlazzi, C. D., E. Elias, M. E. Field, and M. K. Presto (2011), Numerical modeling of the impact of sea-level rise on fringing coral reef hydrodynamics and sediment transport, *Coral Reefs*, *30*, 83–96, doi:10.1007/s00338-011-0723-9.

Storlazzi, C. D., and J. A. Reid (2010), The influence of El Nino-Southern Oscillation (ENSO) cycles on wave-driven sea-floor sediment mobility along the central California continental margin, *Continental Shelf Research, 30*(14), 1582–1599. doi:10.1016/j.csr.2010.06.004.

Storlazzi, C. D., E. P. L. Elias, and P. Berkowitz (2015), Many Atolls May be Uninhabitable Within Decades Due to Climate Change, *Sci. Rep.*, *5*, 14546, doi:10.1038/srep14546.

Taebi, S., and C. Pattiaratchi (2014), Hydrodynamic response of a fringing coral reef to a rise in mean sea level, *Ocean Dyn., 64*(7), 975–987, doi:10.1007/s10236-014-0734-5.

Terry, J. P., and A. C. Falkland (2010), Responses of atoll freshwater lenses to storm-surge overwash in the Northern Cook Islands, *Hydrogeol. J.*, *18*(3), 749–759, doi:10.1007/s10040-009-0544-x.

Vermeer, M., and S. Rahmstorf (2009), Global sea level linked to global temperature, *Proc. Natl. Acad. Sci., 106*(51), 21527–21532.

Vousdoukas, M. I., Velegrakis, A. F., and T. A. Plomaritis (2009), Beachrock occurrence, characteristics, formation mechanisms and impacts, *Earth-Science Reviews*, *85*(1–2), 23–46. doi: 10.1016/j.earscirev.2007.07.002.

Wang, X. L., Y. Feng, and V. R. Swail (2014), Changes in global ocean wave heights as projected using multimodel CMIP5 simulations, *Geophys. Res. Lett.*, *41*(3), 1026–1034, doi:10.1002/2013GL058650.

Webb, A. P., and P. S. Kench (2010), The dynamic response of reef islands to sea-level rise: Evidence from multi-decadal analysis of island change in the Central Pacific, *Glob. Planet. Change*, *72*(3), 234–246, doi:10.1016/j.gloplacha.2010.05.003.

Woodroffe, C., McLean, R., Smithers, S., and E. Lawson (1999), Atoll reef-island formation and response to sea-level change: West Island, Cocos (Keeling) Islands, *Marine Geology*, *160*(1–2), 85–104, doi:10.1016/S0025-3227(99)00009-2.

Woodroffe, C. D. (2008), Reef-island topography and the vulnerability of atolls to sea-level rise, *Glob. Planet. Change*, *62*(1–2), 77–96, doi:10.1016/j.gloplacha.2007.11.001.

Yamano, H., H. Kayanne, T. Yamaguchi, Y. Kuwahara, H. Yokoki, H. Shimazaki, and M. Chikamori (2007), Atoll island vulnerability to flooding and inundation revealed by historical reconstruction: Fongafale Islet, Funafuti Atoll, Tuvalu, *Glob. Planet. Change*, *57*(3–4), 407–416, doi:10.1016/j.gloplacha.2007.02.007.

Yates, M. L., G. Le Cozannet, M. Garcin, E. Salaï, and P. Walker (2013), Multidecadal Atoll Shoreline Change on Manihi and Manuae, French Polynesia, *J. Coast. Res.*, *289*, 870–882, doi:10.2112/JCOASTRES-D-12-00129.1.

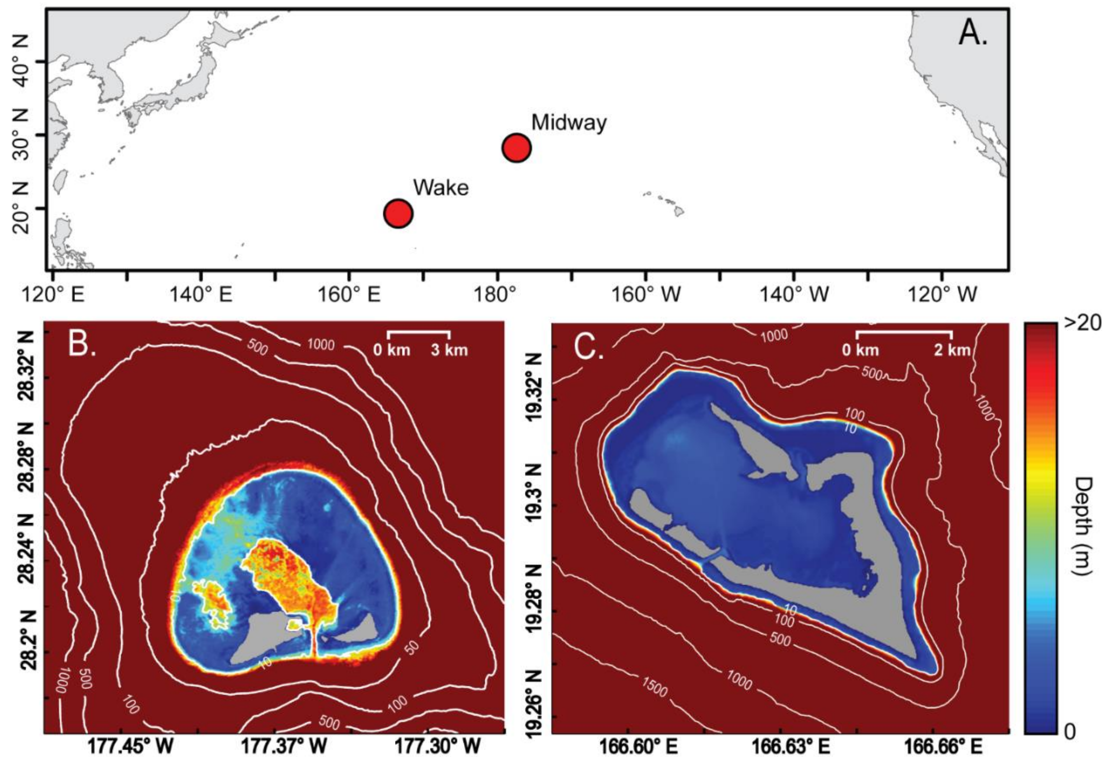

Figure 2-1. Locations (A) and morphologies of the atolls being investigated. Bathymetry and island shape of (B) Midway Atoll and (C) Wake Atoll. Depth values are in meters.

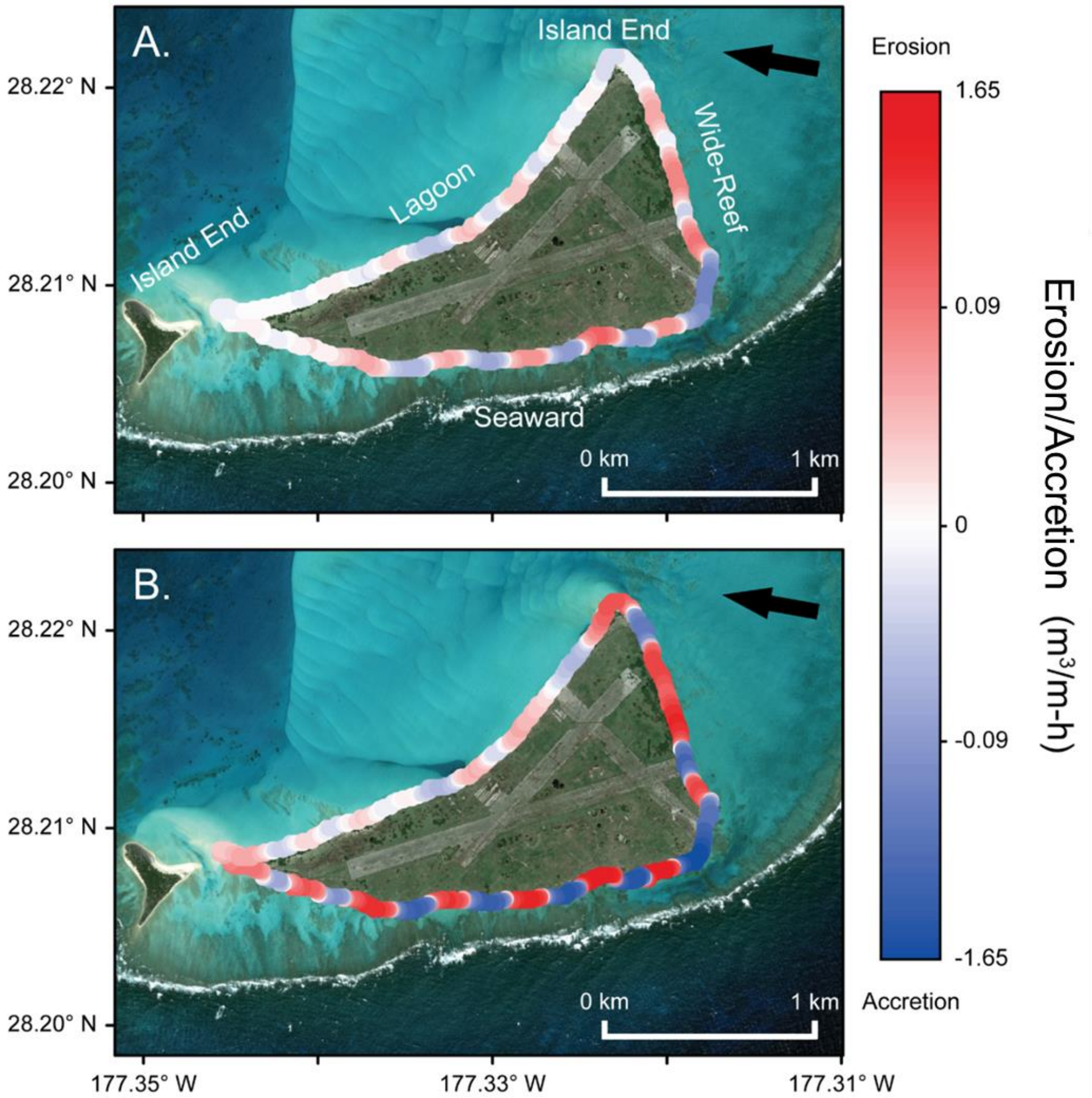

Figure 2-2. Example of model erosion/accretion output for East Island under initial summer conditions (A) with shoreline divisions and +2.0 m SLR (B). Incident waves approach the atoll from 110° indicated by the black arrow at 3.6 m. Erosion values are in cubic meters per meter hour. Note the geometrically increasing color scale. Imagery Source: “Midway Islands, NWHI,” DigitalGlobe (2010).

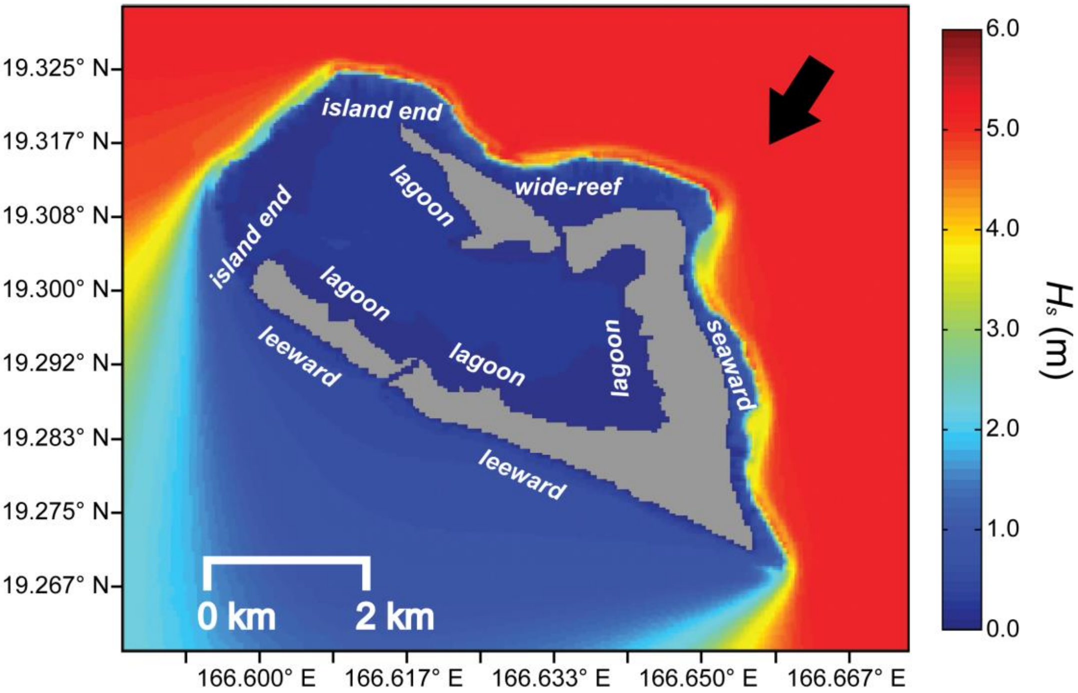

Figure 2-3. Example of model H_s output for Wake atoll under initial winter conditions with shoreline divisions in relation to incident wave energy labeled. Incident waves approach the atoll from 33° indicated by the black arrow at 5.1 m. Wave height values are in meters.

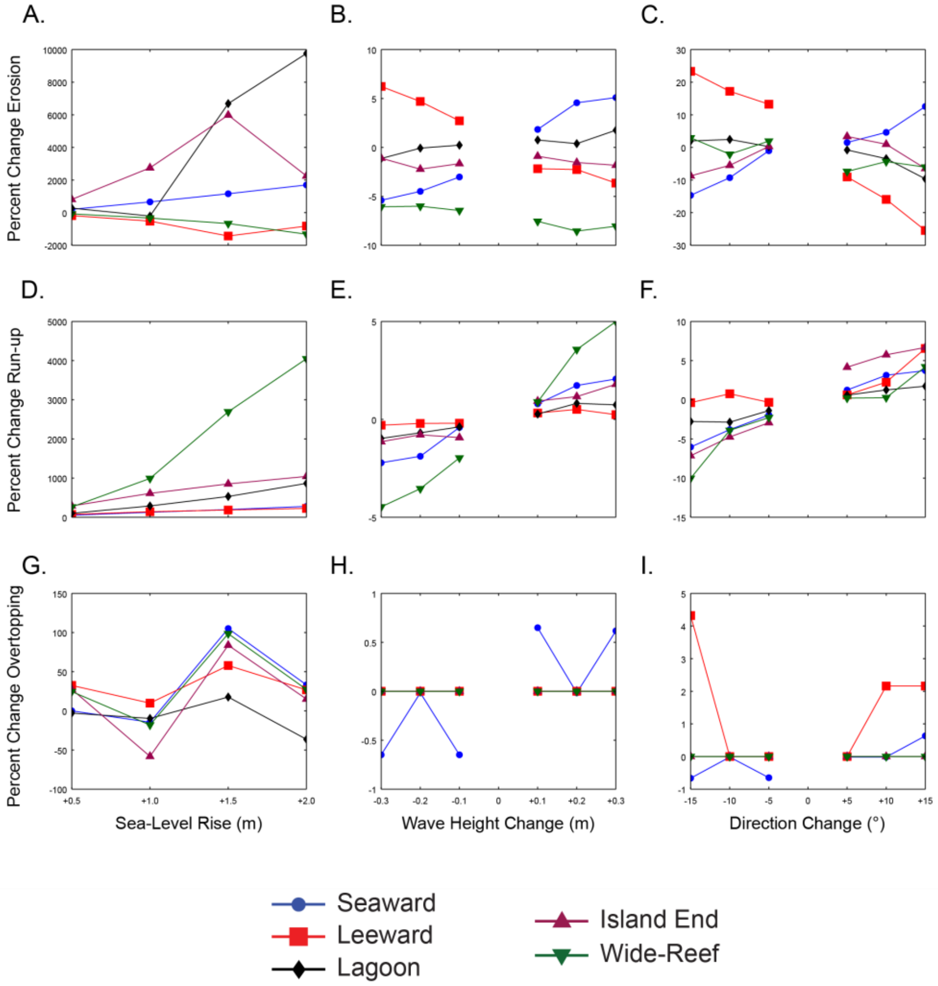

Figure 2-4. Response of Wake Atoll to changes in forcing conditions. Percent change values for accretion/erosion (A–C) where increased erosion corresponds to positive values, run-up (D–F), and overtopping ratios (G–I) in response to sea-level rise (A, D, G), changing H_s at model boundaries (B, E, H), and incident wave directions (C, F, I) for each shoreline type.

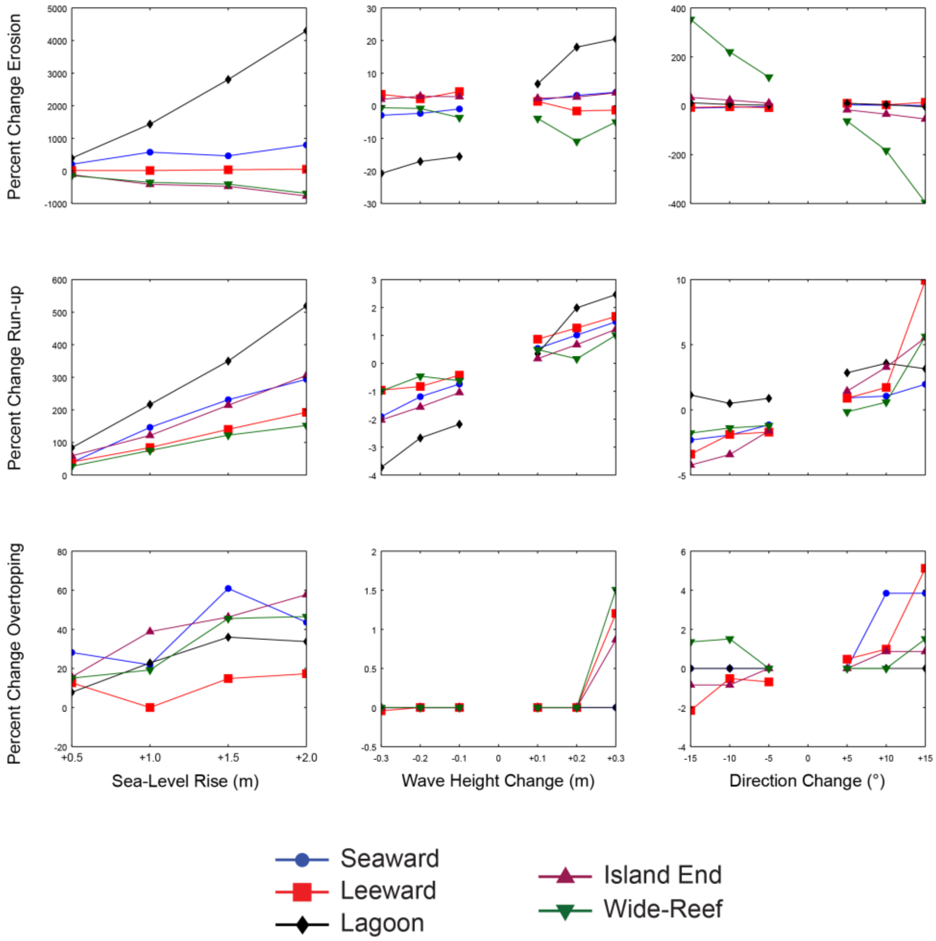

Figure 2-5. Response of Midway Atoll to changes in forcing conditions. Percent change values for accretion/erosion (A–C) where increased erosion corresponds to positive values, run-up, run-up (D–F), and overtopping ratios (G–I) in response to sea-level rise (A,D,G), changing H_s at model boundaries (B,E,H), and incident wave directions (C,F,I) for each shoreline type.

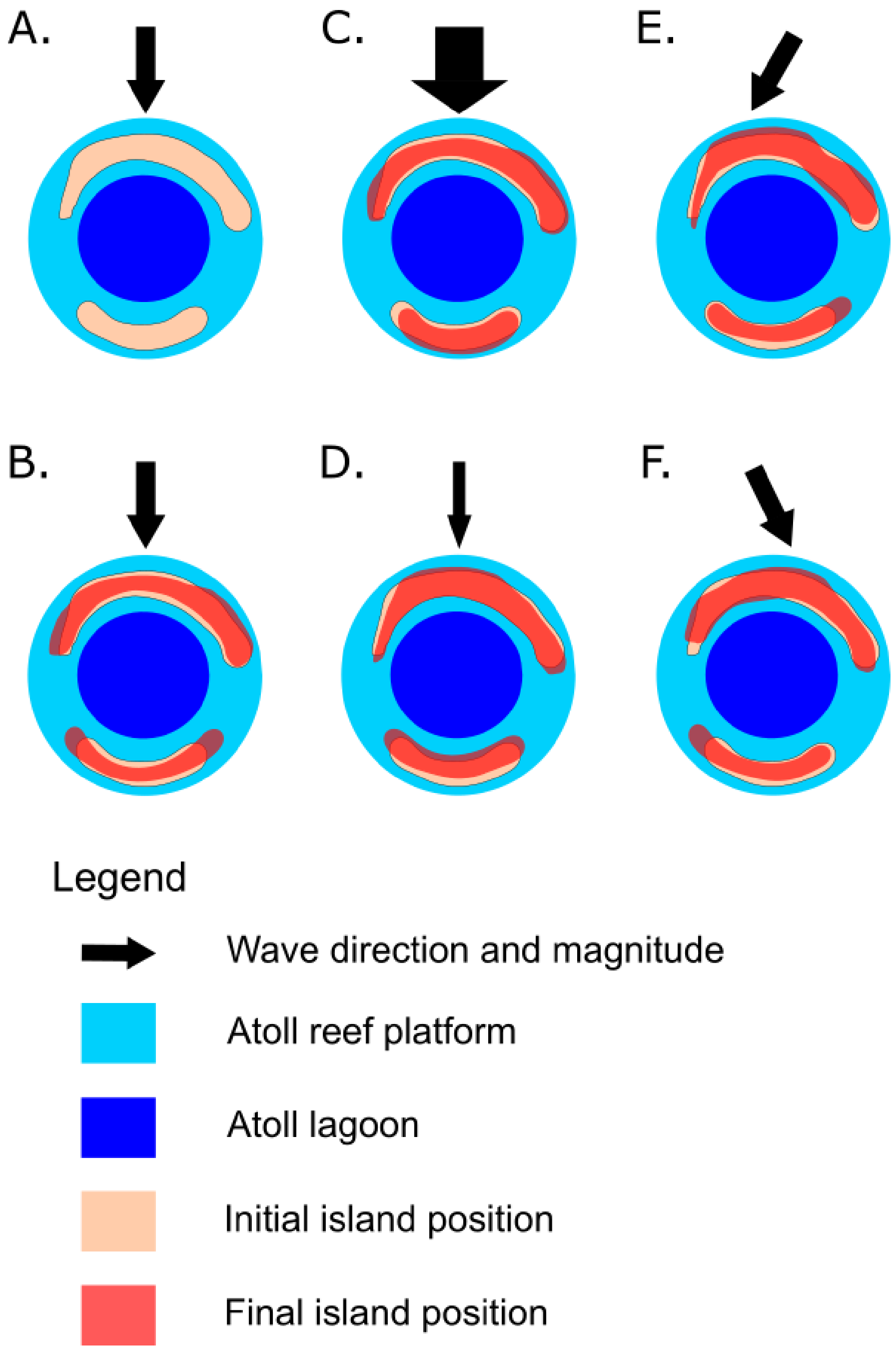

Figure 2-6. Schematic diagram of how atoll islands are projected to respond to changes in forcing conditions. (A) Generic atoll islands with waves approaching from the north may respond to (B) increased sea level, (C) an increase in offshore H_s by 0.3 m, (D) a decrease in offshore H_s by 0.3 m, (E) a clockwise rotation in incident wave direction, and (F) a counter clockwise rotation of incident wave direction.

Table 2-1. Summary of model boundary forcing parameters for Wake and Midway

Atoll	Season	Significant Wave Height (m)	Wave Direction (°)
Wake	DJF	5.1	33
	JJA	3.9	109
Midway	DJF	7.8	302
	JJA	3.6	110

Chapter Three

ASSESSING MORPHOLOGICAL CONTROLS ON ATOLL ISLAND SHORELINE STABILITY DUE TO FUTURE SEA-LEVEL RISE

Abstract

Atoll islands' shoreline stability depends on how island and reef morphology affects incident wave energy; sea-level rise (SLR) may lead to decreased shoreline stability. It is unclear how specific atoll morphologic parameters influence shoreline erosion and/or accretion patterns, and how these relationships respond to SLR. Schematic atoll models with varying morphologies were used to evaluate the impact of individual parameters on erosion and/or accretion. A generic atoll bathymetry was developed and incident wave transformations were simulated using a physics-based numerical model. Alongshore sediment transport was calculated from the numerical wave model output and empirical formula; the resulting wave-driven erosion or accretion was calculated as the divergence of alongshore transport. The magnitude of erosion or accretion increased with sea level; shorelines that were initially erosive generally became more erosive, and shorelines that were initially accretive generally become more accretive due to SLR. The morphologic parameters that significantly influenced shoreline stability were reef flat width, reef flat depth, island width, and atoll diameter. Narrower reef flats, deeper reef flats, narrower islands, and smaller atoll diameters were associated with increased magnitude of erosion and/or accretion. Variations in lagoon beach slope, seaward beach slope, fore reef slope, and island length did not significantly influence erosion and accretion patterns. Windward islands are projected to extend toward their longitudinal ends and migrate toward the lagoon due to SLR, whereas leeward islands erode along lagoon shorelines and extend toward their longitudinal ends. Oblique islands oriented parallel to the incident

deepwater wave direction are forecast to migrate leeward along the reef rim and toward the lagoon. These results suggest that small islands on small atolls are most at risk most at risk for decreased coastline stability with SLR. These findings make it possible to evaluate the relative risk of coastal change hazards to atolls islands due to SLR and help prioritize mitigation efforts.

3.1 Introduction

Atolls are shallow, ring-shaped, coral platforms upon which small, low-elevation carbonate islands are often perched (Figure 3-1). Communities living on atoll islands are vulnerable to large wave events and changing climates (Storlazzi et al., 2015). As global climate warms, sea levels are projected to increase by as much as 2.0 m by 2100 due to seawater thermal expansion and glacial/ice cap melt (Vermeer and Rhamstorf, 2009; Grinstead et al. 2009; Nicholls and Cazenave, 2010); the rate of SLR is projected to exceed the rate of coral reef platform vertical accretion (Montaggioni, 2005). Global sea-level rise (SLR) and reef degradation (bleaching, ocean acidification, etc.) will affect wave conditions along the shoreline by reducing the reef platform's ability to attenuate wave energy and protect island shorelines (Sheppard et al., 2005; Storlazzi et al., 2011; Grady et al., 2013; Ferrario et al., 2014; Shope et al., *in review*). Incident wave dynamics and atoll morphology control shoreline erosional and accretional patterns, and thus some islands may be more vulnerable to future erosion hazards than others. . To help atoll island communities prepare for the future, it is imperative to identify the morphologic factors that control wave energy and the resulting erosional and/or depositional patterns at the atoll scale, and thus which islands are most susceptible to shoreline instability due to morphologic change.

Many studies have explored atoll island response to SLR (Roy and Connell, 1991; Woodroffe, 2008; Webb and Kench, 2010; Rankey, 2011; Ford, 2012; Yates et al., 2013; Purkis et al., 2016), extreme wave events (Hoeke et al. 2013, Smithers and Hoeke, 2014), and reef controls on shoreline sediment mobilization and erosion (Sheppard et al. 2005; Storlazzi et al., 2011; Grady et al., 2013). Although these approaches have elucidated large-scale trends, most of the analyses are location specific, involving a few atoll islands, and/or have only considered the effects of historic SLR. Most atoll islands formed during the mid-Holocene sea level highstand (Kench et al., 2009) and current sea levels have yet to attain those previous highstand levels when islands dynamically formed (Dickinson, 2004; 2009). Thus historical studies (e.g., Webb and Kench, 2010) from relatively low recent sea levels might not accurately portray how islands will respond in the future when sea levels are predicted to attain, if not exceed (Vermeer and Rhamstorf, 2009; Grinstead et al. 2009; Nicholls and Cazenave, 2010), those sea levels when islands formed (Dickinson, 2009). An atoll island’s erosional and accretional patterns may be different from another’s due to varying reef flat width, reef depth, island shape, and direction of incident waves. There has been limited exploration modeling of the erosional and accretional effect of changing wave conditions along atoll islands

(Shope et al. *in review*); it is currently unclear how erosion along different atoll island shorelines will respond to future wave attack and SLR under the influence of different morphologies.

To address morphologic controls on wave-driven erosion and accretion, Grady et al. (2013) and Quataert et al. (2015) modeled the effects of varying reef dimensions on wave parameters along reef-protected shorelines using a schematic or generalized bathymetry. Both of those studies, however, were one-dimensional (cross-shore) models. To capture alongshore variability, this approach requires multiple cross-shore transects. Additionally, lagoon-facing shorelines are generally less well-studied than ocean-facing shorelines. There has not been a two-dimensional modeled analysis of wave-driven erosion along a generalized atoll island shoreline. A two-dimensional model allows a greater number of morphological parameters to be varied to observe the impact on erosion or accretion along individual island shorelines.

Here, we use a physics-based two-dimensional numerical wave model with varying schematized topography/bathymetry and empirical relationships to explore potential morphological controls on wave-driven atoll island erosional and accretional patterns due to SLR. A schematic model allows morphological parameters to be isolated and systematically varied to discern their relative controls on atoll island shoreline stability. For example, a single morphological parameter, such as reef flat depth, can be altered while keeping all other parameters constant, a condition that cannot be replicated from observational data of real atolls. We present a brief overview of atoll and island morphology, characteristic ranges of morphologic parameters, and information about oceanographic forcing and wave transformation over atoll reefs. The model set-up and run conditions are then discussed, including formulation and descriptions of implementation, and then erosion/accretion calculations and data analyses. Finally, the results of changes in shoreline erosion with varying morphology and SLR are presented, followed by a discussion of these trends in relation to previous studies.

3.2 Atoll morphology and interaction with waves

Atolls are shallow raised carbonate platforms with a central lagoon that generally top seamounts or subsided volcanoes. This carbonate platform is created by successive vertical accretion of coral reefs as relative sea level increases, either by eustatic SLR or by subsidence of the underlying volcanic edifice (Dickinson, 2004). The platform steeply rises from depths of a few kilometers to a shallow (0.5–2 m water depth) annular reef flat around the central lagoon. Atoll reefs, and fringing reefs in general, have steep fore reef slopes (Figure 3-2, Table 3-1, Quataert et al., 2015), whereas the slope from the reef flat into the lagoon is usually gentle (≤1/20). Atoll diameters, measured along the longest axis, vary widely (Table 3-1). For example, Majuro Atoll has a diameter of approximately 40 km (Figure 3-1A), whereas Wake Atoll has a diameter of approximately 7 km (Figure 3-1C).

Waves and currents rework reef-derived sediment into islands that sit atop the reef flat (Ohde et al., 2002). Larger atoll islands are underpinned by relict Pleistocene reef material that keeps the sediment in place (Dickinson, 2004) and often enables consolidation into beach rock that inhibits shoreline sediment transport (Vousdoukas et al., 2007). Smaller atoll islands are generally composed of unconsolidated sediment continually reworked by waves. Atoll islands are generally small, with widths generally less than 1 km (Table 3-1), and low in elevation, on average 2–3 m above sea level (Woodroffe, 2008). Island lengths vary greatly, from a 100s of m to several km. For example, Majuro Island is narrow (width~250–550 m) with a narrow fringing reef flat of 150–200 m (Figure 3-1B), whereas Wake Island is wider (~600–800 m), with reef flats ranging from approximately 50 m along its southern shoreline to 600 m along its northern shoreline (Figure 3-1C).

The shallow reef crest causes incident waves to dissipate most of their energy through depth-limited breaking (Ferrario et al. 2014). Wave energy that traverses the reef flat is further dissipated by frictional interactions with the rough reef flat (Lowe et al., 2005; Storlazzi et al., 2011; Quataert et al., 2015). The width of the reef flat seaward of an atoll island helps control wave energy attenuation, with wider reef flats providing greater energy dissipation (Grady et al., 2013; Ferrario et al. 2014; Quataert et al., 2015). With SLR or reef degradation, reef flats become deeper, reducing wave interaction with the underlying reef and thus increasing wave energy delivered to shorelines (Gourlay, 1996; Pequignet et al., 2011; Taebi and Pattiaratchi. 2014; Hoeke et al., 2015).

Atoll islands are dynamic features whose shorelines can respond to changing wave conditions on seasonal (Kench and Brander, 2006) and decadal (Rankey, 2011) timescales. As a result, with SLR, atoll islands may not necessarily be inundated and lose area. Webb and Kench (2010) and Yates et al. (2010) found that some Pacific atoll islands increased in total area over the 20th century despite SLR; however, as discussed before, this trend may not persist as SLR attains those during the mid-Holocene highstand that resulting in dynamic island formation and SLR rates are projected to accelerate by 2100 (Vermeer and Rhamstorf, 2009; Grinstead et al., 2009; Nicholls and Cazenave, 2010). Studies have found that deeper reef flats are associated with higher rates of coastal sediment transport (Storlazzi et al., 2011; Grady et al., 2013).

Atolls are subject to a variety of wave conditions, ranging from small locally-generated wind waves to large swell waves generated far afield by storms and trade winds (Hoeke et al. 2013; Shope et al. 2016). Historical simulations indicate that the mean of the largest 5% of deep water waves at many tropical Pacific atolls ranges from 4 to 8 m during the Northern Hemisphere winter and 2 to 4 m during its summer (Shope et al., 2016).

3.3 Methods

3.3.1 Numerical model

Incident wave simulations were modeled using Deltares's Delft3D modeling suite. Within this study, the WAVE module, which runs the spectral Simulating Waves Nearshore (SWAN) model, was used to simulate wave transformations over the model bathymetry (Booij et al., 1999; Ris et al., 1999). Most of the default model settings were used, but the bottom friction of the reef was formulated using the Madsen coefficient of 0.1 m following Hoeke (2010), and wave set up was enabled. It should also be noted that SWAN does not simulate infragravity waves. Infragravity waves have been shown to play an important role in terms of hydrodynamics along atoll islands, driving greater flooding (Quataert et al., 2015; Cheriton et al., 2016) and overwash, especially along shorelines with narrow fringing reef flats (Ford et al, 2013). However, infragravity waves would likely have a minimal impact on alongshore sediment transport because of their low bottom shear stresses (van Dongeren et al., 2013; Pomeroy et al., 2015). Infragravity waves are generally modeled in one dimension to expedite calculation, but this approach would require many transects to characterize the alongshore variability in wave processes. As the purpose of this study is to efficiently model island shoreline response to incident wave forcing under different morphologies in two dimensions, it was necessary to neglect the role of infragravity waves within the analysis.

3.3.2 Model schematization and bathymetry

The dimensions of many atolls and atoll islands were analyzed to determine characteristic dimensions of a “typical” atoll to create a schematized topography/bathymetry. A wide range of atoll and island dimensions were recorded from many peer-reviewed studies and satellite imagery (Table 3-1). Based on this data compilation, a generalized atoll was created using characteristic values within the described range for each dimension. The final schematized topography/bathymetry was a circular atoll ring with four islands situated at 0°, 90°, 180°, and 270° from north along the rim (Figure 3-3A). The maximum water depth outside of the atoll was set to be 100 m, as the waves forced over the bathymetry would not interact with the bottom at this depth, representing deep water wave conditions. The depth of the lagoon was set to be 15 m, as it is assumed that there is negligible interaction between the low amplitude, high-frequency waves in the lagoon and the lagoon bottom. Lagoon depths can vary considerably between atolls, and do not likely have a huge impact on wave driven impacts along island shorelines because in situ wind-wave growth is a function of fetch, which is relatively limited in the lagoons. Another parameter that was held constant across all model runs was the maximum elevation of the islands, set to be 7 m. Atoll island storm ridges are generally on the order of 4 m above sea level (Woodroffe, 2008), representing the highest point on the island. However, when smoothing the topography/bathymetry used in the model, a higher elevation was necessary to maintain the island shape above sea level at coarse resolutions. Beaches were created by scaling the edges of the islands using the beach slopes found in Table 3-1, and subsequent smoothing of the topography/bathymetry. The islands were elongate, with rounded ends, and were a consistent distance from the reef rim and the lagoon rim (Figure 3-3B).

The remaining atoll morphology parameters were variable. An “initial control” configuration was selected based on the most characteristic values within the ranges summarized in Table 3-1. Data in Table 3-1 do not represent all atolls, but represent a wide range of existing atoll morphologies. The initial fringing reef flat depth was 1 m and its width was 250 m, the fore reef slope was 1/10, the lagoon reef slope was 1/20, the island length was 2 km, the island width was 0.5 km, the lagoon beach slopes were 1/15, and the ocean-facing beach slopes were 1:6. The beach slopes at the island ends were assumed to change linearly between the ocean facing and lagoon beach slopes. The size of an atoll can vary widely, but most are on the scale of 10–50 km, and therefore an initial atoll size of 20 km was selected. Schematized atoll bathymetries were generated incorporating different morphologic parameters (Table 3-1). The initial control schematization was a base from which individual parameters were varied within a given range (Table 3-1) while keeping the others constant. For example, under initial conditions, the reef flat was at a depth of 1.00 m. Between model runs, this depth was varied from 0.25 m to 2.00 m at 0.25 m increments. The rapid changes in atoll bathymetry necessitate that each bathymetry be smoothed according to the most extreme morphological parameters so that the SWAN simulation converged. The smoothed bathymetries maintained the same general structure of the pre-smoothed bathymetries. Smoothing should not impact final results, as each bathymetry was smoothed to the same degree and the results between runs were compared relative to one another.

3.3.3 Model setup

For atoll diameters of 5–20 km, the model was composed of two grids, a 60-m coarse resolution grid representing the entire atoll and a 20-m fine resolution grid focused on the northern island of the atoll. For larger atolls, these grids were further nested in a 180-m grid for 40 km diameter, and in a 320-m grid for 60 km and 80 km diameters. The boundary deep-water wave conditions of the model were a significant wave height (H_s) of 3 m with a peak wave period (T_p) of 15 s to represent large swell conditions (Figure 3-4). The direction of the waves (θ_w) was 0°, 90°, or 180° from north to simulate the higher resolution northern island grid in the windward, leeward, and oblique position relative to incident wave energy.

3.3.4 Alongshore sediment transport and erosion/accretion modeling

The instantaneous alongshore sediment flux was calculated via the Coastal Research Engineering Center (CERC) equation as formulated by Komar (1971) and Rosati (2002), which has been used in previous shoreline change studies (e.g., Ashton and Murray, 2006 and Adams et al., 2011). The formula was adapted for use along atoll island shorelines using the methodology described by Shope et al. (*in review*). The CERC formula is given as:

$$Q_l = \frac{I_l}{(p_s - p_w)gN_O} \tag{1a}$$

$$I_l = K\frac{1}{8}p_w g H_b^2 Cn\sin(\alpha)\cos(\alpha) \tag{1b}$$

$$C = \frac{gT}{2\pi}\tanh\left(\frac{2\pi h}{L_o}\right) \tag{1c}$$

where Q_l is the alongshore sediment transport rate (m^3/s), p_s is the density of carbonate sand (here the bulk density of coral, 1400 kg/m^3, was used [Grigg, 1982; Harney and Fletcher, 2003]), p_w is the density of seawater (1024 kg/m^3), N_O is the volumetric concentration of solid grains (~0.6), I_l is the immersed weight transport rate, H_b is the breaking wave height, C is nearshore wave celerity (m/s, a function of H_s, T_p and h [e.g., Komar, 1998]), n is the shallow water assumption for wave group velocity (0.5), α is the angle of incidence between θ_w and shoreline direction, h is water depth (m), g is the acceleration due to gravity (~9.81 m/s^2), and L_o is wave length (m, a function of T_p and h [e.g., Komar, 1998]). The tuning parameter (K) in equation 1b was varied at each cell following Smith et al. (2009) to generate a better approximation of transport magnitudes. K was calculated as:

$$K = 0.7\xi_b = 0.7\frac{m}{\sqrt{\frac{H_b}{L_o}}} \tag{2}$$

where m is the beach slope.

The primary differences between the traditional CERC application and the methodology used in this study are the distances from shore that the breaking wave characteristics used in the formula were applied and smoothing of the input and output. When calculating sediment transport with CERC, H_b and θ_w are usually computed at a water depth of approximately 5 m (Adams et al. 2011). Along atoll reefs, there are two zones of breaking: the first is at the reef crest, where the larger waves break due to the rapidly shoaling bathymetry, and the second is at the island shoreline. Additionally, the rapid shoaling of the bathymetry causes the incident wave to heavily refract and intersect the shoreline nearly perpendicularly, such that conditions at the reef crest breaking point do not represent the nearshore conditions that drive alongshore sediment transport and morphological change. Therefore, H_s and θ_w output by SWAN along the shoreline were used as input to the CERC calculations instead of H_b and θ_w at a water depth of approximately 5 m. Input and output variables were low-pass filtered to reduce the higher frequency alongshore noise, as were the calculated alongshore wave-driven sediment transport rates. The CERC formula has primarily been utilized for was originally created for long, linear, siliciclastic coastlines (e.g. Adams et al., 2011). Along more complex atoll island morphology, it was necessary to remove highly local patterns to discern shoreline-scale trends. The low-pass filter was set to remove any variations smaller than 20% of the initial island alongshore circumference. This threshold was determined to give the general alongshore drift patterns of the island as a whole, while removing most sub-shoreline scale variation. As these model runs were for an idealized atoll under idealized conditions, smoothing the input and output parameters created a clearer picture of general shoreline changes and the controls of morphology on the magnitude of alongshore sediment transport.

3.3.5 Limitations and assumptions

It is important to note that the CERC formula does have some limitations. Primarily, it only calculates sediment transport in the alongshore direction, so cross-shore sediment processes were ignored within this study. Although this assumption does discount the effects of the over wash of sediment onto the island and the transport of sediment into the lagoon (Woodroffe et al., 1999; Kench et al., 2008; Smithers and Hoeke, 2014; McLean and Kench, 2015), Kench and Brander (2006) and Kench et al., (2009) noted that sediment transport along atoll islands tends to be dominated by alongshore processes. However, with SLR, overwash will likely increase (e.g., Quataert et al., 2015; Cheriton et al., 2016), and increasing onshore sediment transport will alter the alongshore sediment transport patterns as well. Also, CERC assumes that there is an unlimited amount of sediment to transport. Although a valid assumption along many siliciclastic coastlines, atoll environments generally have a comparably limited supply of sediment, leading to an over-estimation of transport magnitudes.

It was assumed that island shorelines were composed of unconsolidated sand. Island shorelines can also include weakly lithified carbonate sands and shingle that inhibit wave-driven sediment transport (Vousdoukas et al., 2007). Therefore, the calculated magnitudes of sediment transport are likely exaggerated and projected trends of shoreline change may not necessarily be mimicked in a real-world setting. Additionally, this method of calculating alongshore erosion/accretion is instantaneous and does not incorporate other processes such as waves from other directions and morphological dynamics present in an evolving coastline that help determine future steady-state shoreline shape and change. For the purposes of analysis, it was assumed that the calculated trends were maintained over long time periods and was the dominant process governing island change. Although Delft3D includes a sediment transport and morphology module (MOR), it was not used because one must then have a good understanding of island sedimentology and stratigraphy, which has been shown to be quite heterogeneous (e.g., Kench et al., 2005; Rankey, 2011). Lastly, instantaneous calculations of erosional and accretional patterns were faster and, therefore, a much greater number of morphological scenarios could be investigated than had Delft3D-MOR been used with an estimate of island sedimentology and stratigraphy.

3.3.6 Coastal change analysis

Erosion and accretion were calculated as the divergence of the calculated alongshore drift: $\partial Q_l / \partial \mathrm{x}$, where x is the distance alongshore (e.g., Pelnard-Considere, 1956). Here, positive divergence of drift values were defined as erosion and negative values as accretion. These magnitudes of erosion or accretion were then divided by the local grid resolution (20 m) to represent the erosion or accretion magnitude per m of shoreline. For each island, the erosion or accretion values were divided into one of three shoreline types: seaward, lagoon, and island ends. Seaward shorelines face the ocean, lagoon shorelines face towards the central lagoon, and the island ends are the longitudinal ends of the islands. For oblique islands, a windward island end faces the direction of incident wave energy and a leeward island end faces away from the direction of incident wave energy.

For each scenario, the erosion or accretion values for each shoreline were summed to discern net shoreline erosion/accretion. These were then compared relative to the net erosion/accretion for the same shoreline for simulations of different forcing and/or morphologies. It must be stressed that due to the accuracy of the CERC formulation and the fact that this is an idealized model, the absolute output magnitudes were not reported or considered in the analyses. Instead, the results were compared in a relative sense, without quantifying the magnitude of difference between simulations.

3.4 Results

This study seeks to compare the impact of SLR on the relative magnitude of erosion and accretion values along island shorelines under different morphologies. The influence of varying island width, reef flat width, reef flat depth, and atoll diameter are described here. Variations in lagoon beach slope, ocean-facing beach slope, fore-reef slope, and island length are not presented, as erosion and accretion were found to be relatively insensitive to changes in these parameters. For windward and leeward islands, results for both island ends were similar. Therefore, results of one representative island end shoreline are presented. For oblique islands, the seaward and leeward island end shorelines behaved differently, and results are presented for each individual shoreline. The magnitude of erosion/accretion increased with increasing sea level; shorelines that were initially erosive with lower sea level generally became more erosive with SLR, and shorelines that were initially accretive with lower sea level generally became more accretive with SLR.

3.4.1 Windward island

Seaward shorelines were erosive under all morphology ranges. Smaller island widths (Figure 3-5A1), narrower reef flats (Figure 3-5B1), deeper reef flats (Figure 3-5C1) and smaller atoll diameters (Figure 3-5D1) produced greater erosion. Narrow reef flats (<150 m) were associated with intense erosion, even at low values of SLR. Although small atoll diameters (5–10 km) were associated with the most erosion, medium-sized atolls (20–40 km) generally had lower erosion than large atolls (60–80 km). The greatest magnitude of erosion with SLR occurred with deep (>1.5 m) and narrow reef flats.

Lagoon shorelines were accretive under all morphology ranges. Smaller island widths (Figure 3-5A2), narrower reef flats (Figure 3-5B2), deeper reef flats (Figure 3-5C2), and smaller atoll diameters (Figure 3-5D2) caused more accretion. Narrow reef flats were associated with substantial accretion, even at low sea levels. Although small atoll diameters were associated with the most accretion, medium-sized atolls generally had lower accretion than large atolls. The greatest magnitude of accretion with SLR occurred with deep reef flats and narrow island widths (< 300 m).

Island end shorelines were accretive all morphology ranges; however, the magnitudes were the smallest for all islands and shorelines in this study (Figure 3-5A3–4D3). Narrow reef flats were associated with more accretion (Figure 3-5B3). Otherwise, the changes with morphological parameters were negligible.

3.4.2 Leeward island

Seaward shorelines were slightly erosive at 0 m SLR and became more accretive with SLR. The magnitudes overall were generally small (Figure 3-6A1–5D1). Small island widths, deeper reef flats, and narrow reef flats were associated with more accretion. The increase in accretion was greatest for small island widths.

Lagoon shorelines were erosive under almost all morphologies. Smaller island widths (Figure 3-6A2), narrower reef flats (Figure 3-6B2), and deeper reef flats (Figure 3-6C2) generated more erosion. The greatest magnitude of erosion occurred with deep reef flats and narrow island widths. For an atoll diameter of 5 km, this shoreline was accretive, but at atoll diameters greater than 5 km it was erosive (Figure 3-6D2). As atoll diameter increased to more than 5 km, the magnitude of erosion decreased.

Island end shorelines were accretive under almost all morphologies. Smaller island widths (Figure 3-6A3), narrower reef flats (Figure 3-6B3), and deeper reef flats (Figure 3-6C3) caused more accretion. The greatest magnitude of accretion occurred with deep reef flats and narrow island widths. At an atoll diameter of 5 km this shoreline was erosive, but at atoll diameters greater than 5 km it was accretive (Figure 3-6D3). As atoll diameter increased to more than 5 km, the magnitude of accretion decreased.

3.4.3 Oblique island

Seaward shorelines demonstrated similar trends to the windward island seaward shoreline, as all were erosive over the range of morphological variations. Smaller island widths (Figure 3-7A1), narrower reef flats (Figure 3-7B1), deeper reef flats (Figure 3-7C1), and smaller atoll diameters (Figure 3-7D1) produced more erosion. Narrow reef flats were associated with intense erosion, even at low sea levels. Although small atoll diameters were associated with the most erosion, medium-sized atolls generally had lower erosion than large atolls. The greatest magnitude of erosion occurred at deep and narrow reef flats.

Lagoon shoreline exhibited similar trends to the windward island lagoon shoreline, in that they were accretive over the range of morphological variations. Smaller island widths (Figure 3-7A2), narrower reef flats (Figure 3-7B2), deeper reef flats (Figure 3-7C2), and smaller atoll diameters (Figure 3-7D2) were characterized by more accretion. Although small atoll diameters were associated with the most accretion, medium-sized atolls generally had lower accretion than large atolls. The greatest magnitude of accretion occurred at narrow island widths.

Leeward island end shorelines were accretive under all modeled morphologies. Larger island widths (Figure 3-7A3), narrower reef flats (Figure 3-7B3), deeper reef flats (Figure 3-7C3), and smaller atoll diameters (Figure 3-7D3) were characterized by increased accretion. The narrowest reef flats were associated with high levels of accretion, even at low sea levels. The greatest magnitude of accretion occurred with deep reef flats. This was the only shoreline in the study for which larger island widths were associated with a greater magnitude of erosion/accretion.

Seaward island end shorelines were erosive under all morphologies. Smaller island widths (Figure 3-7A4), narrower reef flats (Figure 3-7B4), deeper reef flats (Figure 3-7C4), and smaller atoll diameters (Figure 3-7D4) were characterized by increased erosion. The greatest magnitude of erosion occurred with deep reef flats.

3.5. Discussion

3.5.1 Morphological parameters with negligible impact on shoreline erosion

Changing lagoon beach slope, seaward beach slope, fore reef slope, and island length did not significantly impact erosion or accretion patterns in this study. There is no doubt that beach slopes affect sediment transport in the field (Smith et al., 2009), as the slope partially determines nearshore wave breaking conditions, and the K parameter in Eq. 2 is a function of beach slope (Smith et al., 2009), though beach slopes are not explicitly incorporated into the standard CERC equation (Komar, 1971; Rosati, 2002). Our adaptation of the CERC formula is insensitive to beach slope for a few reasons. First, the initial breaking at the reef crest dissipates enough wave energy such that without other morphological differences in reef or island dimensions, the difference in nearshore H_s under different beach slopes is negligible. Second, even at 20-m model grid resolution, there may not be enough spatial resolution to adequately resolve differences in the locations of breaking waves. Finally, smoothing the bathymetry likely muted differences in slope.

Similarly, changes in fore reef slope did not dramatically affect shoreline erosion patterns. This result was surprising given that the reef slope was found to have a significant impact on wave heights and run-up along reef-lined shorelines (Quataert et al., 2015) by increasing nearshore set-up. However, Quataert et al. (2015) found that reef slope had a strong impact on long-period, infragravity waves, and less of an impact on small-period incident waves modeled here. Changes in reef slope did not affect the incident energy of incident band swell waves enough to affect shoreline transport as calculated by CERC.

On an atoll with a diameter of 20 km, varying island length between 1 km and 5 km did not significantly impact shoreline erosion. However, island length could play a greater role in erosion on smaller atolls. On larger atolls, islands are generally situated along a relatively small portion of the reef flat circumference, and thus the entire seaward island shoreline receives waves that have been refracted similarly. However on smaller atolls, a larger island would be exposed to waves that have been refracted over a wider range than a smaller island. Although lagoon beach slope, seaward beach slope, fore reef slope, and island length may affect erosion and accretion patterns in some instances, other morphological characteristics, such as island width or reef flat depth, influence nearshore wave transformations more strongly and thus play a greater role in CERC-derived sediment transport.

3.5.2 Morphological parameters that affect shoreline erosion

The morphological parameters that most influenced shoreline erosion and accretion patterns were island width, reef flat width, reef flat depth, and atoll diameter (Figures 3-5, 3-6, 3-7). These characteristics generally did not cause erosion and accretion trends to reverse (except for decreasing atoll diameters on leeward islands), but affected the magnitude of the erosion or accretion with SLR.

Reef flat width

In general, narrower reef flats led to greater erosion with SLR. Narrower fringing reef flats lead to increased nearshore H_s because the shorter the distance waves travel across the reef flat, the less wave energy is attenuated through frictional dissipation (Lowe et al., 2005; Grady et al., 2013; Ferrario et al., 2014; Quataert et al., 2015). Greater incident wave energy is associated with increased alongshore transport rates (Storlazzi et al., 2011; Grady et al. 2013).

Very narrow fringing reef flats (<50 m) along windward and oblique islands were often associated with relatively high magnitude erosion. This is likely because bathymetric smoothing of a very narrow reef flat renders it almost non-existent. For waves that traverse the reef flat and reach a shoreline, there is minimal dissipation of incident wave energy and therefore high rates of sediment transport. For leeward islands, very narrow reef flats do not have a similar effect. This is likely because waves that reach leeward islands traverse the reef platform width before crossing the lagoon.

Discounting the behavior at very narrow reef flats, the trend between narrower reef flats and more intense erosion was greatest on leeward islands. Waves that reach lagoon shorelines of leeward islands traverse the total reef platform and the lagoon before hitting shore. When crossing the reef flat, these waves refract, so they travel a greater distance than the platform width. As a result, changes in reef flat width are magnified for these waves.

Island width

Narrower islands lead to greater nearshore H_s and increased erosion. When island widths were adjusted in this study, the reef flat width was held constant at 250 m and the reef platform width varied. For example, widening the island by 500 m also widened the reef platform width by 500 m. Sediment erosion and deposition around an atoll island is partially determined by the alongshore wave energy gradient; sediment tends to migrate from regions of high energy to regions of low energy (Kench and Brander, 2006; Kench et al., 2006; Kench et al., 2009; Beetham and Kench, 2014; Smithers and Hoeke, 2014). The magnitude of erosion and deposition is controlled by the gradient in energy; a greater difference in energy between two points leads to greater sediment transport. A wider island decreases the energy gradient from the seaward to lagoon shorelines, because the approximately same change in wave energy is divided over a longer alongshore distance. Therefore, a wider island results in less sediment transport around the island. A secondary impact is that for a given reef flat width, wider islands results in a wider reef platform, which results in increased energy dissipation and less sediment transport (Grady et al., 2013).

Both island width and reef flat width affect the energy gradient across the island. Wider islands decrease the energy gradient by increasing the alongshore distance, as discussed above. Wider reef flats decrease the energy gradient by decreasing the magnitude of incident wave energy on the seaward shoreline. Varying island widths had a stronger impact on erosion magnitudes than varying reef flat widths except for narrow (<150 m) reef flat widths; this implies that under the range of conditions studied here, alongshore distance affects the energy gradient more than incident wave energy. To our knowledge, island width has not been the focus of other published atoll research. Our results demonstrate that it is an important island characteristic for understanding alongshore insular sediment transport.

Reef flat depth

Increasing reef flat depth reduces depth-limited breaking at the reef crest, allowing larger waves to traverse the reef flat, reducing frictional energy dissipation, and increasing erosion. Conversely, shallower reef flats afford more protection from wave attack and reduce erosion. Previous studies have observed increased shoreline erosion with increasing reef depths in the Seychelles due to reef degradation (Sheppard et al., 2005) and in models of fringing reef sediment dynamics in Hawaii (Storlazzi et al., 2011; Grady et al., 2013).

Atoll diameter

Atolls with smaller diameters had greater shoreline erosion for the same forcing than larger atolls. Wave refraction around the atoll and wave shadowing by the windward island (Figure 3-4) likely account for these differences. On smaller atolls, the reef flat and islands have greater curvature, which increases the refraction of wave energy, directing incident energy towards the island shorelines and increasing erosion. On larger atolls, the islands and reef flat have less curvature, reducing wave refraction, which in turn directs less wave energy towards the shoreline, resulting in reduced erosion. Mandlier and Kench (2012) observed that changing the aspect ratio of an oblate coral reef platform greatly affected refraction and wave convergence patterns; the patterns are likely similar for a circular platform with a central lagoon. For example, a 2-km island covers 12.7% of the circumference of a 5-km wide atoll, 6.4% of a 10-km wide atoll, and just 0.7% of an 80-km wide atoll; this is a nonlinear trend. A windward island that covers a greater fraction of atoll circumference will cause a more extensive wave shadow that prevents incident waves from reaching the leeward island. The leeward island lagoon shoreline is accretive at an atoll diameter of 5 km, likely indicating that it is sitting in the wave shadow generated by the windward island. For atoll diameters greater than or equal to 10 km, the leeward lagoon island shoreline is erosive, indicating that wave energy is reaching this shoreline, and that it is no longer in the wave shadow. This result indicates that atoll size is a crucial model parameter, and erosion patterns projected for a smaller atoll may not necessarily be applicable to a larger atoll. Care must be taken when using one atoll to extrapolate future changes to another of a different size (e.g., Shope et al., *in review*).

Our results show that magnitude of erosion generally decreased with increasing atoll diameter up to 40 km, and then slightly increased with increasing atoll diameter up to 80 km. On small-diameter atolls, increased curvature focuses incident wave energy towards the windward island and causes increased erosion, as discussed above. For a medium-sized atoll, the incident wave energy is relatively less, as waves do not refracted as much. These refracted waves traverse the reef flat at an angle, covering a distance that is greater than the reef flat width. As atoll size increases further, the waves are refracted less and less, so that they strike the windward island more perpendicularly. These closer-to-perpendicular waves traverse a shorter distance across the fringing reef flat, which would cause reduced energy dissipation and increased erosion.

3.5.3 Island-scale response to waves and projected morphological changes

Under all scenarios, windward islands experience erosion along their seaward shorelines, intense accretion along their lagoon shorelines, and slight accretion along island end shorelines (Figure 3-5). SLR generally led to an intensification of these patterns. It appears that under SLR, these islands would migrate rapidly toward the lagoon, assuming these wave processes are maintained and dominant over long time periods (Figure 3-8). In contrast, Shope et al. (*in review*) modeled Wake and Midway

Atolls and found that with SLR, the windward islands eroded along seaward shoreline and lagoon shorelines, accreting at the islands' ends and parts of the shoreline with a wider reef flat. Within this study, there was no alongshore variability in reef flat width, which may account for the difference in these findings.

Leeward islands initially experienced intense erosion along their lagoon shorelines and slight erosion along their seaward shorelines (Figure 3-6). Wave energy travels to these islands from two directions. Some wave energy bypasses the windward reef crest, propagates across the lagoon, and erodes sediment along the lagoon shoreline. Other waves refract around the atoll and approach the seaward shoreline (Figure 3-4). Under the 0 m SLR scenario, there is enough incident wave energy along both lagoonal and seaward shorelines that eroded sediment accretes on the islands' ends. As sea level increases, the incident wave energy along the lagoonal shorelines increases more rapidly than along the seaward shorelines. The changing energy gradient causes some sediment to be deposited along the seaward shorelines; however, the dominant region of accretion is still the ends of the islands. With SLR, it is forecast that leeward islands would become longer and thinner while migrating toward the reef rim (Figure 3-8). Shope et al. (*in review*) found similar model results for leeward islands on Wake and Midway Atolls.

Oblique islands erode on the seaward and windward island end shorelines, with the lagoonal and the leeward island ends accreting (Figure 3-7). The windward side of the islands are exposed to much more wave energy than the leeward sides (Figure 3-4). This energy gradient transports sediment from the windward sides to the leeward sides of the islands. Over time under SLR, the oblique islands would migrate leeward along the reef rim and towards the lagoon (Figure 3-8).

3.5.4 Comparison of results with previous studies

Most studies of island morphological change with SLR have not been able to link observations of island response to island and atoll morphology. Atolls have varying wave climates, island configurations, and sediment cover, making it difficult to discern the relative morphological controls on shoreline erosion from purely observational (i.e., aerial or satellite imagery) data. Previous studies have made observations similar to the schematic model results presented here. In a study using aerial photographs and remote sensing, Webb and Kench (2010) found that atoll islands generally eroded along ocean-facing shorelines and accreted along lagoon shorelines in response to historic SLR. An exception to this general trend was observed on Funafuti Atoll, where a leeward island migrated toward the reef rim (Webb and Kench 2010). Similarly, Yates et al. (2013) observed the leeward island on Manuae Atoll migrating toward the reef rim with historic SLR. Webb and Kench (2010) also observed many elongate islands lengthening with historic SLR. Additionally, the lagoon shorelines demonstrated large magnitude trends with historic SLR, indicating that these shorelines will react most dynamically with climate change, as found by Purkis et al. (2016) at Diego Garcia.

However, previous studies have also made observations that differ from the schematic model results presented here. Yates et al. (2013) observed windward islands accreting along their seaward shorelines on Manihi Atoll; Woodroffe (2008) describes seaward shorelines as long-term sediment sinks and erosion along these shorelines as ephemeral. Many other studies have found at least some evidence of seaward shoreline erosion in response to historic SLR. Most atoll islands studied by Webb and Kench (2010) and Purkis et al. (2016) have remained stable with historic SLR. As discussed earlier, however, such historical studies from relatively low recent sea levels compared to the mid-Holocene sea level highstand when most of these island formed might not accurately portray how islands will respond in the future when sea levels are predicted to attain, if not exceed (Vermeer and Rhamstorf, 2009; Grinstead et al. 2009; Nicholls and Cazenave, 2010), those sea levels when islands formed (Dickinson, 2009).

There are many sources of uncertainty—anthropogenic modification, complex morphology, varying wave climates, etc.—that limit the ability of modeling and observational studies to project atoll morphological response to future SLR. Ford (2012) found that shoreline change on Majuro Atoll in response to historic SLR was muted by anthropogenic changes (e.g., harbors and armored shorelines) in urbanized areas. Future SLR is projected to be much more rapid than past SLR (Vermeer and Rhamstorf, 2009; Grinstead et al., 2009; Nicholls and Cazenave, 2010), so atoll islands’ morphological response to historic SLR may not persist. Furthermore, H_s and

θ_w are projected to change at many Pacific atolls in response to climate change (Shope et al., 2016), which may dramatically alter alongshore erosion patterns (Shope et al., *in review*).

3.5.5 Example categorization of island vulnerability to wave-driven erosion with SLR

Wide islands with wide, shallow reef flats on medium-sized (~20 km) atolls are likely to be most resistant to SLR-driven shoreline change (Figure 3-8); reef flat depth and island width are the most important factors. Alphonse, Bikini, and Roi-Namur Islands are examples of islands that exhibit some, but not all, of these characteristics (Table 3-2). Narrow islands with narrow, deep reef flats on small (< 10 km) or large (> 60 km) atolls are likely to be least resistant to SLR-driven shoreline change. Majuro Island, Malé Island, and the northeast island of Manuae Atoll are examples of islands at risk for increased sediment transport based on these characteristics (Table 3-2). However, anthropogenic modification of Malé Island mitigates erosion risk.

In general, uninhabited islands are more at risk for increased erosion with SLR than inhabited islands. Yates et al. 2013 observed significant erosional response to SLR at two narrow, uninhabited islands on Manuae Atoll. On the other hand, people tend to inhabit wider atoll islands so that there is space for infrastructure and crops; Bailey et al. (2010) found that atoll islands need to be at least 300 m wide to provide freshwater resources. Wide islands were found to be relatively resistant to increased erosion

(Figures 3-5, 3-6, 3-7). Furthermore, anthropogenic modification provides further resistance to erosion (Ford 2012).

3.6 Conclusions

The morphology of an atoll and its islands impacts nearshore wave-energy gradients that drive alongshore morphological change. Because atoll islands are generally dynamic features (Kench and Brander, 2006; Rankey, 2011) and these alongshore gradients will likely increase with SLR, atoll shorelines are projected to change considerably by the end of the century. The results presented here suggest that the strongest morphological controls on shoreline stability are island width and reef flat depth; reef flat width and atoll diameter also play a lesser role. It is projected that narrower atolls with deeper reef flats will experience the greatest morphological change with SLR (Figure 3-8). Windward and oblique islands are projected to migrate toward the lagoon, while leeward islands are expected to either migrate toward the reef rim or become longer and narrower.

Based on these results, atoll islands that are most susceptible to future change are small, located on small atolls, and have narrow reef flats. In general, these islands are likely to be uninhabited, due to limited water resources and opportunity for infrastructure development. On inhabited islands, shoreline armoring may mitigate the erosional effect of SLR, regardless of atoll morphology. Even so, because SLR is excepted to accelerate at unprecedented rates over the next century, many inhabited atoll islands will be at risk of increased shoreline erosion and threatened infrastructure.

Schematic physics-based modeling can help elucidate the changes that atoll islands may face in the future by allowing isolation of the role of individual morphologic characteristics on resulting physical processes. The results make it possible to identify features of atoll islands that characterize the relative stability of their shorelines. Thus, one can evaluate any individual atoll islands' relative susceptibility to erosion or accretion, regardless of whether bathymetric data are available to model future changes for that atoll. Because existing atoll bathymetric data are extremely limited, schematic atoll modeling can make a valuable, broad contribution to projecting future shoreline erosion and planning for future hazards.

Future work could address some of these limitations and improve the applicability of schematic atoll models. More complex, realistic bathymetry could be generated and used for schematic modeling, including alongshore variations in reef flat width and depth, different island configurations, and/or varying atoll shapes. A numerical coupled hydrodynamic and sediment transport model could more accurately capture sediment transport around an atoll island to better understand the complexities and feedbacks that govern shoreline change over time.

Acknowledgements

This work was carried out under the USGS's Pacific Coral Reef Project as part of an effort in the United States and its trust territories to better understand the effect of geologic and oceanographic processes on coral reef systems and the USGS's Climate Change Impacts to the U.S. Pacific and Arctic Coasts Project to understand the impact of climate change on U.S. and U.S.-affiliated island shorelines. This project was funded by the USGS's Coastal and Marine Geology Program and Department of Defense's Strategic Environmental Research and Development Program (SERDP) under RC-2334. Funding was also provided by the Dr. Earl H. Myers and Ethel M. Myers Oceanographic and Marine Biology Trust and Wells Fargo Coastal Sustainability Fellowship. Use of trademark names does not imply USGS endorsement of products.

References

Adams, P. N., D. L. Inman, and J. L. Lovering (2011), Effects of climate change and wave direction on longshore sediment transport patterns in Southern California, *Clim. Change*, *109*, 211–228, doi:10.1007/s10584-011-0317-0.

Ashton, A. D., & Murray, A. B. (2006). High-angle wave instability and emergent shoreline shapes: 1. Modeling of sand waves, flying spits, and capes. *Journal of Geophysical Research: Earth Surface*, *111*(F4).

Bailey, R. T., J. W. Jenson, and A. E . Olsen (2010), Estimating the ground water resouces of atoll islands, *Water*, *2*(1), 1–27, doi: 10.3390/w2010001.

Becker, J. M., M. A. Merrifield, and M. Ford (2014), Water level effects on breaking wave setup for Pacific Island fringing reefs, *J. Geophys. Res.-Oceans*, *119*(2), 914–932, doi:10.1002/2013JC009373.

Beetham, E. P., and P. S. Kench (2014), Wave energy gradients and shoreline change on Vabbinfaru platform, Maldives, *Geomorphology*, *209*, 98–110, doi:10.1016/j.geomorph.2013.11.029.

Booij, N., R. C. Ris, and L. H. Holthuijsen (1999), A third-generation wave model for coastal regions - 1. Model description and validation, *J. Geophys. Res.-Oceans*, *104*(C4), 7649–7666, doi:10.1029/98JC02622.

Cheriton, O. M, C. D. Storlazzi, K. J. Rosenberger (2016), Observations of wave transformation over a fringing coral reef and the importance of low-frequency waves and offshore water levels to runup, overwash, and coastal flooding, *J. Geophys. Res.-Oceans*, *121*(5), 3121–3140, doi:10.1002/2015JC011231.

Dickinson, W. (2004), Impacts of eustasy and hydro-isostasy on the evolution and landforms of Pacific atolls, *Palaeogeogr. Palaeoclimatol. Palaeoecol.*, *213*(3–4), 251–269, doi:10.1016/j.palaeo.2004.07.012.

Dickinson, W. R. (2009), Pacific Atoll Living: How Long Already and Until When, *GSA Today*, *19*(3), 4, doi:10.1130/GSATG35A.1.

Van Dongeren, A., Lowe, R., Pomeroy, A., Trang, D., Roelvink, D., Symonds, G., and R. Ranasinghe (2013), Numerical modeling of low-frequency wave dynamics over a fringing coral reef, *Coast. Eng.*, *73*, 178–190, doi:10.1016/j.coastaleng.2012.11.004.

Ferrario, F., M. W. Beck, C. D. Storlazzi, F. Micheli, C. C. Shepard, and L. Airoldi (2014), The effectiveness of coral reefs for coastal hazard risk reduction and adaptation, *Nat. Commun.*, *5*, 3794, doi:10.1038/ncomms4794.

Ford, M. (2012), Shoreline Changes on an Urban Atoll in the Central Pacific Ocean: Majuro Atoll, Marshall Islands, *J. Coast. Res.*, *28*(1), 11–22, doi:10.2112/JCOASTRES-D-11-00008.1.

Ford, M., Becker, J., and M. Merrifield (2013), Reef flat wave processes and excavation pits: observations and implications for Majuro Atoll, Marshall Islands, *J. Coast. Res.*, *29*(3), 545–554, doi:10.2112/JCOASTRES-D-12-00097.1.

Gourlay, M. R. (1996), Wave set-up on coral reefs. S. Set-up on reefs with various profiles, *Coast. Eng.*, *28*, 17–55.

Grady, A. E., L. J. Moore, C. D. Storlazzi, E. Elias, and M. A. Reidenbach (2013), The influence of sea level rise and changes in fringing reef morphology on gradients in alongshore sediment transport, *Geophys. Res. Lett.*, *40*(12), 3096–3101, doi:10.1002/grl.50577.

Grigg, R. W. (1982), Darwin point: a threshold for atoll formation, *Coral Reefs*, *1*, 29–34. doi:10.1007/BF00286537.

Grinsted, A., J. C. Moore, and S. Jevrejeva (2009), Reconstructing sea level from paleo and projected temperatures 200 to 2100 ad, *Clim. Dyn.*, *34*(4), 461–472, doi:10.1007/s00382-008-0507-2.

Grothe, P.R., L.A. Taylor, B.W. Eakins, K.S. Carignan, R.R. Warnken, E. Lim, and R.J. Caldwell, 2010a. Digital Elevation Models of Wake Island: Procedures, Data Sources and Analysis, NOAA Technical Memorandum NESDIS NGDC-32, Dept. of Commerce, Boulder, CO, 22 pp.

Grothe, P.R., L.A. Taylor, B.W. Eakins, K.S. Carignan, E. Lim, R.R. Warnken, and R.J. Caldwell, 2010b. Digital Elevation Models of Midway Island: Procedures, Data Sources and Analysis, NOAA Technical Memorandum NESDIS NGDC-33, Dept. of Commerce, Boulder, CO, 24 pp.

Hagan, A. B., and T. Spencer, (2008), Reef resilience and change 1998–2007, Alphonse Atoll, Seychelles, paper presented at the Proc.11th Int. Coral Reef Symp., pp. 388–392, Ft. Lauderdale, Fla.

Hamylton, S. (2011), The use of remote sensing and linear wave theory to model local wave energy around Alphonse Atoll, Seychelles, Estuarine Coastal Shelf Sci., 95(4), 349–358, doi:10.1016/j.ecss.2011.08.035.

Harney, J. N. and C. H. Fletcher, III (2003), A budget of carbonate framework and sediment production, Kailua Bay, Oahu Hawaii, *J. Sed. Res.*, *73*(6), 865–868. doi:10.1306/051503730856.

Hoeke, R. K. (2010), An investigation of wave-dominated coral reef hydrodynamics. PhD thesis, James Cook University.

Hoeke, R. K., K. L. McInnes, J. C. Kruger, R. J. McNaught, J. R. Hunter, and S. G. Smithers (2013), Widespread inundation of Pacific islands triggered by distant-source wind-waves, *Glob. Planet. Change*, *108*, 128–138, doi:10.1016/j.gloplacha.2013.06.006.

Hoeke, R., McInnes, K., O’Grady, J., 2015. Wind and Wave Setup Contributions to Extreme Sea Levels at a Tropical High Island: A Stochastic Cyclone Simulation Study for Apia, Samoa. J. Mar. Sci. Eng. 3, 1117–1135. doi:10.3390/jmse3031117

Jensen, O. J. (1991), Waves on coral reefs, paper presented at the Proc. 7th Symp. Coastal and Ocean Management - Coastal Zone, vol. 91, pp. 2668–2680, Long Beach, AXE, New York.

Kench, P. S., and R. W. Brander (2006), Response of reef island shorelines to seasonal climate oscillations: South Maalhosmadulu atoll, Maldives, *J. Geophys. Res.*, *111*(F1), doi:10.1029/2005JF000323.

Kench, P. S., R. F. McLean, and S. L. Nichol (2005). New model of reef-island evolution: Maldives, Indian Ocean, *Geology*, *33*(2), 145–148.

Kench, P. S., R. W. Brander, K. E. Parnell, and R. F. McLean (2006), Wave energy gradients across a Maldivian atoll: Implications for island geomorphology, *Geomorphology*, *81*(1–2), 1–17, doi:10.1016/j.geomorph.2006.03.003.

Kench, P. S., K. E. Parnell, and R. W. Brander (2009), Monsoonally influenced circulation around coral reef islands and seasonal dynamics of reef island shorelines, *Mar. Geol.*, *266*(1–4), 91–108, doi:10.1016/j.margeo.2009.07.013.

Komar, P. D. (1971), The mechanics of sand transport on beaches, *J. Geophys. Res.*, *76*, 713–721.

Komar, P. D. (1998), *Beach Processes and Sedimentation*, Prentice-Hall, Upper Saddle River, N.J.

Lowe, R. J., J. L. Falter, M. D. Bandet, G. Pawlak, M. J. Atkinson, S. G. Monismith, and J. R. Koseff (2005), Spectral wave dissipation over a barrier reef, *J. Geophys. Res.*, *110* C04001.

Mandlier, P.G. and P.S. Kench (2012), Analytical modelling of wave refraction and convergence on coral reef platforms: implicaions of island formation and stability, *Geomorphology*, *159*, 84–92. doi: 10.1016/j.geomorph.2012.03.007.

McLean, R. and P. Kench (2015), Destruction or persistence of coral atoll islands in the face of 20th and 21st century sea-level rise? *WIRES Climate Change*, *6*(5), 445–463, doi:10.1002/wcc.350.

Montaggioni, L. F. (2005), History of Indo-Pacific coral reef systems since the last glaciation: Development patterns and controlling factors, *Earth-Sci. Rev.*, *71*(1–2), 1–75, doi:10.1016/j.earscirev.2005.01.002.

Nicholls, R. J., and A. Cazenave (2010), Sea-level rise and its impact on coastal zones, *science*, *328*(5985), 1517–1520.

Ohde, S., M. Greaves, T. Masuzawa, H. A. Buckley, R. Van Woesik, P. A. Wilson, P. A. Pirazzoli, and H. Elderfield (2002), The chronology of Funafuti Atoll: revisiting an old friend, *Proc. R. Soc. Math. Phys. Eng. Sci.*, *458*(2025), 2289–2306, doi:10.1098/rspa.2002.0978.

Pelnard-Considere´, R. (1956), Essai de theorie de l’evolution des formes de rivage en plages de sable et de galets, in 4th Journees de l’Hydraulique, Les Energies de la Mer, III, pp. 289– 298, La Houille Blanche, Grenoble, France.

Pequignet, A. C., J. M. Becker, M. A. Merrifield, and S. J. Boc (2011), The dissipation of wind wave energy across a fringing reef at Ipan, Guam, *Coral Reefs*, *30*, 71–82, doi:10.1007/s00338-011-0719-5.

Pomeroy, A., Lowe, R., Van Dongeren, A., Ghisalberti, M., Bodde, W., and D. Roelvink (2015), Spectral wave-driven sediment transport across a fringing reef, *Coast. Eng.*, *98*, 78–94, doi:10.1016/j.coastaleng.2015.01.005.

Purkis, S. J., R. Gardiner, M. W. Johnston, and C. R. C. Sheppard (2016), A half-century of coastline change in Diego Garcia - The largest atoll island in the Chagos, *Geomorphology*, *261*, 282–298, doi:10.1016/j.geomorph.2016.03.010.

Quataert, E., C. Storlazzi, A. van Rooijen, O. Cheriton, and A. van Dongeren (2015), The influence of coral reefs and climate change on wave-driven flooding of tropical coastlines, *Geophys. Res. Lett.*, *42*(15), 6407–6415, doi:10.1002/2015GL064861.

Rankey, E. C. (2011), Nature and stability of atoll island shorelines: Gilbert Island chain, Kiribati, equatorial Pacific: Atoll shoreline change, equatorial Pacific, *Sedimentology*, *58*(7), 1831–1859, doi:10.1111/j.1365-3091.2011.01241.x.

Ris, R. C., L. H. Holthuijsen, and N. Booij (1999), A third-generation wave model for coastal regions - 2. Verification, *J. Geophys. Res.-Oceans*, *104*(C4), 7667–7681, doi:10.1029/1998JC900123.

Rosati, J. D., T. L. Walton, and K. Bodge (2002), Longshore sediment transport, in Coastal Engineering Manual, part II, Coastal Sediment Processes, edited by D. B. King, chap. III-2, U.S. Army Corps of Eng., Washington, D. C.

Roy, P., and J. Connell (1991), Climatic-Change and the Future of Atoll States, *J. Coast. Res.*, *7*(4), 1057–1075.

Sheppard, C., D. J. Dixon, M. Gourlay, A. Sheppard, and R. Payet (2005), Coral mortality increases wave energy reaching shores protected by reef flats: Examples from the Seychelles, *Estuar. Coast. Shelf Sci.*, *64*(2–3), 223–234, doi:10.1016/j.ecss.2005.02.016.

Shope, J. B., C. D. Storlazzi, L. H. Erikson, and C. A. Hegermiller (2016), Changes to extreme wave climates of islands within the Western Tropical Pacific throughout the 21st century under RCP 4.5 and RCP 8.5, with implications for island vulnerability and sustainability, *Glob. Planet. Change*, *141*, 25–38, doi:10.1016/j.gloplacha.2016.03.009.

Shope J.B., C.D. Storlazzi, and R.K. Hoeke (2016), Projected atoll shoreline and run-up changes in response to sea-level rise and varying large wave conditions at Wake and Midway Atolls, Northwestern Hawaiian Islands. *Geomorphology, In Review*.

Smith, E. R., P. Wang, B. A. Ebersole, and J. Zhang (2009), Dependence of Total Longshore Sediment Transport Rates on Incident Wave Parameters and Breaker Type, *J. Coast. Res.*, *25*(3), 675–683, doi:10.2112/07-0919.1.

Smithers, S. G., and R. K. Hoeke (2014), Geomorphological impacts of high-latitude storm waves on low-latitude reef islands — Observations of the December 2008 event on Nukutoa, Takuu, Papua New Guinea, *Geomorphology*, *222*, 106–121, doi:10.1016/j.geomorph.2014.03.042.

Storlazzi, C. D., E. Elias, M. E. Field, and M. K. Presto (2011), Numerical modeling of the impact of sea-level rise on fringing coral reef hydrodynamics and sediment transport, *Coral Reefs*, *30*, 83–96, doi:10.1007/s00338-011-0723-9.

Storlazzi, C. D., E. P. L. Elias, and P. Berkowitz (2015), Many Atolls May be Uninhabitable Within Decades Due to Climate Change, *Sci. Rep.*, *5*, 14546, doi:10.1038/srep14546.

Taebi, S., and C. Pattiaratchi (2014), Hydrodynamic response of a fringing coral reef to a rise in mean sea level, *Ocean Dyn.*, *64*(7), 975–987, doi:10.1007/s10236-014-0734-5.

Vermeer, M., and S. Rahmstorf (2009), Global sea level linked to global temperature, *Proc. Natl. Acad. Sci.*, *106*(51), 21527–21532.

Vousdoukas, M. I., Velegrakis, A. F., and T. A. Plomaritis (2009), Beachrock occurrence, characteristics, formation mechanisms and impacts, *Earth-Science Reviews*, *85*(1–2), 23–46. doi: 10.1016/j.earscirev.2007.07.002.

Webb, A. P., and P. S. Kench (2010), The dynamic response of reef islands to sea-level rise: Evidence from multi-decadal analysis of island change in the Central Pacific, *Glob. Planet. Change*, *72*(3), 234–246, doi:10.1016/j.gloplacha.2010.05.003.

Woodroffe, C., McLean, R., Smithers, S., and E. Lawson (1999), Atoll reef-island formation and response to sea-level change: West Island, Cocos (Keeling) Islands, *Marine Geology*, *160*(1–2), 85–104, doi:10.1016/S0025-3227(99)00009-2.

Woodroffe, C. D. (2008), Reef-island topography and the vulnerability of atolls to sea-level rise, *Glob. Planet. Change*, *62*(1–2), 77–96, doi:10.1016/j.gloplacha.2007.11.001.

Yates, M. L., G. Le Cozannet, M. Garcin, E. Salaï, and P. Walker (2013), Multidecadal Atoll Shoreline Change on Manihi and Manuae, French Polynesia, *J. Coast. Res.*, *289*, 870–882, doi:10.2112/JCOASTRES-D-12-00129.1.

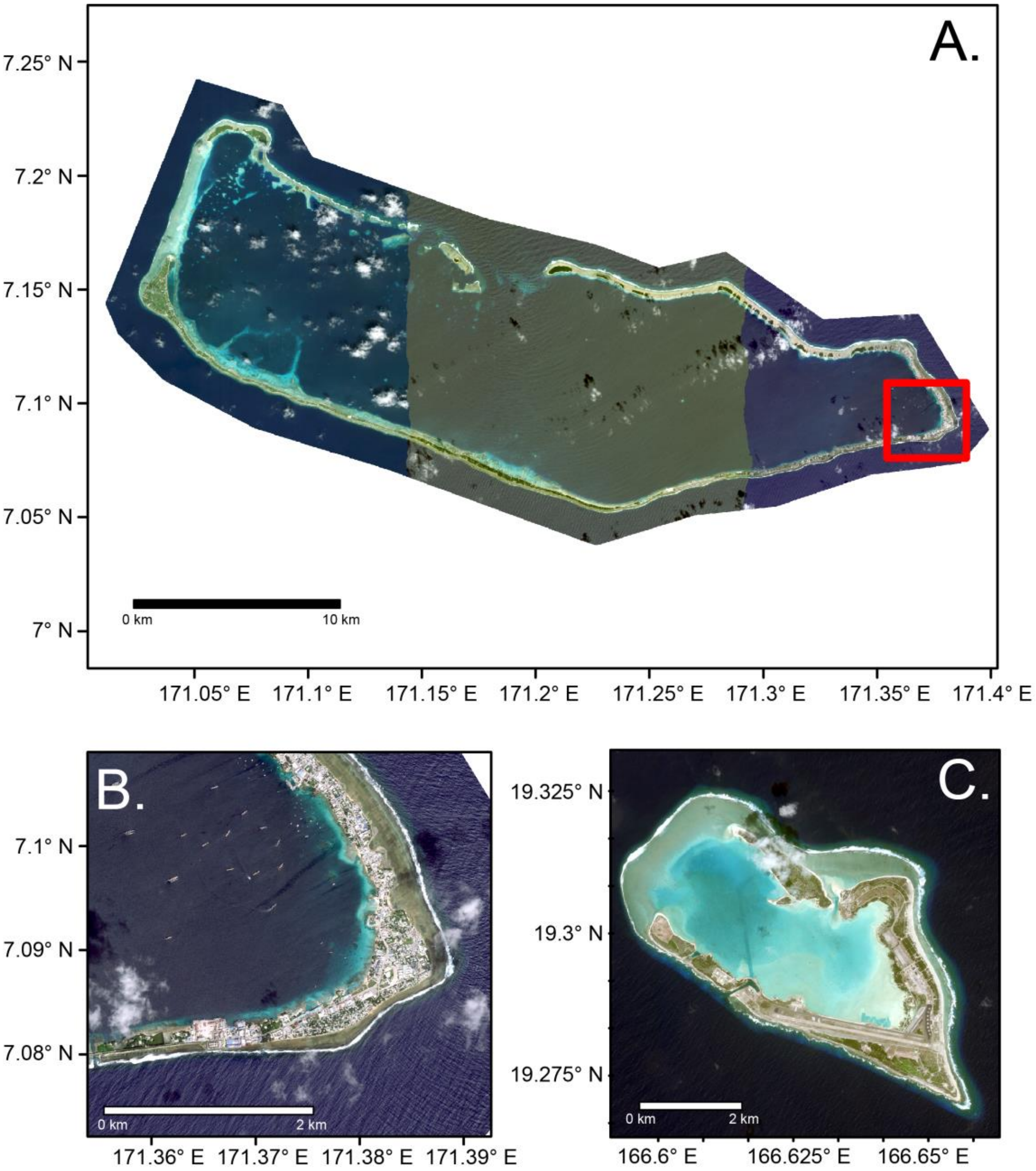

Figure 3-1. Examples of atoll diameters and atoll island sizes at (A) Majuro Atoll, RMI, (B) Majuro Island, and (C) Wake Atoll. The red box in panel A denotes the region captured by panel B. Note the difference in atoll diameter between Majuro and Wake Atolls and the difference in island widths. Imagery Source: Digital Globe's WorldView2 satellite (2012, 2013). Thanks to Tony Kimmet of the USDA-NRCS-National Geospatial Center of Excellence for imagery acquisition.

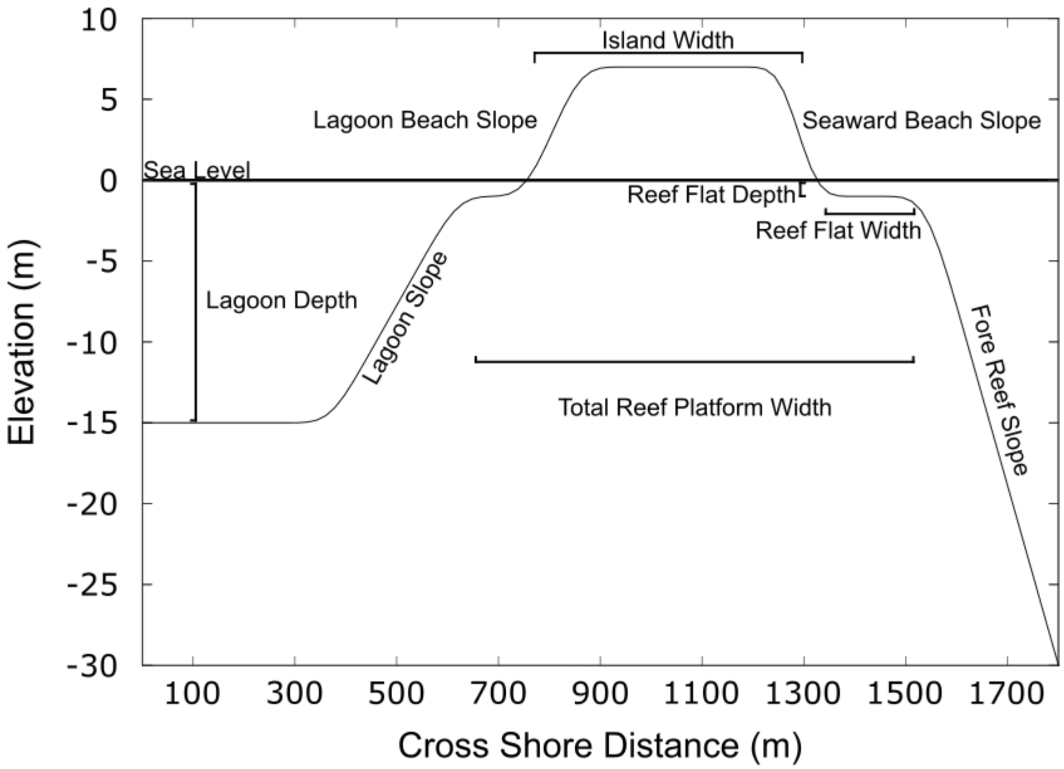

Figure 3-2. Cross-section of schematized atoll island with labeled morphological parameters.

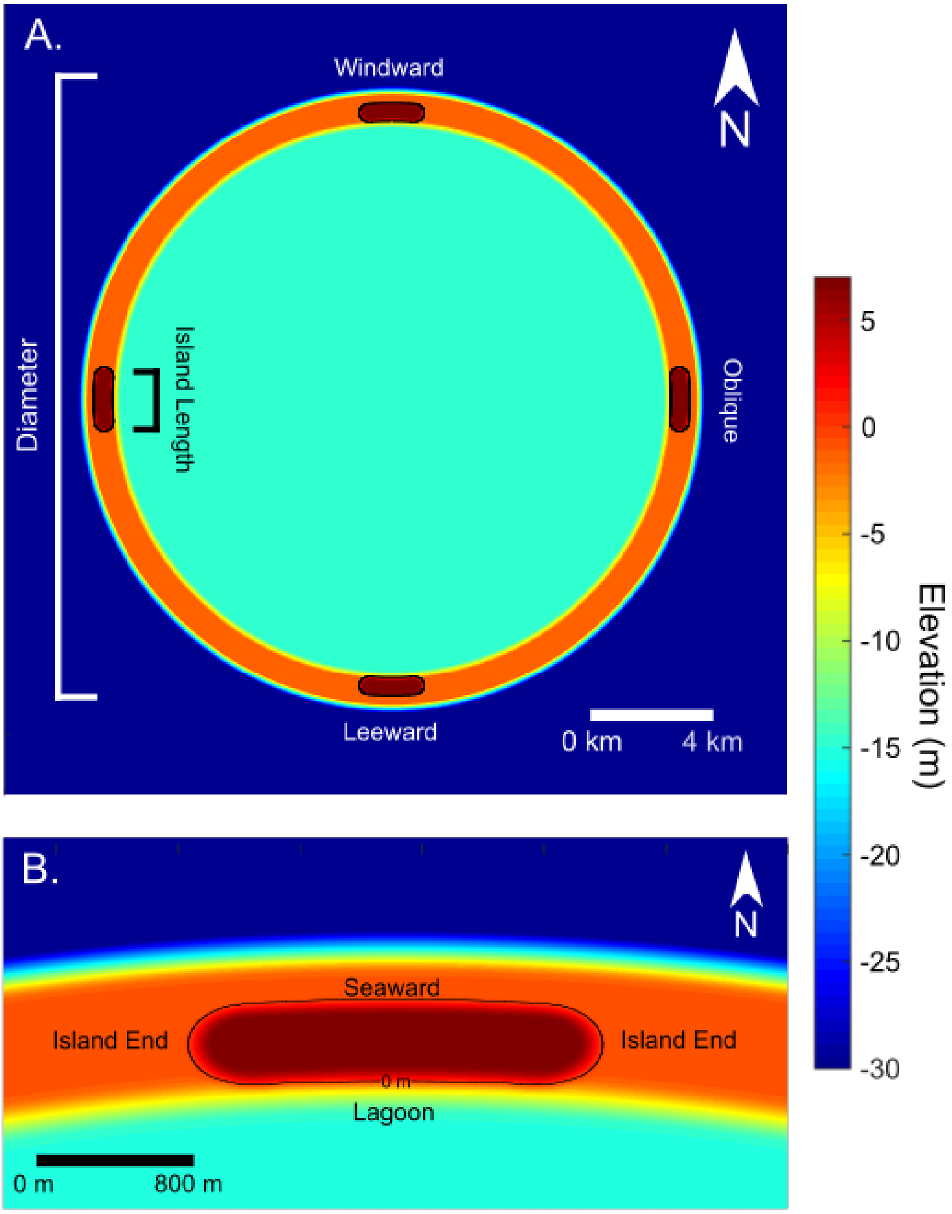

Figure 3-3. Topography and bathymetry of the schematized atoll initial control configuration. (A) Topography and bathymetry at the atoll-scale with labeled morphological parameters and island location in reference to incident waves coming from the top of the diagram and (B) a zoomed in image of the northern island indicating the shoreline divisions. Elevations are in meters and the black lines indicate the 0 m contour.

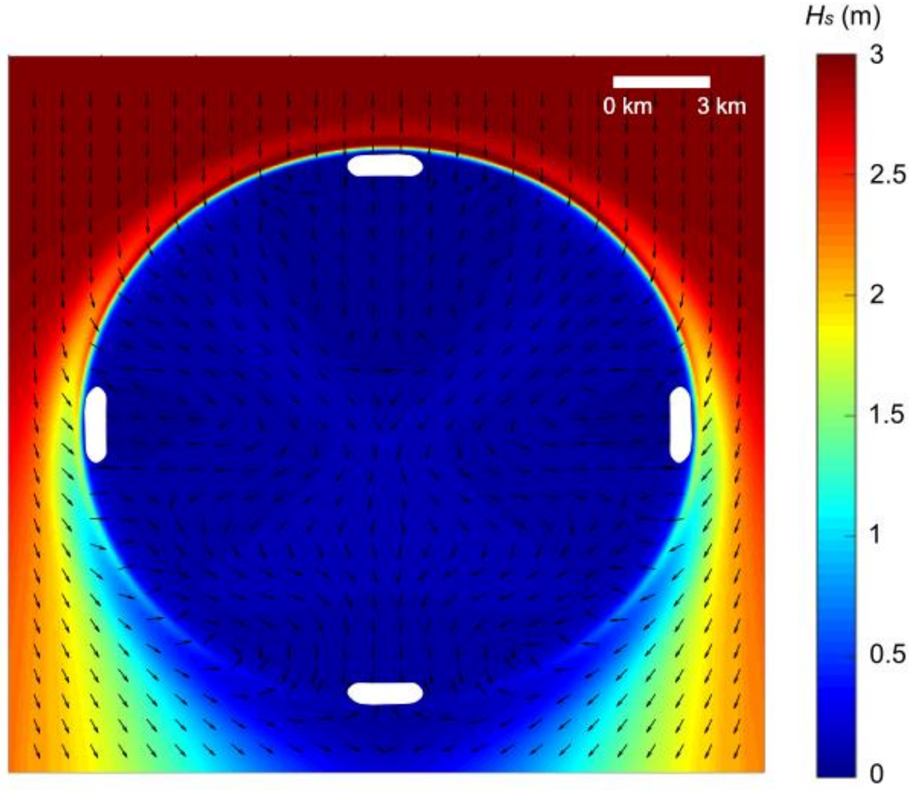

Figure 3-4. Example wave height and wave direction output for 20-km atoll. White areas represent islands; black arrows represent wave direction. Waves approach from the top boundary of the model domain and refract around the atoll.

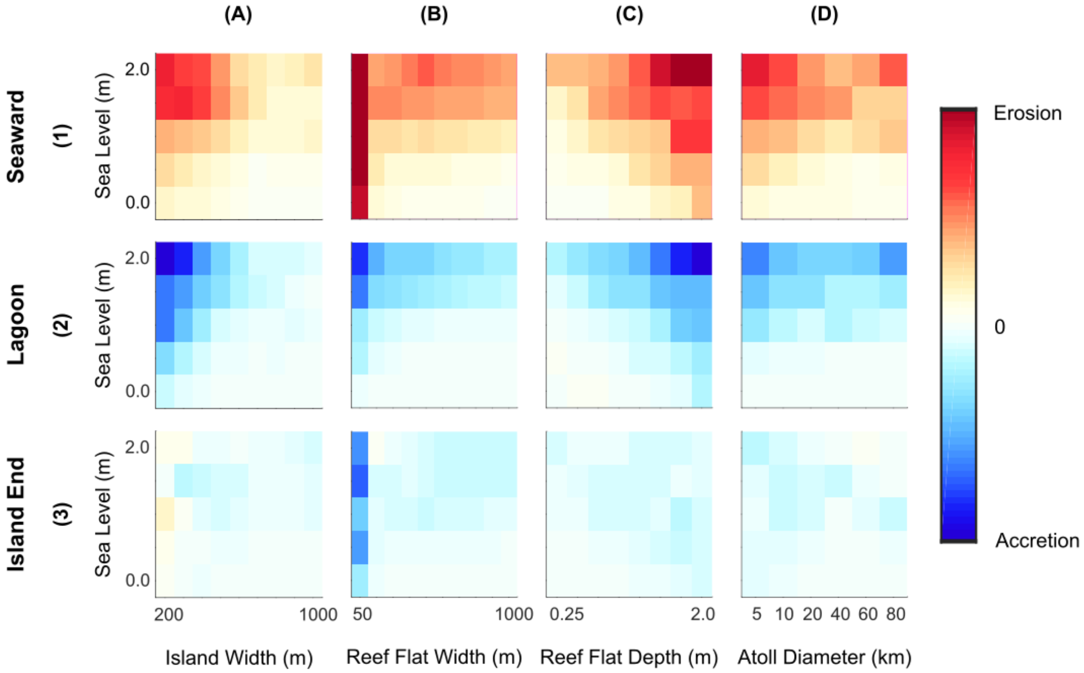

Figure 3-5. Relative changes in shoreline erosion/accretion magnitudes with morphological parameter (A–D) and SLR (y-axis of each plot) for the windward island by shoreline. Rows describe erosion changes for (1) seaward, (2) leeward, and (3) island end shorelines while columns denote magnitude changes with (A) island width, (B) reef flat width, (C) reef flat depth, and (D) atoll diameter. The color ramp is linear, but absolute magnitudes are unlisted to address only the relative changes in values. The color red indicates net erosion values and blue as net accretion values with increasing color intensities indicating greater magnitudes.

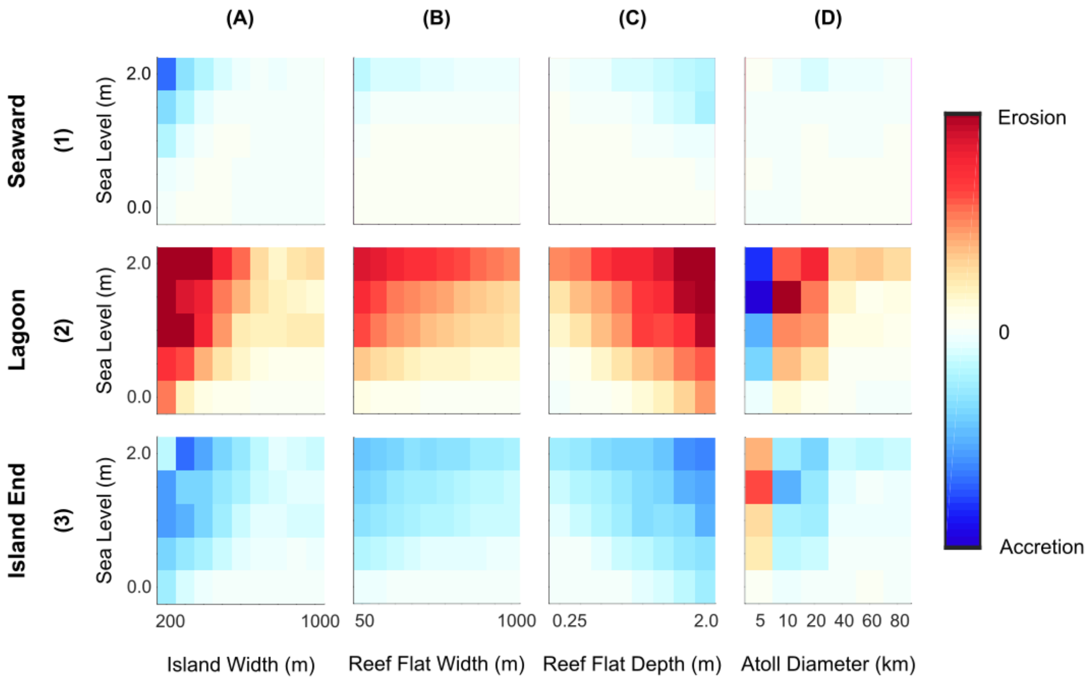

Figure 3-6. Relative changes in shoreline erosion/accretion magnitudes with morphological parameter (A–D) and SLR (y-axis of each plot) for the leeward island by shoreline. Rows describe erosion changes for (1) seaward, (2) leeward, and (3) island end shorelines while columns denote magnitude changes with (A) island width, (B) reef flat width, (C) reef flat depth, and (D) atoll diameter. The color ramp is linear, but absolute magnitudes are unlisted to address only the relative changes in values. The color red indicates net erosion values and blue as net accretion values with increasing color intensities indicating greater magnitudes.

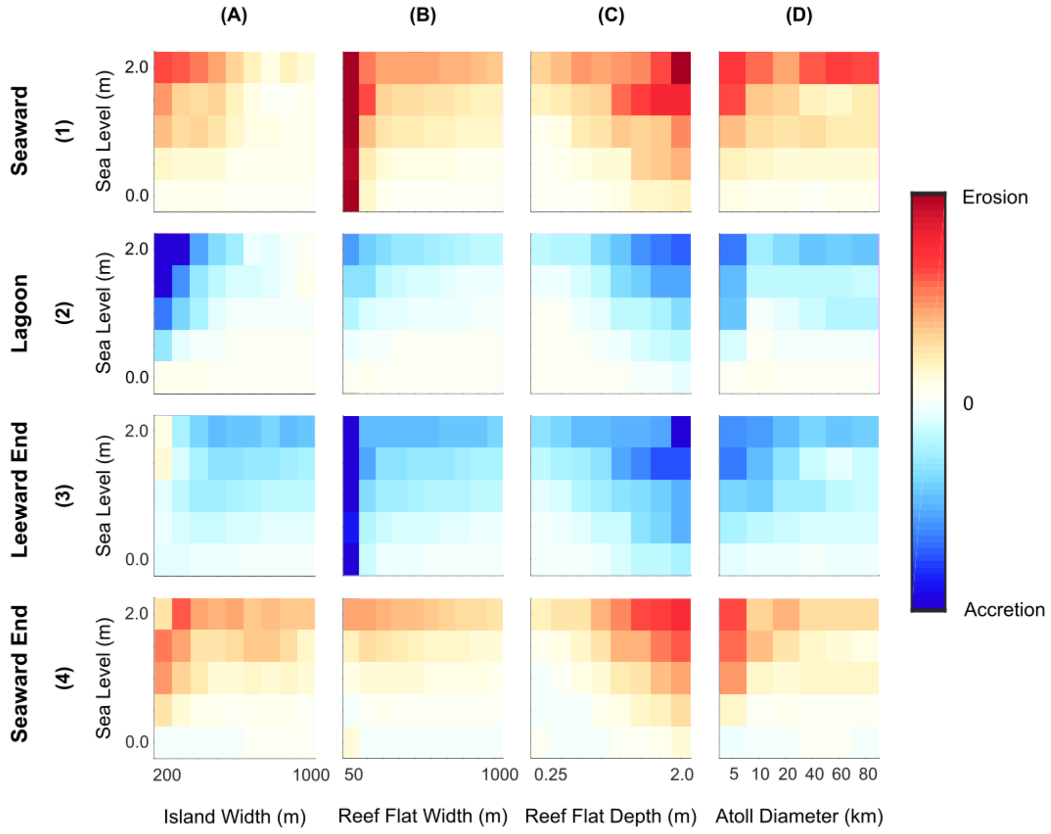

Figure 3-7. Relative changes in shoreline erosion/accretion magnitudes with morphological parameter (A–D) and SLR (y-axis of each plot) for the oblique island by shoreline. Rows describe erosion changes for (1) seaward, (2) leeward, (3) leeward island end, and (4) windward island end shorelines while columns denote magnitude changes with (A) island width, (B) reef flat width, (C) reef flat depth, and (D) atoll diameter. The color ramp is linear, but absolute magnitudes are unlisted to address only the relative changes in values. The color red indicates net erosion values and blue as net accretion values with increasing color intensities indicating greater magnitudes.

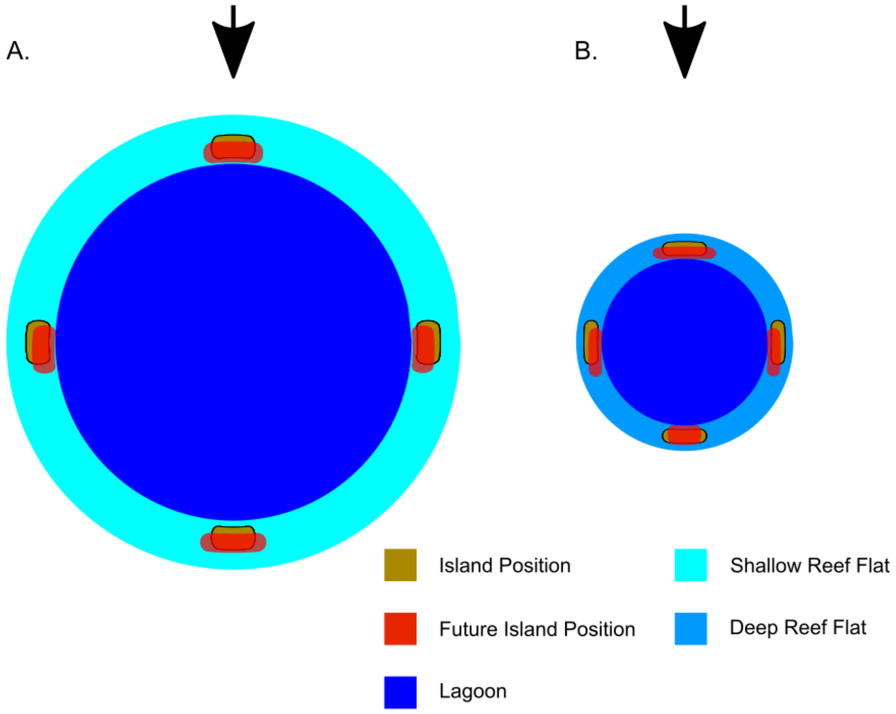

Figure 3-8. Schematic atoll island shoreline response to SLR, with waves approaching from the top of the diagram. A. Relatively resistant atoll (shallow, wide fringing reef flat; large atoll; wide islands). B. Relatively susceptible atoll (deep, narrow fringing reef flat; small atoll, narrow islands). Initial island positions are shown in gold, with future positions overlain in red.

Parameter	Range Used	Initial Control	References
Island Width	200 - 1000 m	500 m	Woodroffe et al., (2008); Webb and Kench (2010) *
Island Length	1000 - 5000 m	2000 m	Webb and Kench (2010) *
Ocean-Facing Slope	1/3 - 1/12	1/6	Rankey (2011); Beetham et al., (2015); Quataert et al., (2015); Grothe et al., (2010a,b)
Lagoon-Facing Slope	1/12 - 1/20	1/15	Grothe et al., (2010a,b)
Fore Reef Slope	1/5 - 1/20	1/10	Hoeke et al., (2011); Beetham et al., (2015); Quataert et al., (2015)
Reef Flat Width	50 - 1000 m	250 m	Woodroffe et al., (2008); Kench et al., (2009); Quataert et al., (2015)*
Reef Flat Depth	25 - 200 cm	1.0 m	Woodroffe et al., (2008); Yates et al., (2013); Quataert et al., (2015)
Atoll Diameter	5 - 80 km	20 km	Ford (2012); Yates et al., (2013)*
Sea-Level Rise	0 - 2.0 m	0 m	Vermeer and Rhamstorf (2009); Grinstead et al., (2009); Nicholls and Cazenave (2010)

* denotes that ranges are supplemented by measurements from Google Earth Satellite Imagery

Table 3-1. Morphological parameters varied within this study with a characteristic range of values determined from literature references, bathymetric data, and Google Earth satellite imagery, along with values for the initial control model scenario.

	Island	**Atoll**	**Island Width (m)**	**Reef Flat Width (m)**	**Reef Flat Depth (m)**	**Atoll Diameter (km)**	**References**
Examples of Islands **Susceptible** to Increased Erosion	Majuro	Majuro	560	250	0.8–1	40	Ford (2012); Becker et al., (2014) *
	Malé	North Malé	> 1000	0–140	1.30–3.80	60	Jensen (1991) *
	Northeast	Manuae	380	250–300	1–2	10	Yates et al., (2013)
Examples of Islands **Not Susceptible** to Increased Erosion	Alphonse	Alphonse	1000	500	0–0.2	6	Hagan and Spencer (2008); Hamylton (2011) *
	Bikini	Bikini	840	800	–	40	*
	Roi-Namur	Kwajalein	900	250–300	< 1	100	Quataert et al., (2015)

* denotes data supplemented using Google Earth satellite imagery

Table 3-2. Examples of atoll islands susceptible and not susceptible to increased shoreline erosion with SLR, based on schematic model results.